

Faculdade de Engenharia da Universidade do Porto



**Recording and Feedback Control of Neuronal
Activity Levels Using Microelectrode Arrays: New
Therapeutic Strategies based on
Electrostimulation**

Fábio Marques do Amaral

Dissertação realizada no âmbito do
Mestrado em Engenharia Biomédica

Orientador: Paulo de Castro Aguiar

setembro de 2018

A Dissertação intitulada

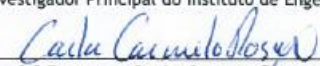
“Recording and Feedback Control of Neuronal Activity Levels Using
Microelectrode Arrays: New Therapeutic Strategies Based on Electrostimulation”

foi aprovada em provas realizadas em 24-09-2018

o júri


Presidente Prof. Doutor José Alberto Peixoto Machado da Silva
Professor Associado do Departamento de Engenharia Eletrotécnica e de Computadores da
FEUP - U. Porto


Doutor Paulo de Castro Aguiar
Investigador Principal do Instituto de Engenharia Biomédica - INEB - U. Porto


Prof.ª Doutora Carla Susana Santana Carmelo Rosa
Professora Auxiliar da Faculdade de Ciências da U. Porto

O autor declara que a presente dissertação (ou relatório de projeto) é da sua exclusiva autoria e foi escrita sem qualquer apoio externo não explicitamente autorizado. Os resultados, ideias, parágrafos, ou outros extratos tomados de ou inspirados em trabalhos de outros autores, e demais referências bibliográficas usadas, são corretamente citados.


Autor - Fábio Marques do Amaral

Resumo

O sistema nervoso humano é de longe o sistema mais complexo conhecido pela ciência, e a comunidade neurocientífica está ainda a tentar compreender as dinâmicas neuronais em condições normais e patológicas. A natureza elétrica da dinâmica neuronal faz da eletrofisiologia a principal metodologia para compreender como é que a informação neuronal é transferida, integrada e processada. Contudo, a eletrofisiologia não é apenas registar a atividade neuronal. Um grande número crescente de evidências mostra as vantagens terapêuticas de estimular e modular com precisão a atividade neuronal em condições patológicas. A estimulação elétrica (EE) tem muito potencial em vários campos de investigação, principalmente em tratamentos médicos de neuroreabilitação. Um dos cenários de reabilitação melhor sucedidos é na doença de Parkinson (DP), através de Estimulação Cerebral Profunda. No entanto, apesar das melhorias clínicas significativas em estados iniciais da DP, com a progressão da doença, a tendência é para perder a sua eficácia devido à adaptação das células às características constantes dos estímulos elétricos. Uma das soluções para esta perda de eficácia da EE na DP, e em outras patologias benéficas dos sistemas de EE aprovados, é o desenvolvimento de sistemas de malha fechada em tempo real, que automaticamente adaptam as características do seu estímulo para o indivíduo e para o estado corrente da doença. O principal objetivo do presente trabalho é a investigação de novos sistemas, métodos e protocolos para alcançar controlos ao nível da atividade em populações neuronais usando recorrentes configurações de matrizes de microelétrodos de elevada densidade. Numa perspetiva clínica, o desenvolvimento de uma nova geração de dispositivos implantáveis baseados em sistemas de realimentação de malha fechada em tempo real, usando matrizes de microelétrodos capazes de interações bidirecionais com neurónios através de EE, são de importância fundamental para tratar doenças neurológicas. A característica principal desta dissertação é a sua natureza transdisciplinar, combinando neurobiologia, eletrofisiologia, culturas de células neuronais, programação e simulações, eletrónica e teoria de controlo. Um objetivo suplementar desta dissertação é o *design* e a construção de um sistema de eletrofisiologia de baixo custo e de fácil construção “Do-It-Yourself” (DIY). O sistema DIY é composto por um amplificador de baixo custo e um *headstage* de interface capaz de ler e

transmitir sinais eletrofisiológicos de uma matriz de microelétrodo com 60 elétrodo para um sistema de aquisição de dados.

Abstract

The human nervous system is by far the most complex system known to science, and the neuroscience community is still trying to understand neuronal dynamics in normal and pathological conditions. The electrical nature of neuronal dynamics makes electrophysiology the main methodology to understand how neuronal information is transferred, integrated and processed. But electrophysiology is not only recording activity from neurons; a growing body of evidence shows the therapeutic advantages of precisely stimulating/modulating the neuronal activity in pathological conditions. Electrical stimulation (ES) has a lot of potential in many research fields, mainly as a medical treatment in neurorehabilitation. One of the most well succeeded rehabilitation scenarios is in the Parkinson's Disease (PD) through Deep Brain Stimulation (DBS). But despite significant clinical improvements at PD's earlier stages, with the progression of the disease, the tendency is to lose its efficacy due to cell's adaptation to the constant features of the electrical stimuli. A solution to this loss of efficacy of ES in PD, and in many other pathologies benefiting from approved ES systems is the development of real-time closed-loop systems that automatically adapt its stimuli features according to the individual and to the current state of the disease. The primary goal of the present work is the investigation of new systems, methods and protocols to achieve activity level control in neuronal populations using state-of-the-art high-density microelectrode arrays (MEAs) setups. In a clinical perspective, the development of a new generation of implantable devices based in real-time closed-loop feedback systems using MEAs capable of a bidirectional interaction with the neurons through ES, are of fundamental importance to treat neurological diseases. A core feature of this dissertation project is its transdisciplinary nature, combining neurobiology, electrophysiology, neuronal cell cultures, programming and simulations, electronics and control theory. A supplementary outcome of this thesis is the design and construction of a low cost and easy-to-build DIY ("Do-It-Yourself") electrophysiology system. The DIY system is composed of a low-cost amplifier and an interface-headstage capable of reading and transmitting electrophysiological signals from a microelectrode array with 60 electrodes to a data acquisition system.

Acknowledgments

Em primeiro lugar gostaria de agradecer ao meu orientador, o Dr. Paulo Aguiar pela oportunidade e por todo o seu apoio neste trabalho e dizer ainda que foi para mim um privilégio fazer parte do grupo NCN (Neuroengineering and Computational Neuroscience), localizado no Instituto de Investigação e Inovação em Saúde (i3S), onde foi realizado o presente trabalho. Quero também deixar um agradecimento aos meus colegas do grupo, em especial à Dr. Cátia Lopes, ao Dr. Miguel Aroso e ao José Mateus por garantirem que eu tinha culturas neuronais para realizar as minhas experiências. Ainda, à Ana Gerós e à Kristine Heiney agradeço pela sua ajuda na parte do trabalho que envolvia programação. No geral, deixo-vos uma palavra de apreço não só pela disponibilidade para me ajudarem que sempre demonstraram, mas também pelo excelente espírito de grupo que aí encontrei.

Ao senhor Pedro Alves, técnico dos laboratórios de eletrónica da Faculdade de Engenharia da Universidade do Porto quero agradecer-lhe pela ajuda que me deu na construção do meu circuito.

Contents

Resumo	iii
Abstract	vi
Acknowledgments	viii
Contents	x
List of Figures	xiii
List of Tables	xvi
Abbreviations, Acronyms e Symbols	xviii
Chapter 1	1
Introduction.....	1
1.1. Motivation.....	2
1.2. Objectives	5
1.3. Document Structure.....	6
Chapter 2	8
Electrophysiology	8
2.1. Introduction to electrophysiology	8
2.1.1. Neuronal membrane	9
2.1.2. Hodgkin and Huxley model	10
2.1.3. Integrate and fire model	13
2.1.4. From neuroscience to neuroengineering	16
2.2. Introduction to standard electrophysiological devices and types of signals	18
2.2.1. Intracellular devices (patch-clamp and intracellular sharp microelectrodes)..	21
2.2.2. Extracellular devices: standard planar-MEAs	22
2.2.3. Extracellular recordings with MEAs: technical considerations	24
2.2.4. “In-cell” recordings using extracellular MEAs	29
Chapter 3	36
Closed-loop system and PID controller.....	36
3.1. Closed-loop systems.....	36

3.2.	Signal processing and spike detection	37
3.3.	PID Control.....	38
3.3.1.	The feedback principle	38
3.3.2.	Components of a PID controller.....	40
3.3.3.	Controller Tuning	43
Chapter 4	47
Materials and Methods	47
4.1.	Integrate and Fire model with a PID controller	47
4.1.1.	Choice of the mathematical model to simulate neuronal activity.....	47
4.1.2.	Integrate-and-Fire model implementation.....	48
4.1.3.	Introduce the controller in the model	49
4.1.4.	Tuning the controller	52
4.1.5.	Validation of the controller.....	52
4.2.	“Real-time” closed-loop control	54
4.2.1.	Electrophysiological system overview	54
4.2.2.	Preparation of MEA for cell culture	55
4.2.3.	Cell culture experiments.....	55
4.2.4.	MEA2100 setup	56
4.2.5.	Stimuli Validation protocol	62
4.2.6.	Neuronal network experiments protocol	65
4.2.7.	Data analysis code.....	65
Chapter 5	69
Results and Discussion	69
5.1.	Integrate and Fire model with a PID controller	69
5.1.1.	Integrate-and-Fire model implementation.....	69
5.1.2.	Controller’s implementation - “real-time” firing rate calculation	70
5.1.3.	PID controller tuning.....	72
5.2.	“Real-time” closed-loop control	81
5.2.1.	Stimuli validation experiments.....	81
5.2.2.	Neuronal network control experiments	89
5.3.	Future Perspectives	95
Chapter 6	97
Conclusion	97
References	100
Appendix A	108
Appendix B	112

List of Figures

Figure 1.1 - Clinical impact of neurological diseases and injuries.	3
Figure 2.1 - Hodgkin and Huxley equivalent electrical circuit for a membrane cell's compartment..	11
Figure 2.2 - Schematic representation of the IF-model.	14
Figure 2.3 - The leaky IF-model response to the variation of the electrode's current over the time	15
Figure 2.4 - IF-model vs experimental results..	16
Figure 2.5 - Schematic representations of the planar MEA60 chip and the planar MED64 chip.	18
Figure 2.6 - Current flow around an axon described by the Volume Conductor Theory..	19
Figure 2.7 - Recorded current flow along an isolated axon predicted by the Volume Conductor Theory results in a triphasic waveform..	19
Figure 2.8 - Intracellular and extracellular spikes recorded simultaneously.	20
Figure 2.9 - Overview of intracellular and extracellular signals recorded by intracellular and extracellular devices	23
Figure 2.10 - Passive equivalent electrical circuit of the interface between a planar MEA and a neuron..	24
Figure 2.11 - Gold mushroom-shaped microelectrode (gM μ E)..	31
Figure 2.12 - Passive equivalent electrical circuit for the gM μ E-neuron interface when the neuron completely engulfs the gM μ E.	33
Figure 2.13 - Passive equivalent electrical circuit for the gM μ E-neuron interface when the neuron partially engulfs the gM μ E.....	34
Figure 3.1 - Block diagram of a simple feedback system.	39
Figure 3.2 - A block diagram of a PID controller in a feedback loop..	40
Figure 3.3 - Typical response of a PID control system in a closed-loop	41
Figure 3.4 - Example of a closed-loop system with a proportional control.	41
Figure 3.5 - Example of a closed-loop system with a proportional and integral control.....	42
Figure 3.6 - Example of a closed-loop system with a proportional, integral and derivative control.	42
Figure 3.7 - PID controller's theory..	43
Figure 4.1 - A block diagram of the in silico PID control model.....	49
Figure 4.2 - Firing rates estimation through two different methods.	51
Figure 4.3 - Area between the response curve of the system and the setpoint value	52
Figure 4.4 - Layout of the recording setup used in the experiments.	57
Figure 4.5 - Screen capture of the stimulators settings control window tab.....	58

Figure 4.6 - Screen capture of the feedback control window.....	60
Figure 4.7 - Setup of the MEA2100-System and “real-time” feedback scheme	62
Figure 5.1 - Simulation of a neuron using the IF-model..	70
Figure 5.2 - Gaussian and α -function causal kernels curves.....	70
Figure 5.3 - Validation and comparison between both kernels.	71
Figure 5.4 - Proportional gain (K_p) tuning of the PID controller.	72
Figure 5.5 - Integral gain (K_i) tuning of the PID controller.	73
Figure 5.6 - Action of the moving average filter in the control error e of the PID controller..	74
Figure 5.7 - Derivative gain (K_d) tuning of the PID controller.....	75
Figure 5.8 - Panel with the different graphs of firing rate (Hz) obtained with derivative gain (K_d) tuning of the PD controller.....	75
Figure 5.9 - Summary of the results obtained with the model during the simulation	76
Figure 5.10 - Summary of the tuning process evolution.	77
Figure 5.11 - Summary of the results obtained with the model using the parameters obtained using the area tuning process..	78
Figure 5.12 - PID controller response to abrupt changes in the firing rate.	79
Figure 5.13 - Results of the PID controller response to noise introduction in the simulated neuronal model..	80
Figure 5.14 - Example of a real-time recording using the MEA2100-120-System.	82
Figure 5.15 - Activity mean levels and respective standard deviations of the experiments (1 - 8) to validate the stimuli (with a stationary phase of 50 ms).....	84
Figure 5.16 - Activity mean levels and respective standard deviations of the experiments (9 - 16) to validate the stimuli (without a stationary phase).	85
Figure 5.17 - Stimuli effect in the form of a ratio interval calculated between the feedback mean firing rates and the basal pre-feedback mean firing rates.	86
Figure 5.18 - Results of experiments 23 and 24 with a normalized noise level.	87
Figure 5.19 - Screen capture of the selected electrodes used in the experiments (18-22, 25).	89
Figure 5.20 - Bar plot graphs showing the activity mean levels and respective standard deviations of the neuronal network experiments (18,20,22).	90
Figure 5.21 - Complementary results of the experiments 20 (at 21DIV)..	91
Figure 5.22 - Bar plot graphs showing the activity mean levels and respective standard deviations of the neuronal network experiments (23,24).	92
Figure 5.23 - Complementary results of the experiments 25 (at 22DIV) with normalized noise conditions..	93
Figure 5.24 - Baseline noise levels of the system using dedicated and not dedicated stimulation electrodes.	94

List of Tables

Table 3.1 - Effects of independent P, I and D tuning.....	43
Table 3.2 - Controller parameters for the Ziegler-Nichols frequency response method which gives controller parameters in terms of critical gain k_c and critical period T_c	44
Table 4.1 - Summary of voltage stimulation pulses tested.	64
Table 5.1 - Gains and respective values used in area tuning process	78
Table 5.2 - Summary of the experiments features	82

Abbreviations, Acronyms e Symbols

List of abbreviations

ADC	Analog-to-digital Conversion
AP	Action Potential
BMI	Brain Machine Interfaces
CC	Coupling Coefficient
CNS	Central Nervous System
DBS	Deep Brain Stimulation
DIV	Days <i>in vitro</i>
DIY	Do-It-Yourself
DSP	Digital Signal Processor
EAP	Extracellular Action Potential
EPSPs	Excitatory Postsynaptic Potentials
ES	Electrical Stimulation
FPS	Field Potentials
GHK	Goldman-Hodgkin-Katz
gMμEs	Gold Mushroom-Shaped Microelectrodes
HDMEAs	High-Density Microelectrodes Arrays
HH	Hodgkin-Huxley
IAP	Intracellular Action Potential
IF	Integrate-and-Fire
IPSPs	Inhibitory Postsynaptic Potentials
jm	Junctional Membrane
LFPs	Local Field Potentials
MCS	Multichannel Systems
MEA	Microelectrodes Array
MED	Multielectrode Dish
njm	Non-Junctional Membrane
NS	Nervous System
PD	Parkinson's Disease
PEI	Polyethyleneimine
PID	Proportional-Integral and Derivative

PNS	Peripheral Nervous System
RMS	Root Mean Square
SNR	Signal-To-Noise Ratio

List of symbols

C_m	Capacitor
C_{njm}	Non-junctional membrane capacitance
e	Control error
E_L	Membrane equilibrium
E_m	Resting potential
E_X	Equilibrium potential
F	Faraday's constant
\overline{g}_L	Membrane leakage conductance
\overline{g}	Membrane maximum conductance
g_X	Conductance per unit area
I	Membrane current
I_c	Capacitive current
I_e	Electrode current
I_i	Ionic current
I_K	Potassium current
I_L	Leak current
I_{Na}	Sodium current
K_c	Critical gain
K_d	Derivative gain
K_i	Integral gain
K_p	Proportional gain
P_X	Permeability of the membrane
r_{isi}	Interspike-interval firing rate
R_m	Membrane resistance
R_{njm}	Non-junctional membrane resistance
R_s	Seal resistance
T	Temperature in Kelvins
T_c	Period of oscillation
t_{isi}	Spikes period
V	Membrane potential
V_{reset}	Reset potential
$[X]_{in}$	Concentrations in the intracellular fluid
$[X]_{out}$	Concentrations in the extracellular fluid
$Z_{electrode}$	Electrode impedance
z_x	Valence of the ion
τ_m	Membrane time constant of the neuron

Chapter 1

Introduction

The human nervous system (NS) is the most complex structure known to man: currently, we know more about the dynamics of distant stars than what happens in a single neuron. The NS is divided into two main components: the central nervous system (CNS) and the peripheral nervous system (PNS). In the CNS is where the information received by the sensory receptors of the PNS is integrated, processed and the decisions of “what to do” are taken and after that, the “commands” are sent to effector organs [1]. To carry input and output information, the PNS has two distinct divisions: the afferent (sensorial) and the efferent (motor). However, despite this global and simple vision of the NS, to understand its complexity is necessary to look inside the human brain with more detail. It is constituted by billions of neurons differentiated into subtypes each one with thousands of cells similar in structure and genetics. These cells interact and communicate with each other resulting in quadrillions of synapses [1], [2]. Despite the very large number of neurons in the brain ($\sim 10^{11}$) [3], [4], they represent a small fraction of the total amount of cells in the brain. The majority of cells are glial cells consisting of microglia, astrocytes, and oligodendrocytes, not capable of generating action potentials (APs) [4].

Among several methodologies, electrophysiology remains the standard approach to study the NS dynamics and analyze the electrical nature of neuronal cells [5]. The electrical properties of neuronal cells have been studied at different levels, from a single-ion channel to extensive neuronal networks, with the aim of elucidating the underlying mechanisms of brain-like synaptic plasticity, AP propagation inside neuronal networks, among others [6], [7]. Despite the efforts to develop new technologies and techniques using electrodes, the conventional techniques such as the patch clamp, intracellular sharp microelectrodes and planar substrate integrated microelectrodes arrays (MEAs) are still the “gold standard” methods to perform neuronal electrophysiology [8], [9]. However, they have critical limitations that will be presented and discussed later.

A major goal in neuroscience research is to understand the relation between specific neuronal circuits properties and dynamics, and associated normal physiological functions or pathologies [2], [8]. However, these tasks have a high level of difficulty due to the sheer volume of neuronal cells and synaptic events within neuronal networks and also due to the fact that neuronal activity is processed at different spatial and temporal scales [5], [7]. Current MEAs have key properties such as long-term, parallel and multisite simultaneous recordings, which makes them an ideal tool to record the spatiotemporal dynamics of neuronal populations. But by itself, recording is not enough and frequently it is necessary to create bidirectional interfaces between electrodes and cells capable to both record and stimulate the cells. Such interfaces are not only fundamental for basic neuroscience, they have also great therapeutic potential for the development of medical devices which address neurological diseases through the modulation of neuronal activity [2], [5].

1.1. Motivation

Neuronal diseases and disorders have an enormous and increasing impact on an aging population, leading to an increase in mortality and morbidity [10], [11]. Furthermore, besides their impact on populations' health, they have associated medical treatments costs [12], [13]. Figure 1.1 presents a projection of the impact and worldwide distribution of Parkinson disease (PD) in 2030, one key neurological disease in our current societies, as well as the annual costs of several disorders in the US.

The integrity of the whole nervous system is crucial and damages in neuronal circuits from one region of the brain can lead to irreversible damages in other parts. The damages can occur due to internal or external factors like injury, inflammation, and trauma and also can be divided into different types such as neurological, neurodegenerative, psychiatric and neuromuscular conditions which correspond to the following respective examples, PD, Alzheimer disease, major depressive disorder and multiple sclerosis [2], [3].

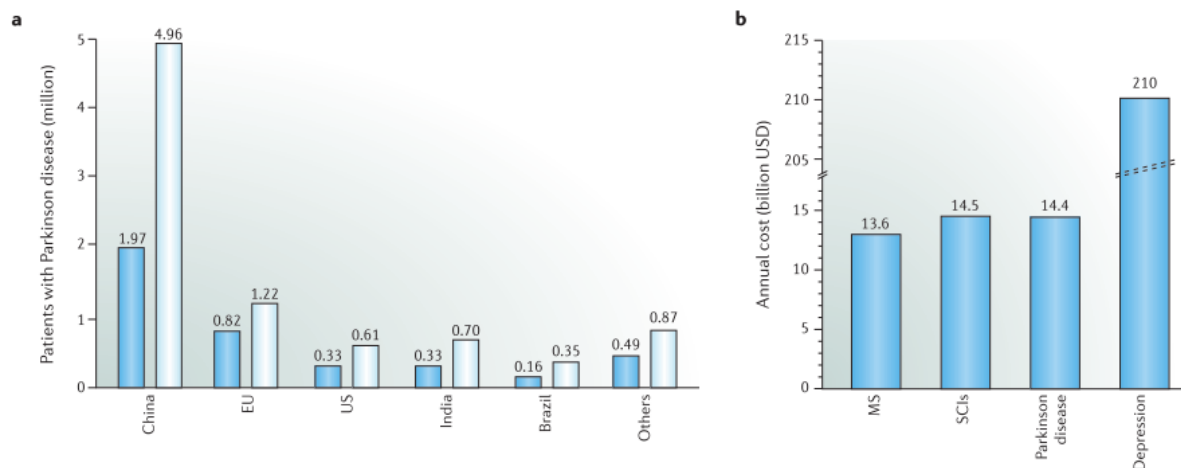


Figure 1.1 - Clinical impact of neurological diseases and injuries. (a) Worldwide distribution and population diagnosed with PD in 2005 (blue) and the corresponding projection for 2030 (light blue). (b) Estimation of annual costs of several disorders in the US. Adapted from [2].

Neurological impairments are often “fought” with neurological rehabilitation strategies, which aim to improve the patient’s life quality restoring their independence in daily tasks. Applied techniques make use of the brain’s plasticity which is a set of mechanisms that allow the brain to adapt and modify its functions according to a new scenario [12]. These modifications can be at the level of existing synapses (synaptic potentiation, depression or excitability changes) or morphological changes (number of dendrites, for instance) [12].

As an alternative to the conventional pharmacological approaches (drugs), electrical stimulation (ES) is gaining attention as an effective therapeutic strategy. Currently, ES is widely used as a medical treatment in neurorehabilitation and therapeutic applications [14]-[16], for instance, to recover limbs’ control in case of nervous system injury and also to treat neuronal disorders. ES has been used to treat neurological damages through neuromodulation of brain’s plasticity by targeted and specific delivery of electrical stimuli. One of the most well-succeeded strategies is the Deep Brain Stimulation (DBS) [12], [13], [17]. It consists in the continuous application of small electrical pulses delivered by implanted stimulation electrodes near target specific regions of the brain to modulate or disrupt abnormal activity, for instance, by changing firing rate and/or firing patterns of individual neurons [12], [17], [18]. DBS is recognized by the US Food and Drug Administration, for application in neurological treatments and was first approved to treat Essential Tremor in 1997. Since 2002 has been applied to treat PD, in 2003 was approved for clinical application in primary dystonia cases and since 2009 it started to be used to treat Obsessive Compulsive Disorder [13], [17]. Further, DBS has also been used as a treatment for other neurological disorders despite its therapeutic effect is not well understood yet. Other examples of ES based therapies include reduction of seizures in Epilepsy, to treat neuropathic pain, psychiatric disorders, depression, Alzheimer’s disease, to recover from stroke damages, among others [12], [17].

To elucidate a common problem of using ES to treat neurological disorders, it will be used the PD as an example. PD is a chronic neurodegenerative movement disorder that tends to evolve and getting worse. Despite treatments with medications are very successful and have significant improvements in many patients, for other patients or in advanced stages of the disease, medication practically loses its effect [18]. An alternative is the DBS which in PD treatment is one of the most well-established techniques capable to control motor symptoms and improve patients' life quality [18]. However, as previous mentioned, PD is a progressive disease with dynamic features which bring constraints to the current open-loop DBS methods due the fact that optimization of stimulation parameters is, mainly, responsibility of clinician and patient's experience which is a subjective parameter and ends up being an iterative process to achieve the adequate stimulation parameters. Also, after some time, the same static stimulation has a tendency to lost is effect and does not avoid the progression of the disease and, meanwhile the disease symptoms will appear again. So, contrariwise to traditional approaches, it is truly important the development of DBS real-time closed-loop systems capable to automatically adapt and adjust their stimulation parameters according to neuronal activity and disease changes to maximize therapeutic results [18].

Another common disorder, and quite present in current populations, are deafness or blindness. By means of ES to sensory neurons is possible to transmit the information to the brain and keep the normal course of the information without significant losses. One famous and successful procedure are the cochlear implants [16], [19] and, not so usual but with great progress in the past years are the retinal implants to treat blindness [20], [21]. Depending on the type of application and the deepness of target neuronal cells, the amplitude of the stimuli can change [5].

By itself, ES is not enough to study the neuronal system but when allied at the same time with recordings of the stimulus-response activity, this is a very powerful technique [5], mainly in emerging areas like brain-computer interfacing and neuroprosthetics [16], [22]. Here, spatial precise stimulation is crucial [23].

The current technologies have limitations which do not enable a complete understanding of all neuronal processes, however, with the development of new technologies, especially, nanotechnologies, diagnosis, and treatment of neuronal pathologies may be achieved [9]. Despite that, current electrophysiological technologies to record neuronal activity as the ones produced by Multi Channels Systems (MCS) (Reutlingen, Germany), for instance, are very expensive which is a large barrier for many labs to acquire these systems and give their contribution in the neuroscience field.

1.2. Objectives

Many NS pathologies can be corrected using ES in well-defined neuronal populations. Recent developments and improvements in microelectrodes fabrication allied to new knowledge about how to stimulate, record and decode neuronal activity have led to an increasing interest in the development of interface systems between populations of neurons and electronic circuits. Between the various types of arrays of microelectrodes that have been developed, there is a configuration with very promising features, in which the microelectrodes are fabricated with the shape of a mushroom with about 1 micrometer of height and width.

The primary objective of this dissertation was the investigation of systems, methods and protocols to achieve activity level control in neuronal populations using state-of-the-art high-density MEAs setups. These feedback control systems are of fundamental importance for the development of the new generation of implantable devices using ES to treat neurological diseases. A core feature of this dissertation project is its transdisciplinary nature, combining neurobiology, electrophysiology, neuronal cell cultures, programming and simulations, electronics and control theory.

The main objective can be divided into two components: an experimental and a theoretical. The experimental part consisted of the design and implementation of an *in vitro* “real-time” closed-loop control system to attain constrained (controlled) global activity levels of a neuronal population cultured on the top of MEAs chips. To this purpose, the commercial MEA2100-System from MSC (Reutlingen, Germany), capable of record and stimulate simultaneously up to 252 microelectrodes, was used. This is only possible because the system has an integrated Digital Signal Processor (DSP), connected to the amplifiers and stimulators, which can be programmed for “real-time” signal detection, filtering and feedback stimulation. In order to accomplish this objective, several experiments were first done to validate the stimulus parameters in order to induce an inhibitory response in the neuronal cells within the range of the stimulation electrodes, reducing their global firing activity. After this validation, a set of experiments were performed to evaluate the stimulus efficacy in the context of a neuronal network. Although MEAs chips with 256 electrodes were used, the goal was to control the global activity level on the culture (population mean level), using feedback stimulation in response to the variation of neuronal populations mean firing rate and not control each microelectrode of the array individually. Different methodologies were also explored, including the development of an *in silico* control system. To achieve this, a canonical and versatile Proportional-Integral and Derivative (PID) control method was implemented in a simulated neuron, using the well-established integrate-and-fire (IF) model for neuronal dynamics. This *in silico* controller was simulated in MATLAB R2017b environment (The MathWorks Inc., USA) and aims to maintain the neuron’s firing rate at a certain well-defined level through the injection

of precise current (calculated by the PID controller) in the differential equation that characterizes the dynamics of the neuron.

Also, motivated by the fact that equipment for electrophysiology with MEAs is quite expensive, and out of reach for many neuroscience/neuroengineering research labs, a supplementary goal of this dissertation was the design, construction and validation of a low cost and easy-to-build DIY (“Do-It-Yourself”) electrophysiology system. The DIY system was composed of a low-cost amplifier and an interface-headstage capable of reading and transmitting electrophysiological signals from an MEA with 60 electrodes to a data acquisition system. Despite relevant progress made in several components of the DIY system, being this a secondary goal, the available time did not allow its full conclusion and validation. The description of the developed prototype can be found in Appendix B.

1.3. Document Structure

The work is divided into six main chapters. Chapter 1 is the introduction and presents the motivations and objectives to elaborate the present work. Chapter 2 presents a review of the literature in the electrophysiology field. Section 2.1 makes an introduction to this topic, starting by describing the neuronal membrane and its properties. It also includes two basic mathematical models to describe neuronal dynamics. The historical transition from neuroscience to neuroengineering is also described in this section. Sections 2.2 - 2.2.3 review the electrophysiological standard devices/techniques and the different types of electrophysiological signals. Section 2.2.4 presents a new category of extracellular MEAs and describes a new configuration of microelectrodes with the shape of a mushroom, which have very promising features. Chapter 3 (section 3.1) makes an introduction to closed-loop systems and their importance in clinical applications in the treatment of neuronal disorders and even in the development of Brain-machine interfaces (BMI). Section 3.2 presents important considerations about signal processing and spike detection. Section 3.3 introduces the feedback principle and the theory behind the classical PID controllers. Chapter 4 presents the materials and methods used in this work. Section 4.1 describes the set of steps made to develop, tune and validate the *in silico* PID control system. Section 4.2.1 gives an overview of the MEA2100-System. Sections 4.2.2 and 4.2.3 describe how to prepare the MEAs for neuronal cultures and the isolation protocol. Sections 4.2.4 - 4.2.6 describe the acquisition system setup and the protocol of the experiments. Section 4.2.7 describes the MATLAB code to analyze the recorded data. Sections 5.1 and 5.2 present and discuss the experimental results obtained in this work. Section 5.1 is dedicated to the *in silico* PID control system and, the “real-time” closed-loop experimental results and discussion are presented in section 5.2, followed by considerations about future work/directions presented in section 5.3. Chapter 6 presents the conclusions and final remarks of this dissertation work.

Chapter 2

Electrophysiology

2.1. Introduction to electrophysiology

Electrophysiology is a field of science dedicated to the study of the electrical properties of cells and biological tissues, mainly in the neuroscience area where it is considered the standard approach [5]. Changes in these properties, currents or voltages, can be measured at different scales, from ion channels to networks of neurons, and allow the nervous system to perform and control its various functions such as sensory perception, memory, and motor action [3]. The study of these properties is quite important as it allows a better knowledge of the brain's behavior and neuronal pathologies such as epilepsy, Parkinson's or Alzheimer's disease, for example. These measurements are only possible since neuronal cells, due to their electrical nature, are capable to generate and transmit electrical signals which can be detected by specific devices called electrodes, even at a distance from the source [5]. This electrical activity occurs because there is a difference in the potential across the cells' membranes, namely between the inside and the outside of the cell. This difference results from different ionic concentrations on both sides of the cellular membrane. The flow of some ions as sodium (Na^+) and potassium (K^+) through the membrane by specific ionic channels causes alterations at the membrane potential, which can be measured through electronic circuits [7], [24]. The membrane potential is the key to neurons being able to transmit and integrate signals [7]. The membrane's resting potential can be defined as the sum of the equilibrium potentials of the different ions and of their relative permeabilities and, under normal conditions, this value is about -65 mV [7]. When the membrane potential, for instance, through ES, reaches a certain threshold of depolarization, an AP is generated.

An ideal electrophysiological system should have the capability to record a set of electrophysiological signals from individual neurons such as APs, subthreshold postsynaptic potentials (excitatory - EPSPs or inhibitory - IPSPs) and subthreshold membrane oscillations. Further, through electrical current application (stimulation) and simultaneously with the

recordings, the system should also be capable of modulating the activity of specific neurons within the neuronal network [8].

2.1.1. Neuronal membrane

The membrane of a neuron is composed by an impermeable lipid bilayer and proteins/ clusters of proteins denominated as ionic channels or ionic pumps, which are the responsible to maintain ions concentrations in both sides of the membrane, inside and outside the cell, and thus, these different concentrations result in an electrical potential across the membrane, the membrane potential. The presence of ionic channels and ionic pumps confers a semipermeable character to the membrane, which is permeable to specific ions [7]. As previously mentioned, in the rest state, the resting membrane potential value is negative which means that the intracellular potential is more negative in relation to the extracellular potential. This can result in an electrical field across the membrane and we can see the cell membrane as a natural capacitor. Another important concept is the equilibrium potential which is defined as “the membrane potential at which current flow due to electric forces cancels the diffusive flow” [25]. This is correlated with another two important events: ions diffusion and electrical drift of the ions. Simplifying, ions diffusion is the movement of particles according to their gradient of concentration, i.e., they diffuse from a region with high concentration to another with low concentration. However, this phenomenon is related to another one, the ions electrical drift. As ions are charged particles, as they move down the gradient, and once the ions concentrations are different in both sides of the membrane, the generated electrical field influences the movement of the ions which leads to an electrical drift of the ions according to their charges in an opposite direction despite their concentrations gradients. For instance, if one side of the membrane has an excess of positive charges in relation to the general amount of charges (positive and negative ones), the flow of ions positively charged even in favor of their gradient of concentration tend to invert and flow in the opposite direction of diffusion because, eventually, the amount of negative charges that stay in the initial side will increase the electrical field and as we know, opposite charges attract each other and same charges repel each other. So, this to say that the system is in equilibrium when the movement of ions due to electrical drift is equal but opposite to the movement due to diffusion [7]. At this point, it is possible to measure the equilibrium potential for a specific neuron. The equilibrium potential is also known as Nernst potential due the Walther Nernst, a German physical chemist who created, in 1888, the famous equation to compute the equilibrium potential for a single ion. The Nernst equation is described below:

$$E_x = \frac{RT}{z_x F} \ln \frac{[X]_{out}}{[X]_{in}}, \quad (1)$$

where, E_x is the membrane potential of the membrane permeable ion (X), R is the universal gas constant, T is the temperature in Kelvins, z_x is the valence of the ion, F is the Faraday's

constant and $[X]_{out}$ and $[X]_{in}$ are the ion concentrations in the extracellular and intracellular fluid, respectively.

The Goldman-Hodgkin-Katz (GHK) current equation, developed by Goldman in 1943 and Hodgkin and Katz in 1949, predicts the current of a specific ion (X) across the cell membrane for a specific value of membrane potential (V), per unit area of membrane (in cm^{-2}). This equation is presented below and has the following assumptions: ions pass through the membrane independently of each other and the electric field within the membrane is constant [7]:

$$I_X = P_X z_X F \frac{z_X F V}{RT} \left(\frac{[X]_{in} - [X]_{out} e^{-z_X F V / RT}}{1 - e^{-z_X F V / RT}} \right). \quad (2)$$

The remaining parameter: P_X is the permeability of the membrane to the abstract ion (ion X, for the example). This equation is often substituted by a simpler one:

$$I_X = g_X (V - E_X), \quad (3)$$

where g_X is the conductance per unit area ($mS cm^{-2}$) and E_X is the equilibrium potential. The total current flowing across the membrane is the sum of the GHK current equation for each ion, which cross the membrane.

Another important concept is the reversal potential (E_m) and is defined as “the membrane potential at which the current reverses direction” [7]. Despite its similarity with the equilibrium potential, when there are ion channels that are not truly selective to just one type of ion, its value will be in the middle of each equilibrium potentials of the ion types which can pass through the ion channel [25]. When the V is equal to the E_X , the current is zero as we can see in equation (3). So, this moment corresponds to the current turning point and by replace the membrane current by zero and solve the GHK current equation in order to voltage, it was created the GHK voltage equation presented below and applied to a membrane permeable to 3 different ions (Na^+, K^+, Cl^-):

$$E_m = \frac{RT}{F} \ln \frac{P_{Na}[Na^+]_{out} + P_K[K^+]_{out} + P_{Cl}[Cl^-]_{out}}{P_{Na}[Na^+]_{in} + P_K[K^+]_{in} + P_{Cl}[Cl^-]_{in}}. \quad (4)$$

2.1.2. Hodgkin and Huxley model

An AP can be quantitatively described by a set of equations developed by Hodgkin and Huxley in 1952 [7], [26], and which are nowadays used as the basis of computational models in neuroscience. They proposed an equivalent electrical circuit for a membrane cell's compartment and is present in figure 2.1.

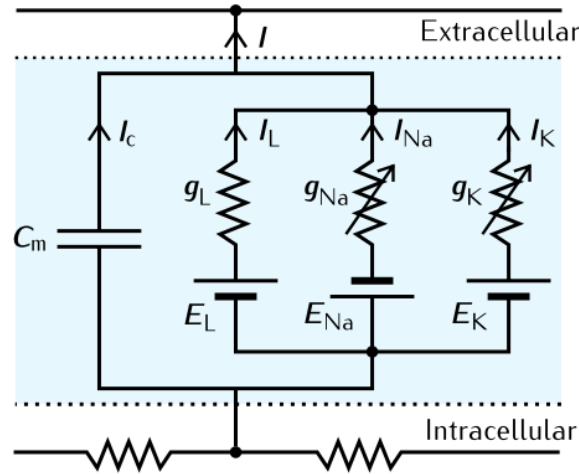


Figure 2.1 - Hodgkin and Huxley equivalent electrical circuit for a membrane cell's compartment. Adapted from [7].

First, to clarify, ion channel is a term used nowadays but unknown to the authors of the model when they did their studies. I just will use it to facilitate the understanding of the readers. In this model, the cell membrane is represented by a capacitor (C_m) and is also represented by three different ionic currents, the sodium current (I_{Na}), the potassium current (I_K) and the leak current (I_L), this one, is mostly due to the current resulting from the flow of chloride ions. The three ion channels are represented by a resistance in series with a battery. E_{Na} , E_K and E_L are the equilibrium potentials correspondent to sodium, potassium and the leak ions and their respective conductances are g_{Na} , g_K and g_L . An important aspect is the arrow above the sodium and potassium resistors which means that the value of their conductances vary with voltage and we can see that solving the equation (3) in respect to g_x . Despite the lack of technology in that time, now we know that there are voltage-gated ion channels. The circuit in the figure 2.1 has the corresponding equation:

$$I = I_c + I_i, \quad (5)$$

where I is the membrane current, I_i is the ionic current and corresponds to the sum of the individual ionic currents of the three types of currents previous mentioned and each individual current can be calculated through the equation (3) and, I_c is the capacitive current which is given by the membrane capacitance multiplied by the voltage's rate of change $\left(\frac{dV}{dt}\right)$ as in the following equation:

$$I_c = C_m \frac{dV}{dt}. \quad (6)$$

Hodgkin and Huxley after their experiments knew that sodium and potassium ions were responsible to generate an electrical impulse so they tried to fit the ionic current generated by each one. First, they noticed that the conductances of the ions depended on the membrane voltage. Additionally, they created the idea of gates on the membrane which enable the passage of ions across it and, the gates had two states, the open and the closed state. These

are controlled by a number of independent particles called by the authors as gating particles and they change their state according to the membrane potential. Like the gates, they have the same two states, open and closed and for an ion cross the gate, all the gating particles need to be in their open state. By calculation of the conductances for each ion (potassium and sodium) obtained in their voltage clamp experiments through isolation of the current corresponding to each ion, for the specific case of the potassium ions, they defined the gating variable n as the probability of a potassium gating particle be in its open state and the probability of the gate be open is n^x . Thus, being \bar{g} the membrane maximum conductance, the membrane conductance for potassium, given the probability of the gate be open, is written as:

$$g_K = \bar{g}_K n^x. \quad (7)$$

By fitting the experimental potassium conductance curve obtained led the authors to assume that the potassium had four gating particles ($x = 4$). They did the same thing to the sodium ion, however, they observed that the behavior of the conductance curve was different of the potassium curve. They observed that despite the voltage continued being applied to the membrane, the sodium conductance after reached its maximum started to decay, a phenomenon named by the authors as inactivation. So, they conclude that instead one gating particle, they should use two. They introduced the gate type particle which characterizes the level of inactivation and it is represented by h . Also, like the gating variable n used for potassium ion, their homologous for sodium is the sodium activation particle m . Thus, by curve fitting they got to the following equation for sodium membrane conductance:

$$g_{Na} = \bar{g}_{Na} m^3 h. \quad (8)$$

The last current, as previously discussed, is the leak current resulting from the permeability of the membrane to chloride ions. Through the equation (3) it is possible to model the leak current. Just for a question of conformity with respect to the last equations, the membrane conductance g will be replaced by \bar{g} . Finally, Hodgkin and Huxley equation [7], [26] to describe the membrane potential, in a small part of a squid giant axon, used in their experiments is present in the equation (9) and results in the combination of the equations (5), (6), (7) and (8):

$$C_m \frac{dV}{dt} = -\bar{g}_L(V - E_L) - \bar{g}_{Na} m^3 h(V - E_{Na}) - \bar{g}_K n^4(V - E_K) + I_{LC}. \quad (9)$$

Once this equation is just for a part of the axon, I_{LC} corresponds to the contribution of the axial current from the vicinity regions of the axon. Considering all extension of the axon, this current can be replaced by the second derivate of the membrane potential solved in order to space:

$$\frac{d}{4R_a} \frac{\partial^2 V}{\partial x^2}.$$

2.1.3. Integrate and fire model

Models capable of capturing the key elements of the dynamics of neuronal networks are challenging to develop and to analyze. Computational models which are appropriate to reproduce single cell's behavior frequently fail in the context of neuronal network analysis simply because they are not adequate for representing network dynamics, or because they are computationally intensive (and do not scale up to population sizes). Further, depending on the scientific questions, for instance, understanding in detail the mechanisms of how neurons are capable to process and transmit APs, are not truly important [7]. These explanatory models can be replaced by descriptive models where it is described the essential function of the neuron, in this case, the genesis of APs through non-coupled differential equations which is computationally faster [7]. The construction of a model requires an active process of simplification, and a criterions judgment of what are the essential elements to capture in the model, and what elements are secondary. Therefore, simplified models are very useful, especially in neuronal networks simulations.

The Hodgkin-Huxley model, HH-model, which describes AP generation using differential equations for each state variable, as previously addressed, is capable to explain with detail various events that occur in the membrane, such as the behavior of different ion channels due to the dynamics for the gating particles related with their conductances. Such mechanisms involving the voltage-dependent Na⁺ and K⁺ conductances to generate an AP are well-understood. However, if the biophysical mechanisms responsible to generate an AP are not explicitly necessary in a model, the model can be simplified and simulations' duration will reduce radically. The integrate-and-fire model, IF-model, which does not include gating variables, is a much simpler model capable of modeling the membrane potential dynamics. Lapicque proposed it in 1907 even when the mechanisms that generate an AP were not well-understood yet [25]. Despite the complexity associated to the generation of an AP, this model sees it as a phenomenon that happens every time the membrane potential reaches a threshold value between -55 to -50 mV, and consequently, a spike is initiated [7], [25]. After that, the membrane potential is reset to a value below the threshold potential.

There are many versions of this model. A version very similar to the original one proposed by Lapicque is used in this present dissertation work, the leaky IF-model, which only cares about the dynamics of subthreshold membrane potential. Unlike to what happens in the HH-model, all active membrane conductances are ignored, being the membrane modeled as a passive leakage term [25]. The membrane's current is given by the following equation:

$$i_m = \overline{g_L}(V - E_L), \quad (10)$$

where $\overline{g_L}$ is the membrane leakage conductance, V is the membrane potential and E_L is the membrane equilibrium (or resting) potential. This current is called leakage current and is the current resultant from all elements that contribute to the membrane's resting potential such as the different ionic channels [25]. Also, it is important to notice that both E_L and $\overline{g_L}$ are not

specific from any ion, and usually, they can be experimentally measured for the cell type which will be modelled [25].

According to the leaky IF-model, there is a membrane which is being charged through currents, flowing into it until it fires an AP; when the potential threshold is reached, the membrane discharges [7]. To better understand how this model works we should look to the figure 2.2.

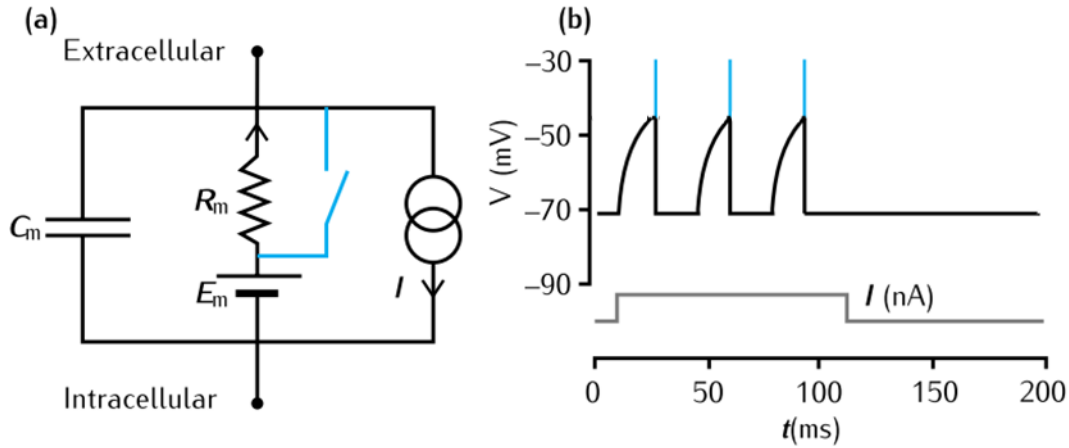


Figure 2.2 - Schematic representation of the IF-model. a) Representation of the IF-model in the form of a circuit diagram. In blue is represented a switch which closes when the membrane potential reaches a threshold voltage, which means that the neuron fired a spike. The switch when closing causes a “short circuit” on the membrane resistance, taking the membrane potential back to the resting potential. (b) When a spike is fired, marked by the blue line, the membrane potential is reset to the resting potential and, despite the current still be injected in the circuit, the switch only opens after a certain time (refractory period), allowing the membrane to charge again and if it reaches the threshold, another spike will be fired. Adapted from [7]

The model can be seen as an RC circuit, which is used to model the passive properties of the membrane, including a spike generation and a reset mechanism within it. A switch represents this last mechanism. When V reaches a certain threshold level (V_{th}), is considered that the neuron fired an AP and consequently the switch closes, bringing the membrane potential back to the resting potential (E_m) [7]. After the refractory period, the switch opens letting the membrane to charge again and hence, the potential increases again [7]. This behavior is illustrated in the figure 2.2(b).

The complete leaky IF-model equation is given by:

$$\tau_m \frac{dV}{dt} = E_L - V + R_m I \quad (11)$$

$$\text{if } V > V_{th}: \text{"spike fired"} \text{ and } V = E_L,$$

where τ_m is the membrane time constant of the neuron and is equal to $R_m C_m$, R_m is the membrane resistance, I is the injected current (from an electrode or from other synapses) and $E_L = E_m$ [7], [25]. The figure 2.3 shows the behavior of this model when subject to a current from an electrode (I_e), which changes in time.

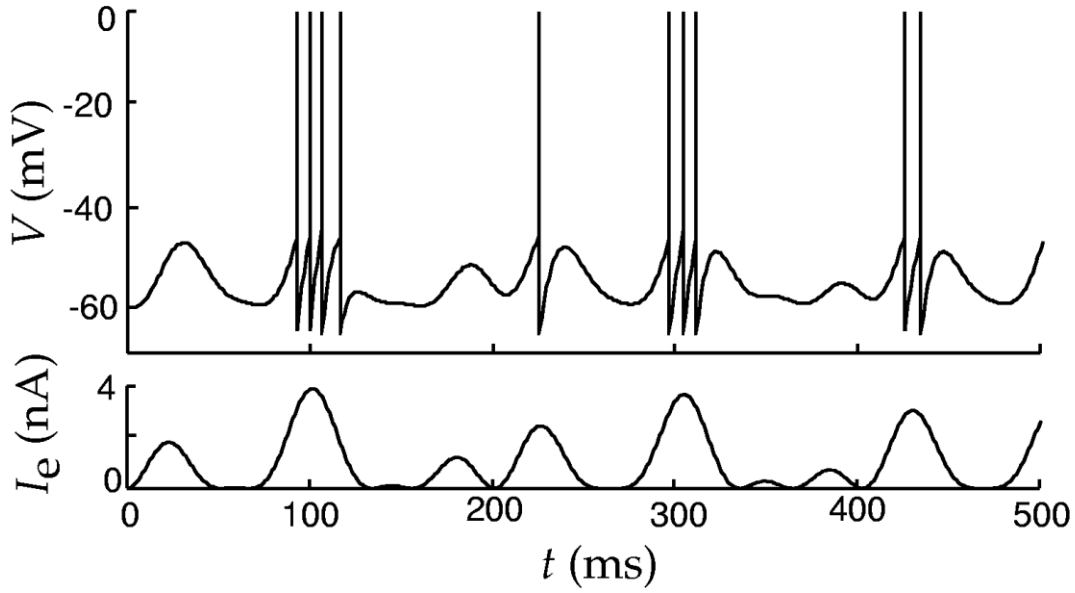


Figure 2.3 - The leaky IF-model response to the variation of the electrode's current over the time. The parameters used in the model were: $E_L = V_{reset} = -65 \text{ mV}$, $V_{th} = -50 \text{ mV}$, $\tau_m = 10 \text{ ms}$ and $R_m = 10 \text{ M}\Omega$. On the top, is the result of the membrane potential as result of the injected current (on the bottom). Adapted from [25].

By integrating the previous equation in a situation where the injected current is constant it is possible to obtain the membrane potential which is given by the equation 12 [7].

$$V = E_m + R_m I \left(1 - \exp \left(-\frac{t}{\tau_m} \right) \right). \quad (12)$$

The greater the current is, the sooner the voltage will cross the threshold and the voltage is reset. And, the process starts again. If a constant current above the threshold is injected into the model, the simulated "neuron" will fire at a constant frequency [7].

The model's firing rate can also be calculated using the equation 13 [25]:

$$r_{isi} = \frac{1}{t_{isi}} = \left[\tau_m \ln \left(\frac{R_m I + E_L - V_{reset}}{R_m I + E_L - V_{th}} \right) \right]^{-1}, \quad (13)$$

where r_{isi} is the interspike-interval firing rate, t_{isi} is the spikes' period and V_{reset} is the reset potential, which is typically made equal to E_L . The figure 2.4 shows the relation between the interspike-interval firing rate (r_{isi}), in Hz, and the injected current from an electrode, in nA, for an IF-model neuron and a cortical neuron measure *in vivo*.

If we solve the equation 13 in order to I , it is possible to determinate the necessary current to inject in the system, capable to make the simulated neuron fire with a specific firing rate. Considering $E_L = V_{reset}$ and $t_{isi} = (1/r_{isi}) \times 1000$, in ms, the resultant equation (14) gives the current in nA:

$$I = \frac{(E_L - V_{th}) \times \left(e^{\frac{t_{isi}}{\tau_m}} \right)}{\left(1 - e^{\frac{t_{isi}}{\tau_m}} \right) \times R_m}. \quad (14)$$

Naturally, the leaky IF-model is not perfect, and one of its limitations is the absence of the experimentally observed spike rate adaptation. The figure 2.4 (a), compares the firing rates

as a function of injected current. Through the equation 13, it is possible to obtain this relation. In 2.4 (a), it is possible to observe that the IF-model, represented by the line, is in accordance with the rates between the first two spikes fired by a real neuron, after being stimulated with a constant current (filled circles). Although, for the same constant injected current in a real neuron, it adapts its firing rate in response to the stimulus, increasing the spikes period until hit a steady-state duration. The open circles represent the steady-state firing rate. In figure 2.4 (b), it is demonstrated the spike-rate adaptation of the neuron. Still, there are more complex IF-models that could fit these more complex dynamics of the neurons [25].

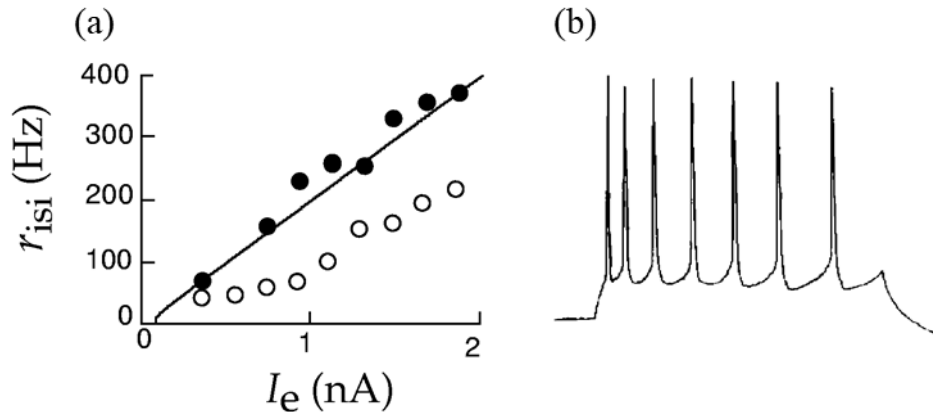


Figure 2.4 - IF-model vs experimental results. (a) Relation between the interspike-interval firing rate (r_{isi}), in Hz, and injected current from an electrode, in nA, for an IF-model neuron and a cortical neuron measure *in vivo*. The parameters used in the model to draw the line were: $\tau_m = 30\text{ ms}$, $E_L = V_{reset} = -65\text{ mV}$, $R_m = 90\text{ M}\Omega$ and $V_{th} = -50\text{ mV}$ [25]. The filled dots represent the r_{isi} between the first two spikes fired by the measure neuron in response to each level of constant injected current. On the other hand, the open circles show that the r_{isi} steady-state of the neuron is the result of its adaptation to the current. This spike-rate adaptation can be observed in (b), where is demonstrated the spiking behavior of a cortical neuron during a constant current. It is possible to observe the increase in the spikes period. Adapted from [25].

In summary, in this section, two different models were reviewed. The first one, HH-model uses a system of differential equations to characterize the membrane potential and the voltage-dependent conductances from membrane's ion channels which are responsible for the generation of spikes and, in the second model addressed, IF-model, it is imposed that every time the membrane potential reaches a certain threshold value, an AP occurs [7], [25].

2.1.4. From neuroscience to neuroengineering

Over the last 60/70 years, the NS has intrigued the neuroscientist community because of its complexity and lack of knowledge of its clear behavior, unlike other human systems. As result, the search for answers has led to the development of new technologies and approaches to study and better understand this human system [2]. Electrophysiology science dates back to the second half of the 18th century. Benjamin Franklin was one of the first electrotherapists who tried to use electricity with a medical purpose to treat neurologic disorders and in 1759 he was capable to see muscles' contraction due to an electrical shock [27], [28]. In 1780s, Luigi Aloisio Galvani during his experiment, he noticed that the leg muscles of a dead frog started to

twitch when an electrical shock was applied to its nerves and, later, in 1791, he introduced a new concept called as animal electricity, which involved physiological processes like muscle contraction and nerve conduction [29]-[31]. In the 1930s, Howard Curtis and Kenneth Cole, using an intracellular micropipette were capable to measure the full AP of a squid giant axon [29], [32]. Hodgkin and Huxley, in 1939, recorded an intracellular AP from a squid giant axon [33]. Also, both, in 1952 suggested the existence of “ion channels” [34]. This was later confirmed due to patch-clamp invention by Erwin Neher and Bert Sakmann in the late 1970s [35]. The first MEA was proposed by Thomas et al., in 1972, for extracellular recordings of in vitro cultured embryonic chick heart cells [36]. Gross et al. [37], [38] in 1977 developed a new MEA system capable of simultaneous single-unit recording of extracellular activity from snail's brain ganglia. Jerome Pine reported in [39] the usage of an array capable to record APs from single dissociated rat superior cervical ganglion neurons with a good signal-to-noise ratio (SNR), for cells at a maximal distance of 40 μm from the electrode. To be able to record signals, he penetrated the cell with an intracellular micropipette to stimulate a cell near an electrode. The APs generated were simultaneous extracellularly and intracellularly recorded and correlated [39]. After technological and materials' advances, in 1994, Nisch et al. reported a new planar MEA with 60 gold microelectrodes to monitor the electrical activity of neurons in cell culture [40]. And, in 1998, Egert et al. using the planar MEA60 developed a novel system of organotypically cultured rat hippocampal slices [41], capable of simultaneous recording and stimulation of long-term cultures (4 weeks). They were able to record either spontaneous and evoked local field potentials (LFPs) and single-unit APs in all of 60 electrodes. The MEA60 is commercially available since 1996 by MCS and is one of the most requested MEA devices [3]. In 1999, Oka et al. [42] developed a planar MEA with 64 microelectrodes capable of electrophysiological recordings in acute hippocampal slices, which they called as Multielectrode dish (MED) probe and is commercially available as MED64 by Alpha MED Scientific Inc. (Japan). Figure 2.5 shows the differences between MEA60 and MED64 devices.

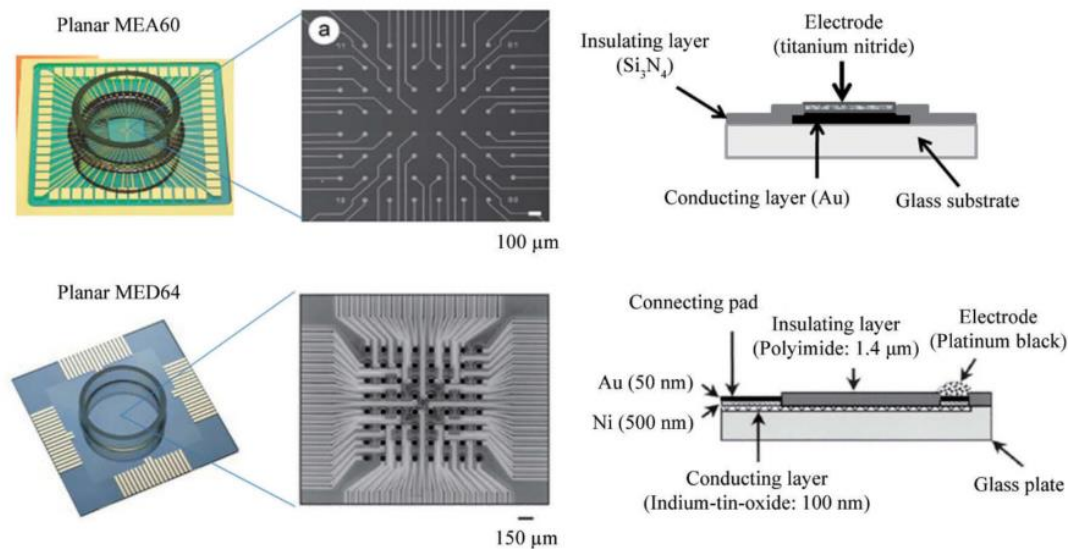


Figure 2.5 - Schematic representations of the planar MEA60 chip and the planar MED64 chip. The planar MEA60 chip (on top) is composed of 60 microelectrodes and the planar MED64 chip (on bottom) has 64 microelectrodes. These models were the first versions of the current commercially available chips. On the right, are described the different layers and materials of each chip. Au is gold, Si_3N_4 is silicon nitride and Ni is nickel. Adapted from [3].

2.2. Introduction to standard electrophysiological devices and types of signals

Although there are other methods to study neuronal activity, the more relevant methods within the neuroscience community are the intracellular recordings and stimulation by sharp or patch electrodes and extracellular recordings and stimulation by substrate-integrated MEAs [8].

Among the extensive repertoire of electrophysiological signals present in neuronal cells and populations, the most important to be considered in the present work are the APs, the LFPs and bursts, which will be discussed below.

An AP is considered the code/language used by neurons to transmit information and is a biophysical phenomenon that happens when the transmembrane potential of a neuron reaches a certain threshold level. This can occur due to stimuli or other inputs like synapses. A signal from an AP is called a “spike” and is nothing more, nothing less than a voltage signal [5], [43], typically recorded as a millisecond-long 80-100 mV spike in cell’s membrane voltage [2]. This kind of event is of the all-or-nothing type and it has unidirectional propagation along the cell.

The flow of currents in the extracellular space generated by APs events can be explained by the volume conductor theory. There is an extracellular medium with low uniform resistance surrounding the neuron, this medium is the volume conductor. The figure 2.6 exemplifies what is the current flow behavior around an isolated axon in a saline bath in two different situations. In the first, the axon is in its rest state (figure 2.6(a)), the membrane potential is uniform and there is no current flowing inside or outside the cell [43]. The second case is when the axon is

depolarized at some point in its membrane and the potential difference between the depolarized spot and the adjacent resting regions creates current flows (figure 2.6(b)). Heinricher [43] describes the depolarized region as a current “sink”, and the adjacent membrane to that region is called as “source” of current because it will be the origin of the current that will flow into the depolarized region. If an electrode is near the axon’s membrane in the depolarized region, it will record a negative signal in relation to a distant reference electrode. However, if the electrode is placed in the called “source regions”, the signal will be positive [43]. Figure 2.7 demonstrates this current flow in an easier way.

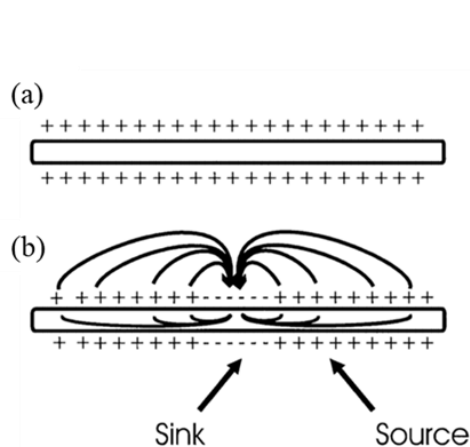


Figure 2.6 - Current flow around an axon described by the Volume Conductor Theory. (a) The axon is in its rest state and there is no current flowing. (b) One region of the axon is depolarized (“sink”) and there is a flow of current to that region from adjacent regions which act as a “source” of current. Adapted from [43].

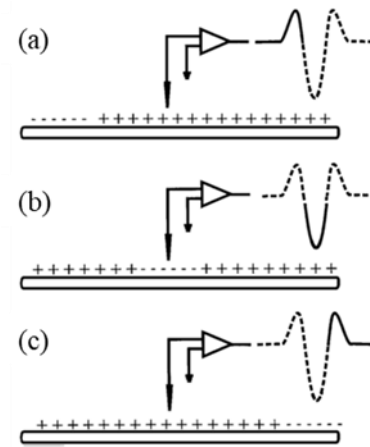


Figure 2.7 - Recorded current flow along an isolated axon predicted by the Volume Conductor Theory results in a triphasic waveform. (a) An AP is moving in the direction of an electrode placed in a region acting as a “source”. The electrode records a positive potential in relation to distant reference electrode. (b) The AP reaches the electrode’s position which is near to a depolarized region and thus, the recorded potential is negative. (c) The AP continues its propagation along the axon and moves away from the electrode what results in another positive potential. Adapted from [43].

Which ions are involved and what is the kinetics of ionic currents are two important questions. An AP is characterized by an initial and fast influx of sodium ions (Na^+) which results in a large negative spike in extracellular recordings named extracellular action potential (EAP). Contrariwise, this Na^+ influx is expressed as a positive spike in intracellular recordings and known as intracellular action potential (IAP). After this initial flux of Na^+ , the slow potassium (K^+) channels enable the efflux of K^+ which results in a small positive spike in the case of EAP and in a latter negative valley in IAP [5]. Figure 2.8 compares the shape of intracellular and extracellular APs over time.

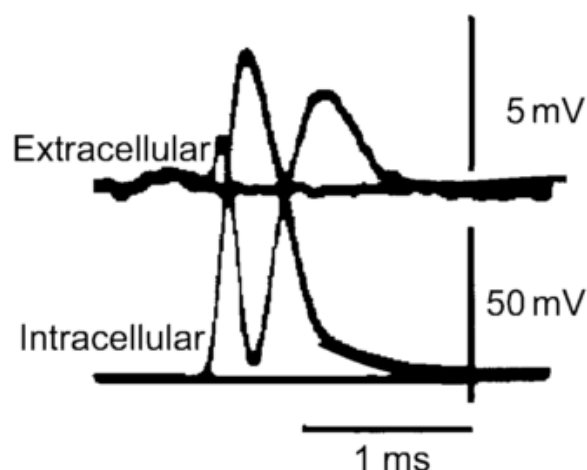


Figure 2.8 - Intracellular and extracellular spikes recorded simultaneously. The intracellular electrode records a monophasic depolarization wave which corresponds to a signal with a triphasic waveform in recordings using an extracellular electrode. Also, signals amplitudes are completely different. Adapted from [43].

IAP can only be detected intracellularly, this is, inside the neuron through a patch-clamp assay for instance. This direct access to the interior of the cell results in recordings of IAP at tens of millivolts. Whereas, EAP can be recorded putting an electrode near the site of spike's source (~100 micrometers), and typically the electrodes are placed in the perisomatic area (around the soma or near the axon initial segment) [44]. EAP measurements are around tens to hundreds of microvolts. Both, IAP and EAP, have a duration inferior to 2 ms [45]. EAP frequency band is located between the 300 and 3000 Hz [46].

LFPs, also known as field potentials, is the name given to a set of electrical current synchronized events that occur in neuronal populations in both time and space and typically is due to spike activity of individual neurons (superposition of fast APs), synaptic potentials or even slow potentials of glia cells [8], [45], [47]. LFPs characteristic duration is about tens of milliseconds [47]. A study authored by Shoham et al. [48], reveals that some parts of the brain have high percentages of neurons that do not fire APs or are firing at very low rates (<0.16 spikes per second) [48]. This emphasizes the importance of subthreshold synaptic potentials in signaling processes within the neuronal networks and that the neuroplasticity is influenced by variations in the amplitude of these signals [8], [49]. If they do not reach the threshold to fire an APs they are "ignored" by conventional extracellular electrodes [8], [48], [50] and important information may be lost. These signals are part of the content of recorded signals and appear in the low-frequency band, usually under the 300 Hz [45], [51]. Typically, when signals are analyzed, this content is filtered by a high-pass filter and frequency components below 300 Hz are removed.

Bursting or burst firing is a phenomenon usually recorded in networks of neurons. To better understand this phenomenon, we should look at the single neuron scale. This occurs when a neuron fires APs at high frequency during a period of time and, after that, is proceeded by a quiet period. Burst activity and burst rates are two important features extracted in recorded data by MEAs, both in single neurons and in networks of neurons. Two important factors that can trigger bursts are the environment, this is, the activity of neuronal networks and, the

neuron's phenotype. In the point of view of a neuroscientist, burst activity is related to different functions such as synchronization of neurons populations activity, motor pattern generation and transport of information [5]. Also, scientists associate the repetition of specific patterns as memory traces that appear by similar stimulus or as a result of internal processes [52]-[54].

2.2.1. Intracellular devices (patch-clamp and intracellular sharp microelectrodes)

Development of intracellular recording and stimulation technologies enabled researchers to better interpret the “language” used by neurons to communicate and transmit/exchange information with each other, mainly the information behind subthreshold synaptic signals [33], [55]-[57]. Patch clamp and sharp-intracellular microelectrodes are powerful resources to record APs, subthreshold and synaptic potentials with a high SNR [8], [43], [55] and have a very good electrical coupling with the cell [8]. Patch-clamp or sharp microelectrodes enable the study of a single neuron and its functions through direct measurement of intracellular voltage and, patch-clamp is also used to measure the ionic currents of single ion channels [5]. The tips of sharp intracellular electrodes are pushed through the cell's plasma membrane and contact directly with the cytosol. Patch electrodes tips when introduced break the plasma membrane of the cell and make direct contact between cell's cytosol and the interior solution of the patch electrode [8], [55], [56]. Current injections through these electrodes can stimulate intracellularly the neurons and also study biophysical parameters such as membrane capacitance, input resistance and synaptic properties like the reversal potential [55]. Although this technique is a very powerful tool in electrophysiology to study neuronal activity, its usage is limited to a few neuronal cells per experiment [8], [58] and is impossible to record and stimulate hundreds of individual neurons simultaneously [8], [59].

The current bulky micromanipulators used to insert the electrode's tip into the target cells limit the use of sharp or patch microelectrodes for parallel recordings or stimulation from many neurons [5], [8], [55]. Besides, intracellular recordings and stimulations provoke damages in the plasma membrane, which get worse with time and thus limit the duration of the studies. Also, perfusion of the cytoplasm in the case of patch electrodes can change the intracellular composition of the neurons [55], [56]. These mechanical instabilities in the cells are the major barriers of intracellular devices to perform investigations for long periods of time, namely when is necessary to monitor long-term events related to neuronal plasticity and learning [8]. Contrariwise, using extracellular and non-invasive technologies such as the extracellular MEAs can avoid these problems of mechanical and enable recordings and/or stimulations of large populations of electrogenic cells during days or even months [55], [60], [61].

2.2.2. Extracellular devices: standard planar-MEAs

The use of planar MEAs systems has been increasing in recent years due to their capability of simultaneous, parallel, non-invasive, multisite and long-term recordings of the electrical activity from populations of neurons at millisecond time scale [5], [62], [63]. This technology is capable of recording LFPs and EAPs and can also emit ES to modulate the normal/abnormal neuronal activity [5]. They can be used in *in vitro* recordings without inducing mechanical damages on the plasma membrane of the cells due to the extracellular position of the electrodes. This is one of the advantages of these systems that enables long-term recordings and stimulation of large populations of excitable cells [47], [60]-[62].

Extracellular recording technologies have also critical disadvantages in relation to the conventional intracellular ones. The major disadvantage is the relative low SNR and the coupling coefficient between single neurons and extracellular electrodes [8], [55], [62], [63]. Standard extracellular electrodes were limited to recordings of LFPs generated by APs [64], [65]. LFPs' amplitudes vary between 10 μ V to 1 mV [8]. Also, MEAs attenuate and temporally filter the electrical signals due to the averaging of LFPs which contributes to loss of information, changes in shapes, amplitudes, and patterns [8], [63]. Membrane level events from single neurons such excitatory or inhibitory subthreshold synaptic potentials, that can influence cell's excitability without firing an AP or even, membrane voltage oscillations, cannot be detected by the standard MEAs [8], [43], [62], [66]. This limits the understanding of neuronal networks. If synaptic potentials, in a neuronal network, are generated synchronously by populations of neurons, they can be picked [67], but this is very rare [66], [68]. Despite the technological developments and efforts to increase the number, density and spatial organization of MEAs [5], [47], [60], the SNR is still poor [69]. Figure 2.9 presents an overview of the electrophysiological signals recorded by standard intracellular and extracellular electrodes.

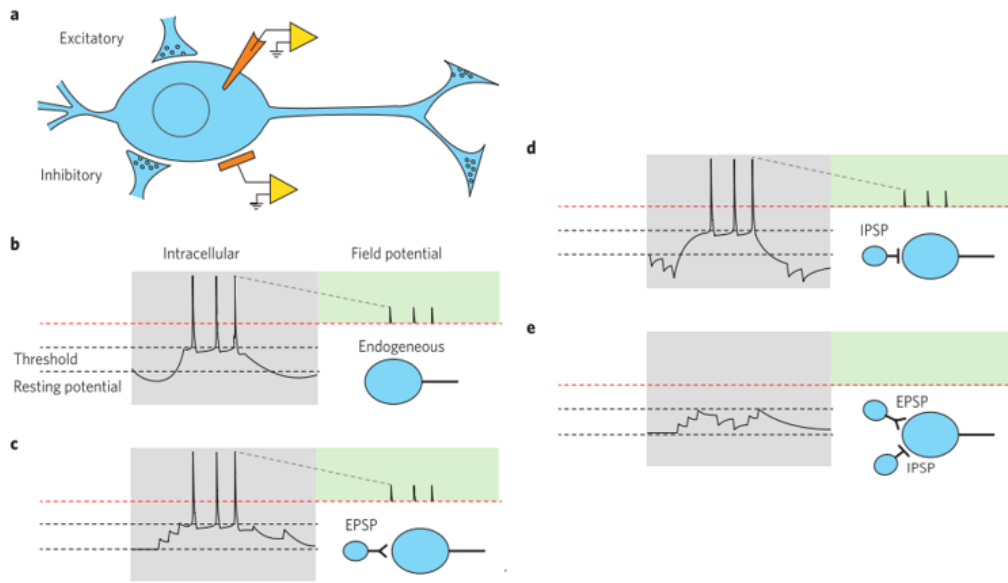


Figure 2.9 - Overview of intracellular and extracellular signals recorded by intracellular and extracellular devices. (a) The neuron (in blue) is regulated by endogenous excitatory and inhibitory synapses. In orange are represented an intracellular electrode (on the top) and a planar extracellular electrode (on the lower). Both to record and connected to an external amplifier (in yellow). (b) A train of APs is generated endogenously when the membrane depolarization reaches a specific threshold level. APs and all variations in the membrane potential resulting from subthreshold potentials are recorded by the intracellular electrode, the extracellular one is only capable to record LFPs resulting from generated APs. Note that the level of attenuation in extracellular recordings is very large compared with intracellular recordings, so, the recorded signals are not to scale. (c) APs are generated due to EPSPs and the sum of these inputs evoke the generation of APs while, in (d), when IPSPs inputs stop, there are generation of APs due disinhibition. Despite these two scenarios are completely different, for the planar extracellular electrode are exactly the same once both result in the recording of identical LFPs. (e) There are no APs due to the inhibitory and excitatory inputs received by the neuron, however, contrariwise to the extracellular electrode, the intracellular device is capable to record the variation of subthreshold potentials. Adapted from [8].

2.2.2.1. Equivalent electrical circuit of the neuron-electrode interface

In the figure 2.10, it is represented a passive equivalent electrical circuit of the interface between a planar MEA and a neuron. The interface is composed by a neuron, an electrode and the cleft between the neuron and the substrate surface where is insert the electrode. The cleft is filled with an ionic solution [8]. About the circuit, considering a single neuron, its plasma membrane is divided into two different parts each one represented by an RC circuit: the junctional membrane (jm) which corresponds to the part of the membrane that contacts with the sensing pad where the electrode is inserted and its resistance and capacitance are represented by R_{jm} and C_{jm} , respectively. The other part of the membrane that faces the bathing solution and the substrate (but not the sensing pad part) is the non-junctional membrane (njm) and its resistance and capacitance are represented by R_{njm} and C_{njm} , respectively. The electrode is represented by the resistance R_e and the capacitor C_e . Lastly,

the cleft has a resistance called as seal resistance (R_s). In simulation models, current injections are placed between R_{njm} and R_{jm} [8].

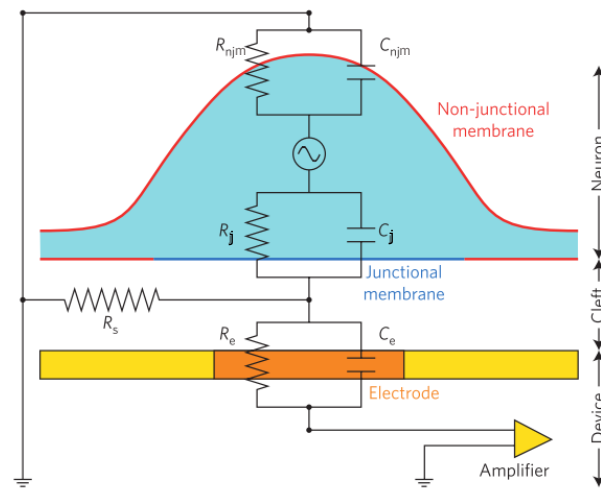


Figure 2.10 - Passive equivalent electrical circuit of the interface between a planar MEA and a neuron. The neuron, in blue, is on the top of the culture substrate, in yellow, and the neuron's body is over the electrode, in orange, which is inserted in the substrate. The electrode is connected to an amplifier. Cell's membrane is divided in two parts: the junctional membrane (jm) - faces the electrode- and the non-junctional membrane (njm) - faces the substrate and the bathing solution. The two parts of the membrane and the electrode are represented, each one, by a RC circuit where R_{jm} and C_{jm} , R_{njm} and C_{njm} , and R_e and C_e are the resistances and capacitances of the jm, njm and the electrode, respectively. R_s is the resistance generated by the physiological solution. Adapted from [8].

One of the most critical electrical properties to consider when using extracellular electrodes, which limits the effective electrical recordings of cells' activity is the value of the seal resistance (R_s). This value is determined by the thickness, the resistivity of the material within the cleft and the surface area of the cleft formed between the electrode and the cell's membrane [55], [65], [70], [71]. According to Hai et al. [72], the cleft thickness between different cell types and sensing pads have an average value between 30-40 nm. Conventional intracellular techniques are capable to generate an effective R_s with values ranging from hundreds of MΩ to a few GΩ [8]. More, the conductance of the junctional membrane is also important.

2.2.3. Extracellular recordings with MEAs: technical considerations

2.2.3.1. Stimulation

MEA systems can also include stimulation circuitry. Apart from allowing passive observation of neuronal activity through recordings, MEA systems can also influence actively and control the activity of neuronal cells and neuronal networks. These bidirectional systems should use the same electrodes to both stimulate and record, in order to reduce the number of electrodes and to achieve a high spatial coupling for input and output mapping of neuronal networks [22].

There are two different modes to deliver stimulation pulses: voltage-mode stimulation or current-mode stimulation [5], [16]. In the first one, the voltage is set precisely as a function of time but the current can vary freely. In the second case, the roles are inverted and, the current is established as a function of time and, the voltage can vary between a range of safety pre-defined values [16]. It is crucial that stimuli do not damage the cells [55]. Stimulations using intracellular sharp glass electrodes or patch electrodes are not difficult and there are well-defined protocols to current injection in neuronal cells. However, the use of extracellular high impedance electrodes to stimulate is more complicated. Due to charge transfer to the plasma membrane it can cause damages to the cells by irreversible electroporation [8], [55], or by irreversible electrochemical reaction [8], [55]. To avoid these situations, delivery of weak capacity stimuli trains to the cells activate local sodium currents capable to generate cell's depolarization and consequently reach APs' firing threshold [55]. Despite this approach is safe in terms of cells viability, it can constrain stimulation protocols where precise timed and consecutive stimulations are needed [55].

One problem of ES is due to the fact that stimulation pulses' amplitudes (volts) are much bigger than the recorded extracellular signals (microvolts), between three to four orders of magnitude, which results in stimulation artifacts in the recording electrodes during and after application of an ES pulse [5], [16], [22]. Some neuronal responses to a stimulus can occur in less than 1 ms after the delivered stimulus [73] and, in the case of the same recording and stimulation electrode, unless it is capable of rapid recovery from stimulation artifacts, the neuronal response will not be recorded [22], [73].

If the coupling between stimulation and recording is purely capacitive, the artifacts will only prevent recordings during the stimulation period. In addition, an artifact can have a big amplitude and cause the saturation of the amplification circuits of the recording electrode, which prevent recording for a period of time after the stimulation ended. This situation happens very often when a recording electrode is near a stimulation electrode [5].

It is important to know how to deal with stimulation artifacts. If the stimulation artifacts do not completely saturate the amplifiers, it is possible to remove this non-desired information from the acquired data by subtracting the estimated artifact using templates, filters or local curve fitting in appropriate software [74], [75]. If saturation occurs, there are different manners to solve the problem. One of them is to return the normal state of the saturated amplifier in the fastest way, so that the recording may continue without interferences from undesired signals. This is achieved by resetting the high-pass filter of the front-end amplifier [76], [77], with a "reset" switch. Also, instead of removing the artifacts from the recording electrode, another option is to eliminate the origin of the artifacts in the stimulation electrode.

2.2.3.2. Noise and signal-to-noise ratio (SNR)

SNR is one of the most important specifications of the MEA system and should be considered. When designing a MEA system is very important to realize what introduces

noise/interference to the circuit and where, and, if this noise will enter in the stage of amplification. Next, possible sources of noise will be discriminated:

- Biological noise: this noise is also known as background noise and results from the electrical activity of other cells around the recording electrode, ionic activity and synaptic noise due to the stochastic nature of synaptic transmission. For instance, the same recording electrode could be detecting APs from distant neurons and also subthreshold events in neurites of cells near it. LFPs are considered biological noise and therefore they are removed by filters and, thereafter spike analysis is performed [5].
- Electrode-electrolyte interface noise: one source of noise is the liquid-metal interface between the electrodes and the biological environment. At frequencies below 10 Hz, the electrode generates noise with a steep roll-off of $1/f$ or even $1/f^2$ [5], [78]. Frequencies above that are more relevant and are associated with thermal noise [79].
- Device noise: the process of amplification and digitalization of the recorded signals also adds noise. The design of the front-end amplifier is extremely important because the amplification stage should guarantee that the acquisition system doesn't limit the system's performance due to the noise. Another step that introduces noise to the system is the analog-to-digital conversion (ADC) of the recorded signal by the ADC MEA system. This quantization noise is part of the quantization error introduced by ADCs when a continuous signal is sampled in amplitude into discrete steps and, the value of this noise is usually an approximation of $1/\sqrt{12}$ times the magnitude of the least significant bit. ADCs used in MEA systems have at least 8-bit of resolution and, in the case of the ADCs are outside the MEA chip, are usually used ADCs with 16-bit or higher resolution [5]. The power supply line also contributes to noise. This noise is picked up between the microelectrode and the connection to the amplifier in the bandwidth between 50 to 60 Hz and is due to the high input impedance of the amplifier at that frequency. One mode to reduce this noise is to reduce the distance between the amplifier and the electrode [5]. More appropriate grounding and shielding can help to diminish the undesired recorded interferences.

2.2.3.3. Effect of electrode size, distribution and density

Published works report microelectrodes sizes ranging from 5 to 50 micrometers in diameter [6]. Bigger electrodes have more possibility of reaching neuronal cells and even contact with them physically which will increase the recorded signals' amplitudes, i.e., record higher spikes. Also, larger electrodes can reach more cells and consequently, pick up signals from different neurons at the same time. Still, these electrodes are not recommended to spatial studies once they can hide localized peak signal of a neuron more distant by smaller signals from a cell near the electrode [5].

The size of the electrode has an influence on its impedance ($Z_{\text{electrode}}$) and consequently influences electrode's noise. Larger electrodes have better SNR and smaller attenuation of the signal due to large $Z_{\text{electrode}}/Z_{\text{amplifier}}$ ratio. One disadvantage is that larger electrodes will pick signals from a bigger area and measure the average potential which results in a reduction of the peak signal amplitudes. However, smaller electrodes have higher noise levels, mainly due to thermal noise;

In the frequency band of 300-3000 Hz, the band for EAP recordings, the noise associated to the electrode is mostly thermal noise. This noise is smaller but can be even less if the electrode is bigger than 5 micrometers of diameter and/or is treated with some sort of coating. The ideal electrode size for *in vivo* applications taking into consideration the neuronal background activity was studied by Camunás-Mesa and his collaborator through simulations [80]. For their parameters and excluding the electrode's noise, the optimum size is about 40 micrometers.

Active electronic components integrated on the substrate where are the electrodes give the possibility of a large increase in the number and density of electrodes in MEAs. Complementary metal-oxide-semiconductor based high-density MEAs (HDMEAs) have been emerging in electrophysiological studies to mapping neuronal activity including activation sequences, localize single cells and create full-compartmental neuronal models through high-spatiotemporal-resolution data of single neurons, enabling the study of their contribution in the activity of the neuronal populations [5], [47]. Impact of spatial electrodes distribution and type of cells in recorded signals by HDMEAs [47]: (1) Electrode-neuron distance: the smaller the distance is, the higher is the recorded signal; (2) Extracellular space resistivity: the higher the resistivity is, the higher the signals; (3) Neuron size: larger cells need more membrane current to depolarize thus, produce bigger signals compared to small cells; (4) Type of "target" (cultures/tissue) [47]: dissociated cultures (the cells are closer to the electrodes what increases the signal); culture density (larger signals are recorded in cultures with high density in relation to low-density cultures. In high-density, cell's membranes are very close to each other which increases the extracellular space resistance); tissue slices (compared to cells in culture, recordings with tissue yield significantly small signals. Cell debris between viable cells and the electrodes are the main responsible).

2.2.3.4. Electrodes' impedance

Electrodes' impedance is one of the most important features to take into account when designing a MEA. Higher the electrodes' impedance, higher is the Johnson-Nyquist noise, in other words, is the thermal noise [16], [79].

Impedance is inversely proportional in relation to the size of the electrodes, this is, increase the surface area reduces the impedance. Since the development of the first MEA [36], [37], increasing the number and density of electrodes, by reducing the surface area of the sensing pads, has been adopted by many labs [47], [60], [61], [81] with the goal of improving

the spatial resolution of the devices. MEA's electrodes are built necessarily in the smallest size possible, micrometer scale and more recently nanoscale, which is a big limitation to achieve electrodes with low impedance. So, to reduce the electrode's impedance and consequently improve neuronal recordings, one strategy is to increase the effective surface area of the electrodes [5], [16]. This is achieved by using conductive materials with porous to modify the surface of the electrode, which increases its surface area and decreases the impedance. Some examples of these materials are the Pt-black, Au, carbon and conductive polymers like poly(3,4-ethylenedioxythiophene) [28], [82]. In addition, different nanostructures are often used to increase the electrode's surface area, in literature we can find some examples as gold nanoflakes/nanopillars, carbon nanotubes, and nanostructures as spongy platinum black or Ti_3N_4 [28], [83], [84]. Besides electrodes should be fabricated with a low level of impedance, their value of impedance must be similar to all electrodes across an array to avoid discrepancies of readings inside the array and to get reliable and consistent data. Low impedance increases the SNR, with the usual target SNR of 5:1 or higher [5]. Electrodes with low impedance can deliver more current with a small voltage level, which reduces the stimulation artifacts and are safer for the tissue/cells [16].

2.2.3.5. Electrical coupling coefficient in the neuro-electronic interface

Electrical coupling coefficient (CC) is defined as “the ratio between the maximal voltage amplitude of a signal recorded by the device (electrode-amplifier system) and the voltage amplitude of the signal generated across the plasma membrane of a neuron/excitabile cell” [8], [69]. The electrical CC is correlated with the concepts previously addressed.

As discussed above, neuro-electronic devices for electrophysiological studies, namely the ones with an extracellular position suffer from a weak electrical coupling. When in contact with an extracellular device the cells tend to form and preserve an extracellular cleft between their membrane and the substrate where they attach. The problem is that when there is an AP, the resulted current generated by the propagation of the event is shunted by the cleft. Reducing the cleft thickness may improve the electrical coupling [72].

Electrode's input impedance has a great impact on the electrical CC in the interface cell-electrode. The geometry and material of the sensing pad have an influence in the electrical CC and also in the electrode's impedance as previously mentioned.

Another manner to improve the electrical coupling coefficient in the neuron-electrode interface is to reduce its resistance. For instance, in the case of a very high value of R_{jm} and a small value of C_{jm} , just a small part of the current generated across the membrane of the neuron will flow through the junctional membrane and will be detected by the electrode [8].

Localized electroporation has been used to temporally increase the electrical CC through local increases in junctional membrane conductance [85].

The input impedance of amplifiers and the parasitic capacitance, also known as stray capacitance, of the conducting lines and electronic components are responsible for attenuations in recorded signals [8].

2.2.3.6. MEAs' Materials

MEAs are composed by various components distributed in different layers: the insulator and conductor layers, the microelectrodes and the substrate. Choosing the materials for each component is a very important task when projecting a MEA device, not only in terms of their performance in transducing the biological signals but also with regards to aspects of biocompatibility. Materials that are in contact or near cells and tissue need to be approved in cytotoxicity tests. Moreover, is also important to take into account what type of experiments in what will the MEAs be used, i.e., *in vivo* or *in vitro* experiments, for cultures or acute preparations, and what type of signals will be recorded, this is, if are EAPs and/or LFPs or IAPs, single-cell resolution or not. Finally, despite recordings, there is also interest in MEAs for stimulation, and in this case, the charge capacity of electrodes is important. Typically, electrodes are made with metallic conductors such as gold (Au), titanium nitride (TiN), platinum (Pt), stainless steel, aluminum (Al), and alloys like iridium oxide (IrOx) [5].

2.2.3.7. Amplifiers

Typical neuronal amplifiers should have the following features: its input impedance must be significantly higher than the electrode's impedance to guarantee the integrity of the input signals. In the case of the amplifier be in the same substrate where are the electrodes, temperature concerns are needed because substrate heating can damage cells or tissue which contacts. For that reason, should be taken into account the power characteristics of the amplifiers and chosen the ones which work with low power. Either, MEAs are used for a variety of applications which involve recordings of signals from a vast range of amplitudes, so, the amplifier' gain should be adjustable in order to be applied in different situations. Another dynamic range requirement is the frequency bandwidth. This must be flexible and enable recordings in a variety of ranges. For instance, sometimes is necessary to capture only lower frequency signals or spikes in the EAP band [5].

2.2.4. "In-cell" recordings using extracellular MEAs

To fill the gaps and overcome the limitations of standard planar MEAs, many labs started to merge the advantages of standard planar MEAs devices and the conventional intracellular microelectrodes [8] with the purpose to achieve "in-cell" recordings using MEAs, i.e., recordings with quality similar to that ones obtained by the conventional intracellular methods

[8], [9], [86]. One of the strategies proposed by several groups led to the creation of a new category of MEA devices - the 3D structured MEAs - which use micro- or nanometer scale structures protruding from the sensing pads. Some examples of these 3D structured MEAs can be found in the literature, for instance, nanowires (nanopillars) that reach the cytosol by penetrating the plasma membrane [9], [87], [88] or due to membrane electroporation [85], [89]. I will focus on other 3D structured based MEAs which use micrometer-sized extracellular gold mushroom-shaped microelectrodes.

There are three crucial aspects that should be respected to obtain this “in-cell” recordings using extracellular MEAs [8], [62]:

1. Activation of cell conserved mechanisms such as phagocytosis by which the cultured cells actively engulf the microelectrodes (they must have a 3D-shape and protrude from the flat substrate to enable the engulfment);
2. Establishment of a high seal resistance (R_s) between the cell's membrane and the engulfed electrode [72];
3. Localization of ion channels in the plasma membrane that interface with the electrode (activation or recruitment of ion channels in that region can increase the local conductance in the junctional membrane).

2.2.4.1. Gold Mushroom-shaped microelectrodes (gM μ Es)

The demand for new approaches that allow a better interface between neurons and sensing pads led two investigators, Micha E. Spira and Aviad Hai, and their co-workers to create what they call as the “in-cell recording approach” and developed this new type of microelectrodes [55], [62], [72], [90], [91]. They investigated what are the microelectrodes' appropriate 3D geometry and dimensions to protrude from the flat glass substrate and have an intimate contact with the neurons. To achieve this contact, they created a micrometer-sized-3D-gold-microelectrode with mushroom's shape which protrudes from the substrate to a height of 1-1.5 micrometers (figure 2.11). Other groups are also capable to fabricate this type of microelectrodes [92], [93]. Their shape and size were chosen to mimic the shape and dimensions of post synaptic spine structures of vertebrate neurons' dendrites [72], [94], [95]. Also, the microelectrodes had their surface chemically functionalized with a specific peptide (RGD-based peptide) [96] to activate conserved cell biological mechanisms such as phagocytoses [97], which are induced in the interface microelectrode-neuron. Thus, instead of inserting a microelectrode into the cell, this process is done by the cell itself through phagocytosis (a conserved cell biological mechanism for the internalization of particles [98]). They found that the gM μ Es maintain their extracellular position in relation to the neuron's plasma membrane but the interface neuron-gM μ Es presents a tight cleft and a larger area of contact [72], [91] compared with the standard extracellular microelectrodes. More, they noticed that when neurons grow on gM μ Es there is an engulfment of the microelectrode by the

neuron and this results in a rearrangement of the actin cytoskeleton of the neuron which forms an actin ring around the stalk of the microelectrode [90]. The authors showed that arrays with these type of microelectrodes are capable of recordings with a good SNR of attenuated subthreshold synaptic potentials and APs from individual neurons comparable to intracellular recordings [8], [55], [62] and are also capable of effective stimulation [55], [62]. Through their efforts in several reported studies [55], [62], [72], [90], [91], they referred an increase of the electrical CC from a value of 0,1 % for experiments using planar extracellular MEAs to a significant value of 50% for experiments with chemically functionalized gMμEs. However, in those reports, they used cultures of *Aplysia* neurons, which have a big size and, was observed that neurons closely engulfed the mushroom-shaped microelectrodes what contributes to a high seal resistance (R_{seal}) [8]. However, other experiments conducted by Shmoel et al. with primary rat hippocampal neurons [63] using gMμEs, which surface was functionalized with polyethyleneimine (PEI) and laminin shown that there was a promotion of “self-assembly” of the gMμE by the cells however was not a complete engulfment of the electrode as happened with *Aplysia* neurons. Shmoel et al. called this “type of engulfment” as “loose-patch-like configuration”. The engulfment of gMμE by the cells allow multisite, high quality recordings of positive monophasic APs from mammalian neurons [63]. Reported studies where there is engulfment by mammalian cells can be found in literature for cardiac muscle cells (HL-1)[91], [93], embryonic fibroblast cells (NIH-3T3) [72], Chinese hamster ovary cells (CHO)[72], rat adrenal medulla cells (PC-12) [72], among others.

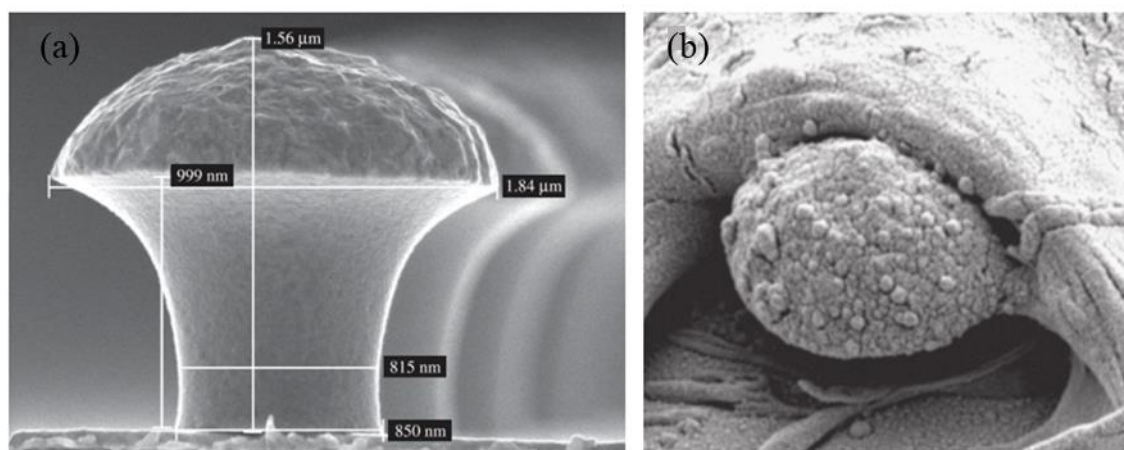


Figure 2.11 - Gold mushroom-shaped microelectrode (gMμE). (a) An example of gMμE's dimensions. It is composed by a ellipse-shaped cap in the upper part and the stalk which protrudes from the substrate (Adapted from [72]). (b) A neurite of an *Aplysia* neuron interacting with a gMμE (Adapted from [90]).

The most considerable differences between “gold standard” planar MEAs and gold mushroom shaped MEAs in cultured rat hippocampal neurons are present in the amplitudes and shapes of the recorded signals. Planar MEAs record LFPs comprising amplitudes in the interval between 40 to 100 μV with a SNR up to 5 and mostly with a negative peak or biphasic signals [5], [81], whereas, recordings with gMμEs based MEAs are mainly characterized by positive monophasic APs, with amplitudes, reported by Shmoel et al. [63], bigger than 100 μV , where

34.48% of the recorded signals were equal or bigger than 200 μV and 10.64% were bigger than 500 μV . Recorded signals' shapes and amplitudes from cultures on planar MEAs tend to change over the days in culture [81]. Unlike, signals recorded with gM μ E-MEAs maintain their spike shape (positive monophasic) over days [63]. However, their amplitudes can progressively increase, decrease or even disappear as consequence of the engulfment level between the neuron and the electrode, alterations in the cleft width formed in the interface neuron-electrode, movement of the neuron in relation to the electrode's position, changes in ionic channels distribution, expression and density in the neurons' membrane interfacing the electrode or even due cells death [63].

2.2.4.1.1. Equivalent electrical circuit of the neuron - gM μ E interface for recording and stimulation

A recent study conducted by Ojovan et al. [69], using SPICE simulation system, proposed a passive equivalent electrical circuit for the gM μ E-neuron interface and this model is presented in the figure 2.12. Next, the model will be described by authors' words: "In the model, the neuron's surface area is subdivided into a non-junctional membrane (njm, red) that faces the grounded culture medium, and a junctional membrane (jm, blue) that faces the electrode. Each of these membrane compartments is represented by a resistor and capacitor in parallel R_{njm} , C_{njm} , R_{jm} and C_{jm} , respectively. The cleft formed between the neuron and the electrode is represented by a resistor (the seal resistance - R_s). The electrode is represented by a resistor and capacitor (R_e and C_e , respectively)" [69]. The values of the parameters can be obtained from direct measurements, normally by the use of classical intracellular recording electrodes such as patch or sharp microelectrodes, or even by calculations of the physical parameters that fit the specific geometry of the microelectrodes and the neuron-gM μ E interface [55]. The value of the seal resistance determines the coupling between the neurons and the gM μ E and, for values below 100 M Ω , the CC is drastically reduced [55]. The junction interface between the neurons and the microelectrodes has high bidirectional electrical coupling which enables recordings with quality and SNR similar to the classical intracellular methods and also stimulation with milliseconds duration of single pulses. Besides the engulfment suffered from the microelectrodes, another phenomena can be responsible for the improvement of the electrical coupling, and investigators have reported that the geometry of the gM μ E can improve the conductance of plasma membrane in the junctional membrane (part of the cell's membrane that faces the gM μ E) [69] due to the activation or recruitment of ion channels in that localization [55], [90] (membrane convex curvature leads to local cytoskeleton rearrangements and alters the mechanical tension on the two sides of the lipid bilayer which activate ion channels or increase the local conductance [8], [99], [100]). Further, microelectrodes' extracellular position is maintained which does not compromise the mechanical stability of the cell and so, the recordings can last for a longer period of time [55]. This set of modifications can be observed in the figure 2.13.

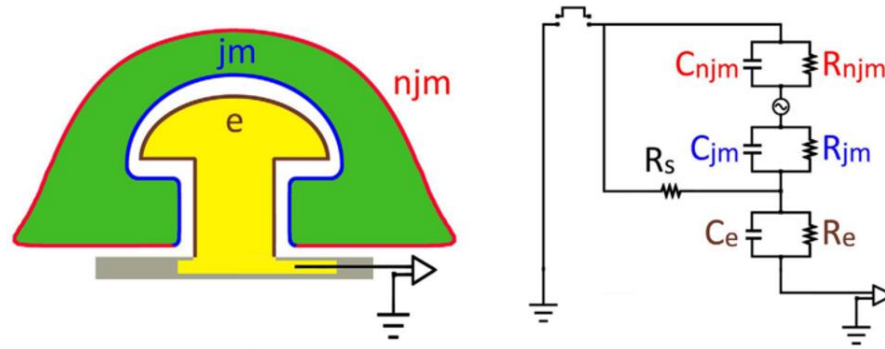


Figure 2.12 - Passive equivalent electrical circuit for the gMμE-neuron interface when the neuron completely engulfs the gMμE. The neuron, in green, totally engulfs the gMμE, in yellow, which protrude from the substrate. The electrode is connected to an amplifier. Cell's membrane is divided in two parts: the junctional membrane (jm, blue) - facing the electrode- and the non-junctional membrane (njm, red) - facing the culture medium. The two parts of the membrane and the electrode are represented, each one, by a RC circuit where R_{jm} and C_{jm} , R_{njm} and C_{njm} , and R_e and C_e are the resistances and capacitances of the jm, njm and the electrode, respectively. R_s is a resistor and represents the cleft formed between the neuron and the gMμE. Adapted from [69].

The main ideas retired from Ojovan et al. 's study [69] are that increasing the diameter of the gMμE cap results in larger electrical CC values, however, increasing the stalk diameter decreases this effect. Also, the CC is inversely related with the thickness of the cleft formed between the neuron and the electrode, i.e., CC value declines as the thickness increases [69]. Hai et al. in their experiments [55], [62] were capable to record AP with amplitudes close to 20 mV and synaptic potentials of approximate 2 mV, with an attenuation of approximately 25% with respect to the input potential [55], [62] that corresponds to a high CC level. Simulations performed by Ojovan et al. [69] suggested that to obtain this value of CC obtained by Hai et al., they needed to lower their value of R_{jm} by a factor of 1000, which emphasis even more the idea (described above) that when neurons engulf the electrode, the curvature formed in the junctional membrane contributes to increase the density of ion channels in that region [8], [62], [99], [100], which increases the membrane's conductance and, in turn, reduces the value of the R_{jm} , justifying in this way the differences of CC obtained in the simulations [69] in relation to that ones obtained experimentally.

Hai and his collaborators [55] conclude that there is an unprecedented good CC between neurons and the engulfed mushroom-shaped microelectrodes in respect to other extracellular MEAs approaches and also, they reported that injections of current sufficient to reach the firing threshold of the neurons are possible without cause damages in the plasma membrane [55].

It is important to understand that many times the electrodes are not engulfed by just one cell. One single electrode can be contacted or even partially engulfed by different neuronal elements such neurites or cell bodies, and therefore, this implies deep alterations in the CC in the interface neurons/neurites - gMμE [69]. For the case of the electrode is partially engulfed, the equivalent electrical circuit proposed by Ojovan et al. [69] is shown in the figure 2.13. Similar to the model presented in the figure 2.12, the cell membrane is represented by two parallel RC circuits. However, the electrode is represented by two RC circuits in series, one for

the electrode's part engulfed by the neuron and the other circuit is for the part in contact with the grounded culture medium. Spike activity (APs recordings) of different neurons that partially engulf a single gMμE can be recorded [69].

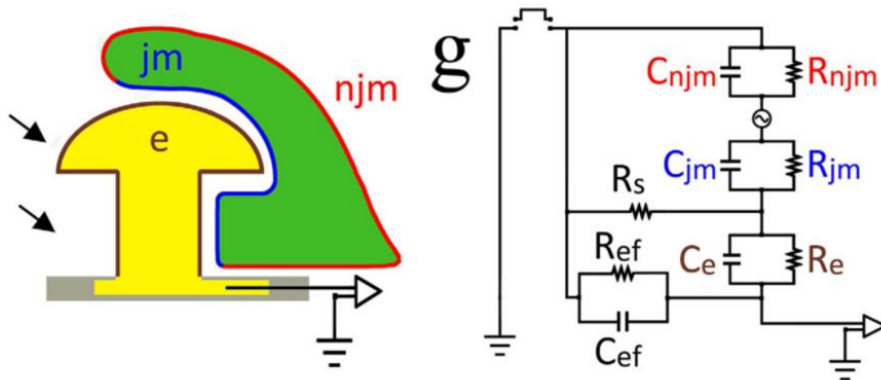


Figure 2.13 - Passive equivalent electrical circuit for the gMμE-neuron interface when the neuron partially engulfs the gMμE. The neuron, in green, partially engulfs the gMμE, in yellow, which protrude from the substrate. The electrode is connected to an amplifier. Cell's membrane is divided in two parts: the junctional membrane (jm, blue) - facing the electrode- and the non-junctional membrane (njm, red) - facing the culture medium. The two parts of the membrane, each one, are represented by a RC circuit where R_{jm} , C_{jm} , and, R_{njm} , C_{njm} , are the resistances and capacitances of the jm and the njm, respectively. The electrode is represented by two RC circuits in series. R_e and C_e are the resistance and capacitance of the part of the electrode which contacts with the neuron's membrane and R_{ef} and C_{ef} are the resistance and capacitance of the part of the electrode in contact with the culture medium. R_s is a resistor and represents the cleft formed between the neuron and the gMμE. Adapted from [69].

2.2.4.1.2. gMμEs based MEAs for in vivo applications

Until now, and mostly due to the recent existence of gMμEs based MEAs, there is no *in vivo* applications using this type of microelectrodes, however, considering future *in vivo* applications, they need to overcome some expected difficulties. One of them is mushroom electrodes' high impedance ($\approx 30 \text{ M}\Omega$) compared with neurons [2]. More, they should be capable to resist to sheer forces and maintain its mechanical stability during insertion into the brain tissue. Further, unlike *in vitro* applications where the cell culture is deposited over the MEAs' platform and the initial contact occurs due to the effect of gravity, in *in vivo* applications this first contact probably will need strategies like molecular signaling to attract the neurons or chemical functionalization of the electrode's surface to stabilize neuron-electrode bond, after contact [69]. Another issue present in *in vivo* is the presence of glia cells that tend to encapsulate foreign bodies, thus, they will compete with the neurons to engulf the gMμE and thereby, prevent the intimate contact between cells and the microelectrode [55], [69].

Chapter 3

Closed-loop system and PID controller

This chapter introduces the importance of closed-loop systems in neuronal control experiments and some strategies to process the recorded signals including the detection of APs. More, it describes one of the most versatile and widely used controllers in the world, the PID controller, that was used in this work to develop an *in silico* control system to modulate the firing activity of a simulated neuron.

3.1. Closed-loop systems

To understand this concept of closed-loop systems applied to neuronal experiments, we have to look to the neuronal circuits as part of a continuous sensorial-motor loop: the brain (CNS) - body (efferent PNS) - environment constitute the motor cycle and, the sensorial information returns to the brain by the opposite direction, environment - body (afferent PNS) - brain (CNS) [16]. Therefore, the NS is capable to understand the surrounding environment and take decisions depending on the sensing (input) information taken from that. Now, we can compare what happens in the NS and what is a closed-loop. Rolston et al. [16] defined a closed-loop as “a system where a sensed signal alters the system output which, in turn, may alter the sensed signals”. And, giving the example of the air conditioner, i.e., in a room, if a certain temperature is set, the thermometer sensor will determine if is necessary more or less cold air pumped by the device to reach that temperature, however, this is not a single event, is a continuous monitorization of the room’s temperature that can always be in constant change and adaptations have to be done by the equipment. This to say that we can use MEAs in closed-loop systems where the afferent sensorial information can be carried to the neuronal cells through ES, inducing plasticity or modulate cells activity; and, the efferent information from the cultured neurons on the MEAs is recorded and used to trigger ES [16], [101], [102] in abnormal scenarios or to control robotic prostheses for example [16].

In the clinical point of view, is expected that closed-loop systems will be more effective to treat neuronal disorders since the stimulation parameters will be adapted according to the state of each patient, in a continuous, real-time and dynamic way [16], [18]. The majority of the medical treatments using ES are open-loop systems, i.e., “a system which creates output regardless of external conditions, or which reads input and takes no action to affect further input” [16], and for these ones, stimulation parameters remain constant despite the disease’s state, like what happens in current DBS treatments in PD [18]. Another area where these systems are truly important is in prosthetics, where sensorial feedback can be achieved, for instance in a prosthetic hand, and consequently improve patient’s rehabilitation [16].

Real-time closed-loop experiments and BMI require the detection of spike trains in real-time thus, time-consuming spike sorting methods are a great barrier to achieve all potential of MEA devices capable of recording and stimulation [59]. The plasticity of neuronal circuits is the study goal of many labs. Memory and learning are associated with the precise timing of neuronal activity of populations of neurons, i.e., temporal patterns, and even, the timing of activity between single neurons [101]. Sometimes, this spike sorting is just a voltage threshold detection. Stimulation of specific neurons which depend on other neurons activity was successfully tried to control the bursting activity of neurons cultured on MEAs [103].

3.2. Signal processing and spike detection

MEA signals are recorded in their raw state, noisy, distorted and convoluted, thus, they should be treated and processed in order to extract the relevant information from them. Spike sorting is a term used for a set of steps to extract single-neuron spike trains from raw data [104], one of which includes spike detection, an important step in the rest of the proposed dissertation. However, it will be also described the normal steps of signal processing which include: data filtering, spike detection, and spike sorting.

- Filtering step: first of all, it is necessary to filter the raw data acquired by the MEA system. To do this is usually used a highpass or bandpass filter, usually with a bandwidth of 300-3000 Hz, with the purpose to remove the low-frequency components [65], [105]. Sometimes, the filtering process causes an alteration of the shape of the EAPs due to phase distortions.
- Spike detection: the most common and easy manner to perform spike detection is using an amplitude threshold [5], [22], [66]. There are different methods but, typically, a voltage threshold is established as $\pm(K \times Th)$ where K is usually 5 and Th is the threshold calculated by the chosen method, normally is the baseline noise level (root mean square (RMS) of the signals with a mean value of zero) [5], [22]. The MEA2100 system, that will be used in our experiments, follows this method. Another one, the adaptive median [105] is other method to define the threshold value but with a measure

based on the median and is used for recordings with a bigger number of spikes [22], [105].

- Spike sorting: this phase consists in grouping the spikes according to their shapes in clusters and occurs after spike detection [5], [47]. A neuron will be distinguished according to the characteristics of its spike shape, grouped in the cluster with that features and separated from different neurons with other spike shapes. However, spike sorting methods/algorithms are not very optimized and effective yet and therefore they need user supervision to correct possible errors due for instance, it is possible to occur a mismatch of the electrodes relative to neurons due to some movement between them which will alter the recorded signal [5], [66]. This electrode's drift is a big problem for long-term recordings, as well as changes in the environment surrounding the electrodes mostly because of growth or movement of glia cells [66]. Two examples of techniques for extract shape features that have been used are the principal component analysis or PCA [104] and the wavelet transform [106]. Ideally, the advances in such algorithms will be able to run in real-time to continuous monitoring the recorded data and be used in closed-loop therapeutic treatments which involve, for instance, ES, and be also applied in BMI such as neuroprosthetic devices [59], [66].

3.3. PID Control

When talking about closed-loop systems is important to do a brief introduction to PID controllers. PID controllers are not the focus of this dissertation work, but they are used here in a proof-of-concept of how to control neuronal spiking behavior through a PID controller using a mathematical model, to simulate neuronal behavior. Yet, its features should be understood and, in this chapter, I will give a small introduction about how they work and their main components/variables. An example of how this classical control method can be used to control the firing rate by modulating the interspike interval of a neuron can be found in [107]. There, they used a linear proportional and integral (PI) controller to achieve that purpose. Another example, this time for application in PD can be found in [108]. Gorzelic et al. used a PID controller to obtain an improved DBS algorithm [108].

3.3.1. The feedback principle

First, before talking about how PID controllers work, it is important to introduce a few concepts used in a closed-loop system to understand when these appear further ahead. In the figure 3.1 is presented a block diagram of an unity-feedback system.

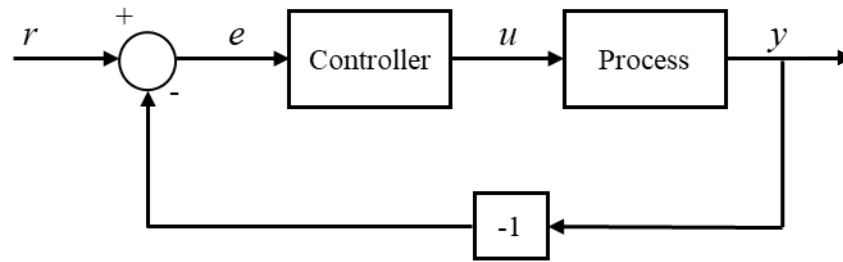


Figure 3.1 - Block diagram of a simple feedback system. The larger boxes represent the two major components of the system, the controller and the process. The control variable u is the input of the process and y is the output. At the beginning of the system, r is the setpoint. The controller's input is the control error e which is the difference between the process' output and the setpoint.

The larger boxes represent the two major components of the system, the controller and the process. These two components are related as we can see from the arrows that link them. Starting in the middle of the system, the control variable (or manipulated variable) u is the input of the process. Process' output y is the process variable. This variable is the parameter of the system that needs to be controlled, for instance, temperature, pressure, etc. At the beginning of the system, r is the setpoint or the reference value and it is the desired value of the process variable. Finally, the controller's input is the control error (e) which is the difference between the process variable and the setpoint ($e = r - y$). The error will be used by the control algorithm of the system to compute an update of the control variable while the controller is turned on [109], [110]. Therefore, a feedback loop system has the purpose of keeping the process variable close to the setpoint, even when there is any disturbance in the system that could deviate the process value from the reference value.

Many areas in electronics, communication or instrumentation make use of this powerful technique called feedback control. According to Åström, K.J. and Hägglund, T., authors of the book "PID controllers: theory, design, and tuning" [109], the feedback control principle could be explained like this: "Increase the manipulated variable when the process variable is smaller than the setpoint and decrease the manipulated variable when the process variable is larger than the setpoint" [109]. If there is something that disturbs and affects the equilibrium of the system and, for some reason, the process variable becomes larger than the reference value (r), when the variable error is calculated, it will give a negative value that makes the controller output (u) to decrease and consequently, the process output (y) will also decrease. This particular type of feedback is called negative feedback because the control variable (u) moves in opposite direction to the process variable [109], and is usually represented in block diagrams by the sign-reversing block as we can see in the figure 3.1. Lastly, what makes feedback systems a really strong technique is that, despite the disturbance, the system will always try to bring the process variable the closest as possible to the setpoint, of course, if well designed and implemented [109], [111].

3.3.2. Components of a PID controller

Basically, a PID controller is the most famous control algorithm used in the world: more than 90% of the current industrial controllers are based on PID controllers, predominantly at lowest levels [112]. This popularity is due to the fact that PID controllers are easy to use, simple, could be used in a vast amount of applications and, at the same time, its clear functionality is also associated with robust results and “can thus be said to be the ‘bread and butter’ of control engineering” [109], [112]. Further, despite the technological developments since that the PID controllers were invented (beginning of 20th century), they still by far the most popular control algorithm and should be part of control engineer’s toolbox [109], [112].

As its name says, the PID controller has three control components, the proportional (P), integral (I) and derivative (D), and the controller’s output is the result of the calculation of each component and the sum of these three components as shown in the following equation [111]:

$$u(t) = K_p e(t) + K_i \int_0^t e(\tau) d\tau + K_d \frac{de(t)}{dt}. \quad (15)$$

The next figure shows how the controller can be introduced in the form of a block diagram of a feedback system where each component of the controller is described separately through each parcel of the equation above:

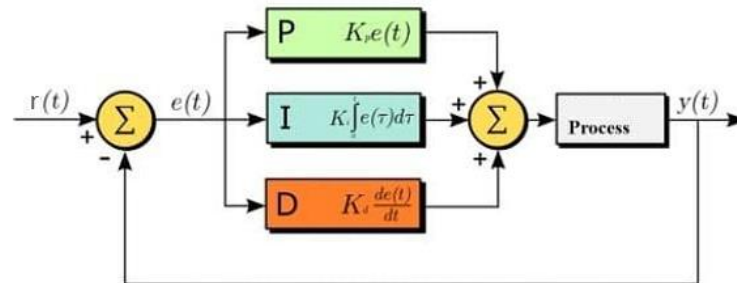


Figure 3.2 - A block diagram of a PID controller in a feedback loop. Each component of the controller is described separately with different equations. $r(t)$ is the setpoint, $e(t)$ is the control error and $y(t)$ is the measured process variable. Adapted from [113].

The three components in the equation act as separated modules of control and it is possible to have four different types of control: Proportional control (P), Proportional and Integral control (PI), Proportional and Derivative control (PD) and PID control. The type of controller should always be chosen according to the needs and properties of the system, it is not always possible to state that the three components together will do a better job than only two. More, keep the controller as simple as possible [112].

In the figure 3.3 is represented an example of a typical response of a PID control system in a closed-loop. Some terminologies that characterize the control system performance need to be introduced like the rise time which is the time that the system takes to go from 10% to 90% of the stationary state (final value). The overshoot is the value that the process variable

exceeds the final value, the steady-state value. The settling time is the necessary time for the process variable to settle to within a certain percentage (commonly 5%) of the final value. The steady-state error is the final difference between the process variable and the setpoint. Lastly, the deadtime is the delay between when the process variable changes, and when that change can be observed and, it is an undesired behavior of a control system, this should not occur [109], [112], [110].

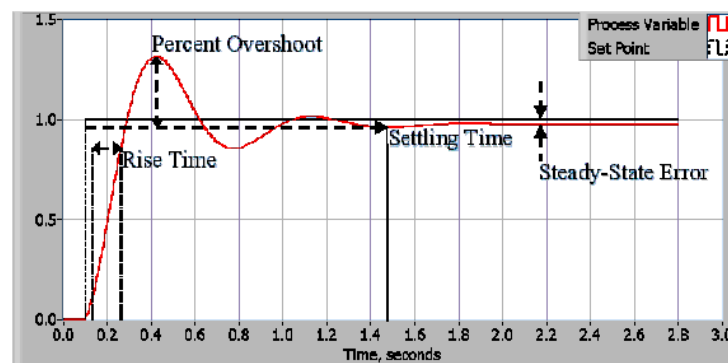


Figure 3.3 - Typical response of a PID control system in a closed-loop [110].

The **proportional** action of the controller adjusts the control variable proportionately to the error, where K_p is the proportional gain. Increasing this gain will increase the response velocity of the control system, however, if too high, the control variable could start oscillating and even, make the system unstable and stay out of control. Also, the overshoot tends to be larger. Further, if K_p is too small, the controller could fail to overcome the disturbs and to restore the system's equilibrium. It is important to highlight that the proportional control is only capable to reduce the steady state error and not eliminate it [109]-[112].

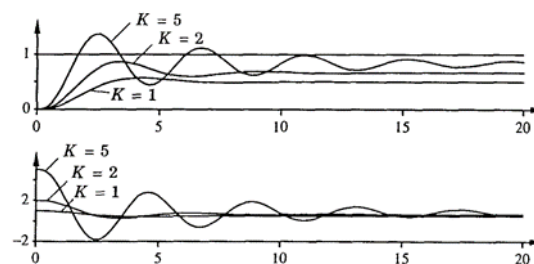


Figure 3.4 - Example of a closed-loop system with a proportional control. The upper diagram shows the action of the proportional gain (K) in the response curve (setpoint = 1). The lower diagram shows the control signal u for the previous K . Adapted from [109].

The **integral** action of the controller is proportional to the integral of the error, it sums the error over time, removes completely the steady state error and makes sure that, in the steady state, the process' output is equal to the setpoint. This integral component could compensate the steady state error of the proportional control since, no matter how small the error is, there is always an improvement of control. This component will increase or decrease over the time, unless the error is zero, what drives the steady state error to zero. But, it could

increase the overshoot. K_i is the integral gain. The “integral correction” can occur during regular intervals of time called integral time constant (T_i) and is defined as $T_i = 1/K_i$. This means that if the K_i is low, the system could take much time to reach the setpoint however, if K_i is too high, the system could become unstable similar to what happens with K_p [109], [111], [112], [110].

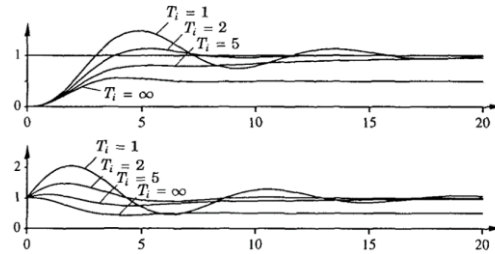


Figure 3.5 - Example of a closed-loop system with a proportional and integral control. The upper diagram shows the action of the integral component for different values of integral time T_i in the response curve (proportional gain is constant and setpoint = 1). The lower diagram shows the control signal u for the previous T_i . Adapted from [109].

The **derivative** action is proportional to the rate of change of the control error and this component brings to the system the ability of the controller to anticipate the error. K_d is the derivative gain. Thus, there is an anticipated correction of the error, which reduce the response time and improves the stability of the system. Similar to the integral component, the derivative controller also has a derivative time constant (T_d) which is used to estimate the control error at time T_d ahead. T_d is equal to K_d/K_p [111]. This is useful because, looking to the case of the proportional control, the process dynamics will always take some time to react to the outcome that, the control variable will introduce in the process output. And, to see this “delay” in correcting the error, we just need to look to what happens in the case of an overshoot, for instance. Therefore, the derivative action will predict what will occur to the process output further ahead taking the current rate of variation and projecting it to the future, trying to avoid future errors. Due to the sensibility of the derivative action, in noisy systems or when the systems need to respond very fast to a disturb, this component could make the system unstable because the inclination of some peaks of the noise could change very quickly, overloading the derivative controller [109]-[112].

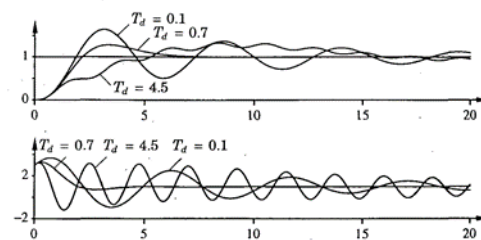


Figure 3.6 - Example of a closed-loop system with a proportional, integral and derivative control. The upper diagram shows the action of the derivative component for different values of the derivative time T_d in the response curve (proportional gain and integral time are constant and setpoint = 1). The lower diagram shows the control signal u for the previous T_d . Adapted from [109].

After introduced T_d and T_i , the controller can also be represented by the following equation [111]:

$$u(t) = K_p \left(e(t) + \frac{1}{T_i} \int_0^t e(\tau) d\tau + T_d \frac{de(t)}{dt} \right). \quad (16)$$

The theory of a PID controller is based on past, present, and prediction of future control errors as demonstrated in the figure 3.7.

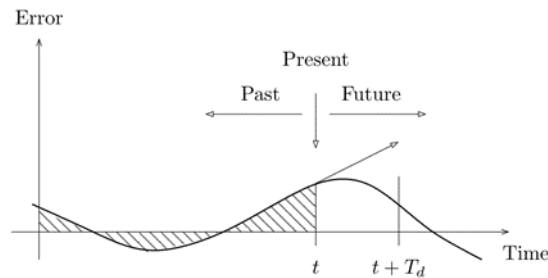


Figure 3.7 - PID controller's theory. A PID controller takes control action based on past, present and prediction of future control errors. Adapted from [111].

The proportional part acts on the present value of the error, the integral represents an average of past errors and the derivative can be interpreted as a prediction of future errors based on linear extrapolation, as illustrated in figure 3.7 [111].

The table 3.1 summarizes the individual effects of each component of a PID controller in a closed-loop system. Although, all components depend on each other and must be parameterized together through the tuning process [112]. The next topic will approach the importance of tuning these parameters and how it should be done.

Table 3.1- Effects of independent P, I and D tuning [112].

Closed-Loop Response	Rise Time	Overshoot	Settling Time	Steady-State Error	Stability
Increasing K_p	Decrease	Increase	Small Increase	Decrease	Degrade
Increasing K_i	Small Decrease	Increase	Increase	Large Decrease	Degrade
Increasing K_d	Small Decrease	Decrease	Decrease	Minor Change	Improve

3.3.3. Controller Tuning

Despite the individual features of each controller component presented in the table 3.1 seem to be clear, their effect could not be exactly like that when they are associated with each other. Thus, one of the most important things to do when designing a controller is to guarantee that each part improves the system's performance without compromise the other components' performance. Therefore, tuning the gains (K_p , K_i and K_d) is a crucial step to obtain the desired behavior. There are different ways to do that. I will only talk about two manual tuning methods. Although, in the literature can be found many others. For example, Panda et al. [114] provides

five different tuning rules, Shahrokh, M. and Zomorodi, A. [115] made a comparison between different tuning methods and the book “PID Controllers: Theory Design and Tuning” by Åström, K.J. and Hägglund, T., [109] is also a good source of knowledge about different types of PID tuning methods.

The first method could be considered primitive and consists of an adjustment of the parameters manually by a “trial and error” process like a step response method based on the input-output of the system. This is based on the fact that who is tuning the controller knows what the gains do to the system. First, the integral and derivative gains are set to zero and the proportional gain is increased until the system’s response starts to oscillate. Then the K_p should be set to approximately half of that value for a “quarter amplitude decay” type response [113]. After that, the integral gain is increased to stop the oscillations and reduce the steady-state error but could increase the overshoot. Once defined the proportional and integral gains to get the desired response, if necessary, it is time to increase the derivative gain to reduce the overshoot and increase the stability [110], [111]. Again, the derivative action of the controller is difficult to tune and sometimes could also become the system unstable. This is one of the reasons why the majority of used controllers are PI type controllers [112].

The second method is the Ziegler-Nichols’ method developed in the 1940s by John G. Ziegler and Nathaniel B. Nichols and, is one of the most widely used methods. Similar to the previous method, the integral and derivative gains are set to zero and the proportional gain is increased until the system starts to oscillate with a constant amplitude oscillation. This gain corresponds to the critical gain (K_c) and T_c is the period of oscillation. After many experiments and simulations performed by the authors of this method, the controller parameters were obtained and, the table 3.2 gives these parameters in terms of K_c and T_c [110], [111].

Table 3.2 - Controller parameters for the Ziegler-Nichols frequency response method which gives controller parameters in terms of critical gain K_c and critical period T_c . The parameter T_p is an estimation of the period of damped oscillations of the closed-loop system [111].

Controller	K_p/K_c	T_i/T_c	T_d/T_c	T_p/T_c
P	0.5			1.0
PI	0.4	0.8		1.4
PID	0.6	0.5	0.125	0.85

Although PID controllers are a classic method of control, the interest in this type of controllers has been growing through the recent years. This is mainly due to the appearance of automatic tuning. Sometimes there is no time, or even, lack of knowledge to develop detailed models of the processes of the systems [116]. Generally, engineers design their controllers in the frequency domain using the Laplace transform for continuous systems (described by differential equations) or the z-transform for discrete systems (described by discrete different equations). In the frequency domain, the system’s model is called a transfer function [107]. Many tuning methods assume that the process is completely known in terms of transfer

functions, step responses or frequency responses [116]. However, this is not true for the majority of people interested in design their own control systems. Although, today, there are available equipment and software with automatic tuning techniques capable to obtain process models quickly and easily; of course, it is only possible due to the current computational power, which did not exist when the classic tuning methods were developed. And, by tuning we are not talking only about of tuning the gains as previously addressed in this section. It refers to process identification and also controller's design [116]. To finish, two examples of tuning software are the INTUNE® tuning software [117] and the Simulink (MathWorks).

Chapter 4

Materials and Methods

4.1. Integrate and Fire model with a PID controller

One of the goals of this dissertation work is to create an *in silico* PID controller capable to modulate the neuronal activity of a simulated neuron through the injection of current, as a proof-of-concept. This section describes all the steps performed to reach this goal.

4.1.1. Choice of the mathematical model to simulate neuronal activity

The two models described in the chapter 2, subsections 2.1.2 and 2.1.3, were chosen to simulate the behavior of a neuronal cell. Both, the HH-model and the IF-model were implemented and simulated in MATLAB R2017b (The MathWorks Inc., USA). Right away, it was clear that the HH-model was computationally heavier and time-consuming, which is normal because is a more complex and detailed model compared with the IF-model, as addressed before. Furthermore, this proof-of-concept of how to modulate neuronal activity through current injection is focused on the cell's firing rate and thus, the only events that will be considered are the APs fired by the simulated neuron. Therefore, it is possible to extract the spikes using a model capable of modeling the membrane potential dynamics, without adding the dynamics of ion channels and their contribution to the membrane potential, which is the case of the IF-model. In addition, we noticed that the HH-model was very sensitive to the smallest current injected into the model by the simulated electrode. Such reasons led us to select the IF-model.

4.1.2. Integrate-and-Fire model implementation

The IF-model was implemented and simulated in MATLAB R2017b with the following parameters: $E_L = -70.0 \text{ mV}$, $R_m = 20.0 \text{ Mohm}$, $\tau_m = 10.0 \text{ ms}$. The total current flowing into the cell (I) is composed by the neuron's intrinsic current defined by I_{neuron} and the current injected by an external source, in this case, an electrode ($I_{electrode}$). Through the equation 14, it was set a firing rate of the simulated neuron of 10 Hz what corresponds to a current of approximately 1.000045 nA. At this point in the work, no external current source had been defined to inject current into the neuron. This current corresponds to I_{neuron} , being $I_{electrode}$ equal to zero. The differential equation dV/dt was calculated using Euler's method with $V_{t_0} = -70.0 \text{ mV}$, during a simulation time of 10 seconds with a discretization time (dt) of 0.01 ms. According to Euler's method, the code implemented to calculate the rate of change of membrane's potential was:

```
for i = 2 : nsteps

    % Euler's method
    V(i) = V(i-1) + dt/tau_m * (- V(i-1) + E_L + I * R_m);

    % Reset the membrane's potential when the neuron fires an action
    potential.
    if V(i) > E_thresh
        V(i) = E_L;
        spikes(i) = 1;
    end

end
```

where nsteps is the total time of simulation in milliseconds divided by dt. When the potential reaches the threshold potential, the neuron fires an action potential and the event is stored in the events vector called “spikes”. This vector will be used posteriorly to calculate the firing rate of the simulated neuron. This is done using a Gaussian kernel with a sigma (σ) of 100.0 milliseconds:

```
% kernel size
N = round(8*sigma/dt);

% kernel size must be an odd number
if mod( N, 2 ) == 0
    N = N + 1;
end
```

```
% Creates and applies the kernel
kernel = fspecial('gaussian', [N, 1], sigma/dt);
firing_rate= 1000/dt * conv(spikes, kernel, 'same');    %firing rate
[Hz]
```

4.1.3. Introduce the controller in the model

The next step was the addition of an external electrode capable to inject current in the model and modulate its firing behavior. To do this, we tried to implement in the model a PID controller to adapt the electrode's current in order to maintain the neuron's firing rate around a certain pre-specified value. Based on the theory behind this type of controllers that can be found in the Chapter3, we started by defining the scheme of the controller, which is presented in the figure 4.1.

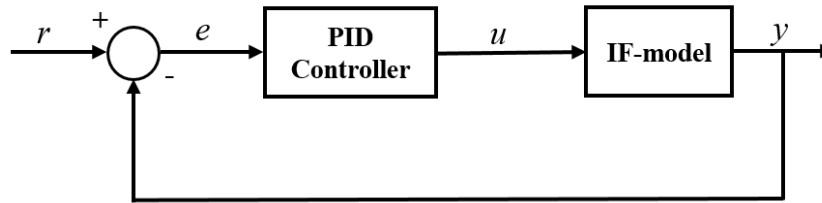


Figure 4.1 - A block diagram of the *in silico* PID control model. The boxes represent the two major components of the system, the controller (PID controller) and the process (IF-model). The control variable u is the input of the process and in our model is the current of the simulated electrode, y is the output (calculated firing rate). At the beginning of the system, r is the setpoint (desired firing rate). The controller's input is the control error e which is the difference between the firing rate computed at each iteration and the desired firing rate value.

In the figure 4.1, r corresponds to the setpoint value, the reference value for the desired firing rate of the simulated neuron. The controller is the PID controller responsible to adjust the electrode's current, which will be injected in the IF-model. y is the firing rate after the current adjustment. The equation 15, presents the way that the current is adjusted over the simulation time:

$$I_{\text{elect}} = (K_p * \text{error}(i)) + (K_i * \text{integral_error}(i)) + (K_d * \text{derivative_error}(i)) + d_{\text{electrode_dt}}(i-1); \quad (15)$$

First, starting with the proportional component of the controller, it is given by the proportional gain times the firing rate error. In the integral part of the controller, the strategy was to look to the integral as the sum of the errors over the simulation time, since $t_0 = 0 \text{ ms}$ until t_i (time of the current loop iteration), times the integral gain. Basically, the integral of the error is updated and stored in the vector called `integral_error` (`integral_error(i) = error(i-1) + error(i)`) that will be used by the function responsible to adjust the electrode's current.

The last component, the derivative term, is the derivative of the error times the derivative gain. First, we noticed that the error curve had some peaks that could introduce errors when

calculating the derivative. So, the next step was to apply a moving average filter to the vector where the errors had been stored and use the moving average of the error to calculate the derivative by calculating the rate of change of the error between the current iteration and a certain number of iterations before. This enables the controller to know how the error is varying over the time and tries to compensate it in the future. The last part was to update the electrode's current by adding the necessary current to compensate the error of the electrode's current that had been applied to the model in the iteration before.

Another feature that should be explained is the mode how the code updates the firing rate during the simulation. Initially, the model did not have a controller implemented in the code and the firing rate was calculated in the final of the simulation through a Gaussian kernel that runs the vector where the spikes are stored and estimates the firing rate. However, after introducing a controller in the system, it is necessary that at each iteration of the simulation there is a control of the current injected by the electrode in the model, thus, the firing rate should be updated in each iteration. In this case, it cannot be done using a Gaussian kernel because it estimates the firing rate using spikes fired before and after the current time of simulation. The Gaussian kernel, a non-causal filter, is defined by the probability density function [25]:

$$\omega(\tau) = \frac{1}{\sqrt{2\pi}\sigma_\omega} e^{\left(-\frac{\tau^2}{2\sigma_\omega^2}\right)}. \quad (16)$$

The temporal resolution is given by σ_ω . Reducing its value increases the temporal resolution, once the filter uses more finely spaced intervals of time to estimate the firing rate however, if the interval is very small it could not be capable to differentiate the transitions of the firing rates in a smooth way [25]. The next step was to change the type of filter used to calculate the firing rate and the encountered solution was to replace it for a causal kernel, instead of a Gaussian. This is truly important because, if we are monitoring the spiking behavior of the simulated neuron and using that to estimate the necessary current to modulate that behavior, we cannot use information about future spikes. One commonly form of a causal kernel is the α -function that is described by the equation 17 [25]. The temporal resolution is given by $1/\alpha$ [25] and in this work, since the temporal resolution used in the Gaussian kernel was 100 ms, when replacing it by the causal kernel, and to maintain the same resolution, the value of α used to design the kernel through the equation below was 0.01.

$$\omega(\tau) = [\alpha^2 \tau e^{(-\alpha\tau)}]_+. \quad (17)$$

The $[\]_+$ notation means that when the argument is negative, $\omega(\tau)$ is zero, it is called the half-wave rectification [25] and can be expressed like this :

$$[\omega]_+ = \begin{cases} \omega & \text{if } \omega \geq 0 \\ 0 & \text{otherwise} \end{cases}. \quad (18)$$

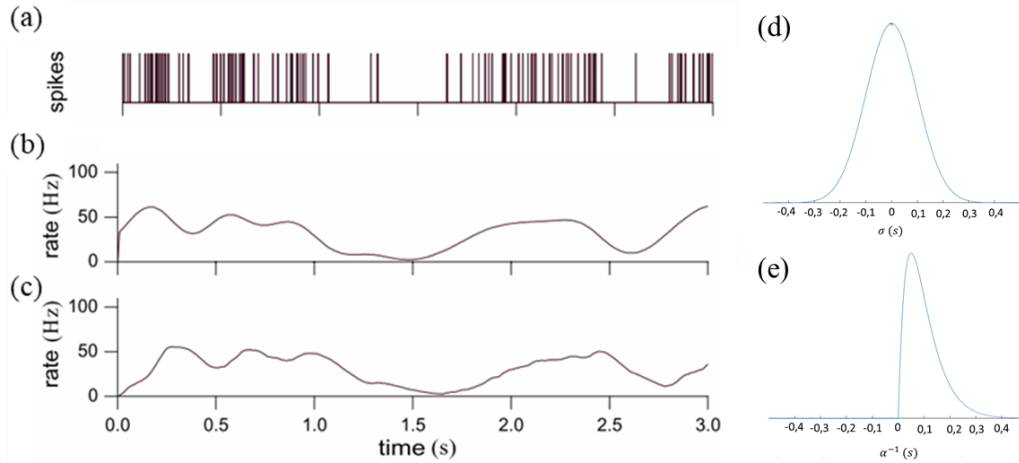


Figure 4.2 - Firing rates estimation through two different methods. (a) Spike train recorded from a monkey cortical neuron. (b) Firing rate approximation using a Gaussian kernel with $\sigma = 0.1$ s. (c) Firing rate estimation using a causal kernel (α -function window) with $1/\alpha = 0.1$ s. Adapted from [25]. (d) Example of a Gaussian kernel curve with $\sigma = 0.1$ s. (e) Example of a causal kernel (α -function) curve with $1/\alpha = 0.1$ s.

The figures 4.2 (b) and (c) show two different firing rates approximations of the spike train recorded from a cortical neuron (figure 4.2(a)). In (b), it was used a Gaussian kernel to compute the firing rate. Looking to a characteristic Gaussian curve (figure 4.2(d)), it follows a normal distribution (mean: $\mu = 0$; standard deviation: $\sigma = 1$). In the figure 4.2(d), we observe its symmetry in relation to a middle center point. This means that when a Gaussian window function slides through the spike train, will be used any spike to the right or left of that point, as long as they are inside the window (under the curve), to estimate the firing rate. Considering that point as the present moment, the Gaussian kernel will use the past and the future spike events in relation to that point, which cannot be applied in a real-time estimation of the firing rate, for instance, using a device to monitor this rate, simply because the future events did not happen yet. In (c), a causal kernel (α -function) was used to estimate the firing rate. The word causal indicates that the output only depends on the present or past inputs, what make these types of filter ideal to be applied in real-time systems. As the figure 4.2(e) demonstrates, half of the kernel is zero which corresponds to the “future” part. This is very useful in this work because, at each iteration of the controller loop, the firing rate could not be estimated including the null part of the vector where the spikes are stored. Consequently, as result of the features of the two filters and once this spike train is complete, I mean, it is not an estimation where the spikes will continue to appear over the time, like what happens in a real-time situation, the Gaussian Kernel will always be one step forward in relation to the firing rate calculated through the causal kernel. This is notorious when comparing the figures 4.2(b) and (c), where the (c) rate tends to peak later in relation to (b) since the Gaussian kernel is always adding events that occur after time t (t -time in which the approximation is being done). While, the α -function only uses the spikes before t to estimate the rate. In addition, its estimations suffer from a delay proportional to α .

4.1.4. Tuning the controller

In this work was used a manual tuning due to the lack of a detailed linear process model to describe the system dynamics, which are usually used by practically all know tuning methods [108], [116]. To manually tune the gains of the controller the total time of simulation was reduced to 5 seconds and the discretization time to 0.1 ms because with the previous settings the model becomes computationally heavier and time-consuming, which are not the desired features for this tuning process where various trials are needed. The setpoint was defined to 30.0 Hz, what means that the controller should adapt the electrode's current to introduce the right current to maintain the simulated neuron firing with a rate of 30 spikes per second. It is also important to remember that the model continues with the neuron's "intrinsic" current that is responsible to make the neuron fire at 10 Hz, value already defined in the subsection 4.1.2.

First, starting with the proportional gain, the integral and derivative gains were set to zero and K_p was increased until obtain an oscillatory response. After that, K_p was reduced to half of that value to obtain a "quarter amplitude decay" type response. Then, K_i was increased in order to stop the oscillation in the firing rate response and try to reduce the steady state error. Lastly, after defined the values for K_p and K_i , K_d was also increased to try to remove the overshoot of the response. To figure out what type of controller fits better in the model, after chosen the value of K_p , we also tried a PD (Proportional and Derivative) approach, i.e., instead of increase K_i , it remained null and we started to increase K_d .

In order to obtain a finer tuning of the parameters, for each gain was selected a range of values around the previously selected values for the gains. For each possible combination between the three gains, it was calculated the area between the response of the controller in relation to the setpoint value, as we can see in the figure 4.3. The triple combination corresponding to the smallest area was selected.

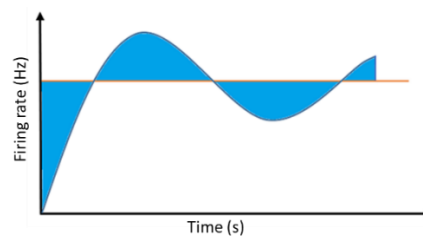


Figure 4.3 - Area between the response curve of the system and the setpoint value (red line).

4.1.5. Validation of the controller

Before validating the response of the controller, it was necessary to validate the way that the firing rate was computed, i.e., verify whether the causal kernel was better than the Gaussian kernel to estimate the firing rate in a "real-time" situation (during the simulation). To find out how the two types of kernels were going to behave during the control cycle loop of

the simulation, we created a vector of zeros and ones with the size of the simulation (5 sec = 50000 steps for $dt = 0.1$ ms), where the ones represent the occurrence of spikes. The ones were randomly distributed along the vector of zeros, about 60 spikes, less in the last 2 seconds (20000 steps). The kernels and their firing rates' approximation will be presented in the Results and Discussion section.

After that, the controller's performance was evaluated in two phases. The first validation process of the developed model consists in testing the model using a neuron that during the simulation time is changing its firing rate. The idea is to observe how the controller reacts to abrupt changes in the values of firing rate, and if its response is capable to recover from these variations bringing the neuron's rate again to the reference value. To do that, it was created a function responsible to change the I_{neuron} over the simulation during fixed periods of time. The values of current correspond to well-defined firing rates, which through the equation 14 were converted in current. The second step to validate the model involves the introduction of noise in the system to perturb the performance of the controller, mainly the derivative part that is more sensitive to noise. Nevertheless, the moving average filter used to remove the abrupt oscillation peaks in the error vector should be sufficient to stabilize the error curve and use it to calculate the derivative error of the system. This noise will be introduced in the model by adding it to I_{neuron} and its biological meaning is related with the called "neuronal noise". The neurons in the neuronal circuits are constantly receiving a large number of synaptic inputs that act as a source of noise, which can disturb the neuronal response. This noise is a combination of excitatory and inhibitory synaptic inputs [118]. The noise was created through the MATLAB function *randn*, which follows a standard normal distribution to distribute random numbers in a vector with the number of steps corresponding to the simulation duration time. In each cycle of the loop, the value of noise corresponding to that iteration is added to the current I , that will be used to compute the membrane potential in the IF-model. Of course, the values of noise were multiplied by a decimal factor to reduce its magnitude. The results will be presented in the Results and Discussion section.

4.2. “Real-time” closed-loop control

The core goal of this dissertation work was the design and implementation of an *in vitro* “real-time” closed-loop control system using the commercial MEA2100-System from MCS. This section describes all the steps performed to reach this goal.

4.2.1. Electrophysiological system overview

The electrophysiological recordings carried out in this work were done using two commercially available *in vitro* systems for extracellular recordings using MEAs. These systems belong to MEA2100-System line from MCS (Reutlingen, Germany) [119]. These devices include two main components: a headstage and an interface board. Currently, there are available 6 different types of headstages: for one 32, 60, 120 or 256-electrodes MEAs per headstage or for two 32-electrodes MEAs or 60-electrodes MEAs per headstage. The headstage corresponds to the part of the system where the MEA is positioned. It is the core element of the system and is responsible for data acquisition, signal amplification and also has an integrated stimulus generator. The acquisition is done through an A/D converter integrated into the headstage and the acquisition parameters such as the sampling rate (until 50 kHz per channel) can be set on the computer using the MCS software. The amplification process occurs before the acquisition and near the signal source to minimize the noise in the signals. The system has a fixed hardware gain of 10 and a resolution of 24 bits [119]. The stimulus generator consists in 3 independent integrated stimulus generator units (2 in the case of the MEA2100-256-System). It enables current or voltage stimulation, monophasic or biphasic pulses, and single pulses or pulse trains. Any MEAs' electrode can be selected for stimulation, enabling a targeted stimulation, and can also record. Stimulus features, electrodes selection or other stimulation configurations are implemented in the MCS software [119]. The interface board is connected to the headstage and receives the signal from it. Also, it contains a DSP. This component is truly important in the present work because enables real-time signal detection, filtering, analysis of the acquired data and, the main tool of this work, the feedback stimulation in real-time. The filtering is done by a second order high and low pass filters integrated into the hardware. By default, the hardware filtering settings were a cut off frequency of 1 Hz to the high pass filter, which aims to prevent the baseline drift of the recorded signals and, the low pass filter had a cut off frequency of 3.3 kHz. These settings can be changed through a software (“MEA2100 Configuration”) to configure the hardware filters bandwidth without any modification in the hardware. More, this interface connects to the computer and has other digital inputs and outputs for synchronization with additional instruments [119]. For more detailed information about the MEA2100-System, the datasheet with the technical specifications can be consulted in [120].

The experiments present in this dissertation were performed with the MEA2100-120-System and MEA2100-256-System, i.e., using 120 and 256-electrodes MEAs chips.

4.2.2. Preparation of MEA for cell culture

In this work were used substrate-integrated planar 120 and 256-electrodes MEAs (MCS) (Reutlingen, Germany) composed of 120 titanium nitride (TiN) recording electrodes and 4 internal reference electrodes in a 12×12 grid [121], and 252 titanium nitride (TiN) recording electrodes and 4 internal reference electrodes in a 16×16 grid, respectively. TiN is a very stable material, giving a long life to MEAs and allow their re-use. Both MEAs have a silicon nitride (SiN) isolator. The tracks and contact pads of the 120-MEAs are made of TiN and in the 256-MEAs, they are made of a transparent indium-tin-oxide (ITO) [122], perfect to see the culture on the microscope, otherwise, the tracks density would not allow it. Each electrode has $30 \mu\text{m}$ in diameter with a center-to-center inter-electrode spacing of 100 or $200 \mu\text{m}$ (depends on the chip used), and an impedance of less than $100 \text{ K}\Omega$ [122].

The MEAs were prepared for cell culture by surface coating with 0.05% of PEI (25kDa, Sigma-Aldrich Co.) overnight at 37°C , followed by four washing steps with sterile water. After completely air-dried, MEAs were subsequently coated with $5 \mu\text{g}/\text{ml}$ laminin isolated from mouse Engelbreth-Holm-Swarm sarcoma (Sigma-Aldrich Co.) at 37°C , for at least 2h before cell seeding.

4.2.3. Cell culture experiments

Experimental procedures involving animals were carried out in accordance with current Portuguese laws on Animal Care (DL 113/2013) and with the European Union Directive (2010/63/EU) on the protection of animals used for experimental and other scientific purposes. The experimental protocol (reference 0421/000/000/2017) was approved by the ethics committee of the Portuguese official authority on animal welfare and experimentation (Direção-Geral de Alimentação e Veterinária). All efforts were made to minimize as possible the number of animals and their suffering.

Unless otherwise stated, all reagents listed below are from Gibco, ThermoFisher Scientific.

Primary embryonic rat cortical neurons were isolated from the prefrontal cortices of Wistar rat embryos (E-18). Embryos cortices were dissected in HEPES-Hanks' Balanced Salt Solution (H-HBSS) and enzymatically digested in $0.5 \text{ mg}/\text{ml}$ trypsin (1:250) in H-HBSS for 15 min at 37°C . Subsequently, tissue fragments were washed once with 10% (v/v) heat-inactivated fetal bovine serum (hiFBS, Biowest) in H-HBSS to inactivate trypsin, and twice with H-HBSS to remove hiFBS from the solution. Tissue fragments were then mechanically dissociated with 5 ml plastic pipette and subsequently with 1 ml pipette tips. Viable cells were counted using the trypan blue (0.4% (w/v), Sigma-Aldrich Co.) exclusion assay to determine the cell density of viable cells. Therefore, the laminin coating solution was removed from the MEAs and 3×10^5 of viable cells were seeded on the coated MEAs. Cells were cultured in Neurobasal medium supplemented with 0.5 mM glutamine, 2% B-27 supplement and 1% penicillin/streptomycin (P/S, 10,000 units ml^{-1} penicillin and $10,000 \mu\text{g} \cdot \text{ml}^{-1}$ streptomycin), and kept in a humidified incubator at 37°C

supplied with 5% CO₂. The experiments were performed using cells with 15 - 35 days *in vitro* (DIV).

4.2.4. MEA2100 setup

After introducing the system's hardware, let's focus on the software. To complete the system is necessary a computer, computationally powerful and with a high memory capacity, where the software package Multi-Channel Suite needs to be installed. This package includes three programs: the Multi-Channel Experimenter where the data is exhibited in real-time and the acquisition setup is set, for instance, apply filters, detect spikes, configure the stimulation settings, etc. Basically, it commands the MEA2100-system and is where the experimental protocol will be defined. The other program is the Multi-Channel Analyzer. As its name says, is a tool to analyze the data recorded from the Multi-Channel Experimenter. The files can be imported to it allowing an offline analysis, for example, to detect spikes or analyze bursts. Finally, the third program is the Multi-Channel DataManager. It allows the conversion of the data files recorded with the Multi-Channel Experimenter in other file extensions permitting us to export the files for analysis with other programs. It is the case of the extension HDF5, which can be used in MATLAB R2017b (The MathWorks, Inc., USA), where the data analysis of the recordings was made.

Despite the use of two different MEA2100-Systems, the setup of the experiments is equal since both use the same software and the graphical user interface is practically equal, except the MEAs layout for obvious reasons and in the case of the MEA2100-256-System, it just has 2 stimulator units instead of 3. Although, it is not relevant because just one stimulator is used during the experiments. The figure 4.4 shows the layout of the recording setup used in the experiments:

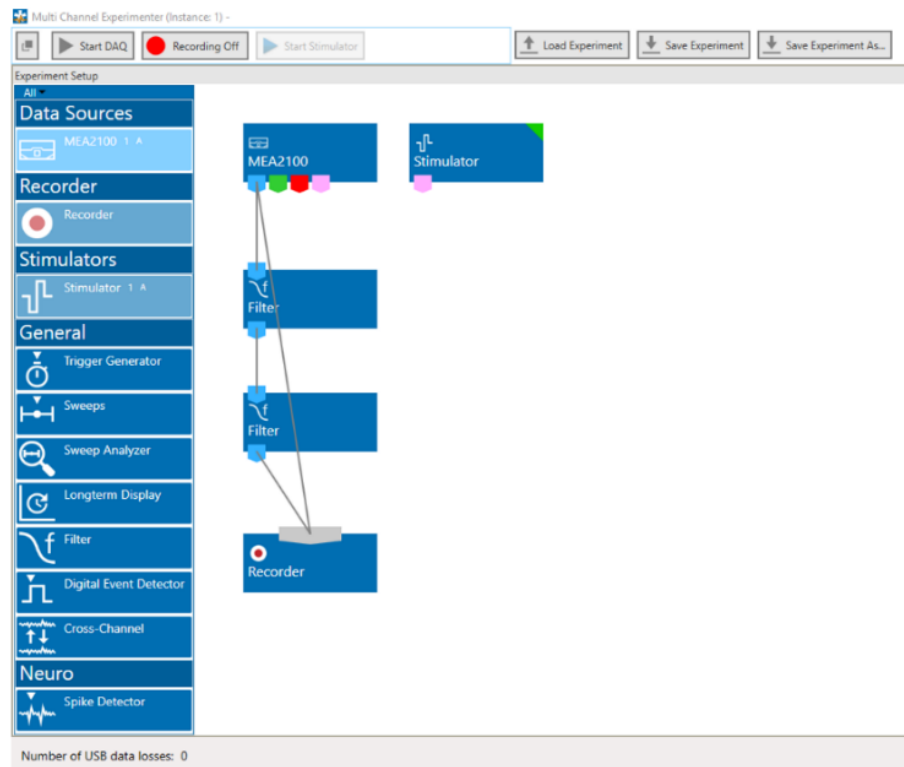


Figure 4.4 - Layout of the recording setup used in the experiments.

The general setup of the experiments was designed in the Multi-Channel Experimenter software. The graphical interface of this program is very user-friendly and to mount the setup we just need to drag-and-drop the boxes in the left side of the panel to the white space and link them as shown in the figure. By double-clicking on the top of any instrument box, it will open a control window tab dedicated to that box. For instance, in the MEA2100 box is where the data acquisition settings are, such as the sample rate, and also has a separator to access the real-time feedback settings.

Both, raw data and filtered data were recorded during the experiments. Note that these are digital filters and do not have any relation with the integrated hardware filters. More, the raw data could be filtered after the experiments using the Multi-Channel DataManager software. The digital filters implemented in the experiments' setup were a second order high-pass Butterworth filter with a cut off frequency of 200 Hz followed by a second-order low-pass Butterworth filter with a cut off frequency of 4000 Hz. Knowing that EAP frequency band is located between the 300 and 3000 Hz [46], the selected bandwidth does not present any restriction to the detection of APs.

With regard to the stimulation settings, they are accessible to the user by double-clicking in the stimulator box and will appear the control interface shown in the figure 4.5.

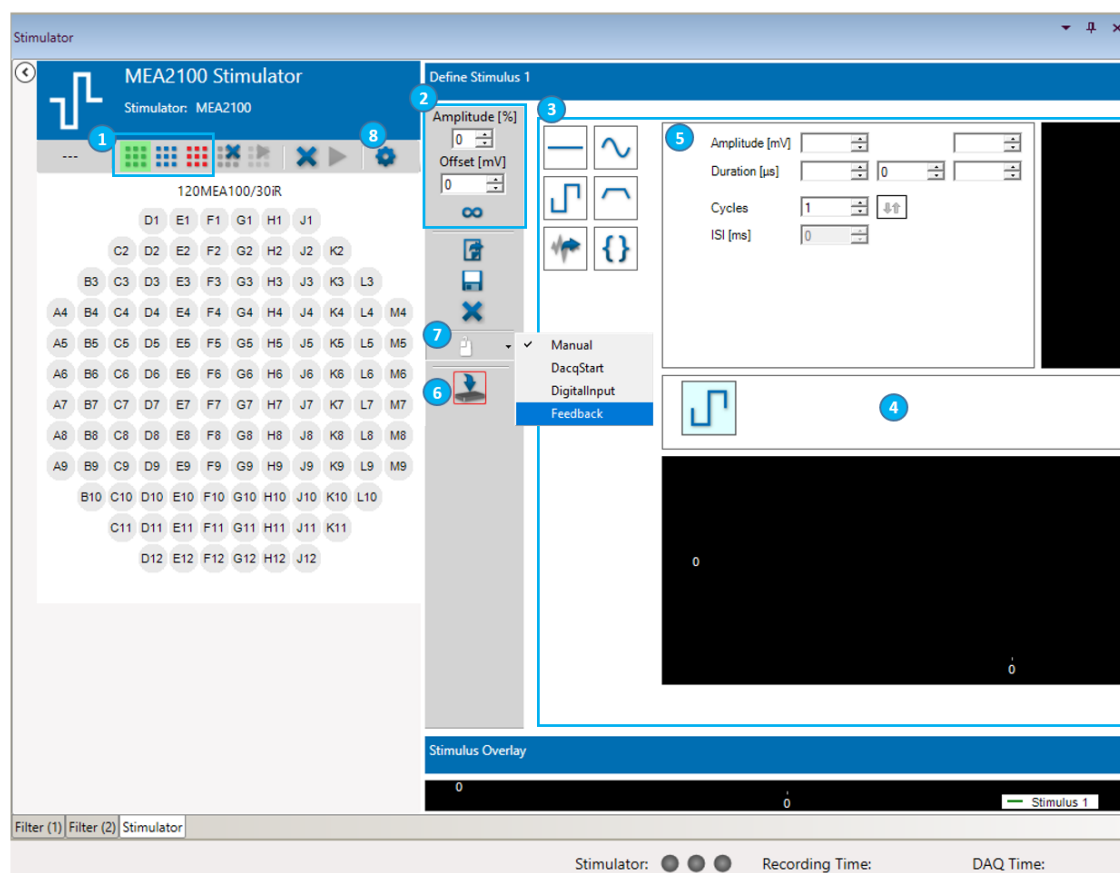


Figure 4.5 - Screen capture of the stimulators settings control window tab.

In this control window, it is possible to select the electrodes used for stimulation. First, we choose the integrated stimulator that we want to use by clicking in one of the stimulators (stimulator 1 - green, stimulator 2 - blue or stimulator 3 - red) in (1) and after, we select the electrodes that will be used to trigger the stimulus. Remember that the stimulators are independent and each one has its own control tab; also, all the three could be used in the same experiment. Also, note that the figure is from the MEA2100-120-System as we can see by the MEAs' layout and by the existence of three stimulators. The stimulation pulse parameters and the stimulus' shape can be defined in (2) and (3). First, by drag-and-drop the boxes of predefined waveforms, below the number (3), to the rectangular space, in (4), it is possible to build the desired type and shape of the stimulus and create stimulation patterns by combining different stimulus [119], [123]. The stimulation parameters of the stimulation pulse can be adjusted in (5). Then, the stimulus is downloaded into the DSP by clicking in (6). For the current work, the manual trigger to stimulation is changed to feedback (7). In addition, there are two important features of the integrated stimulus generator that should be addressed. If the user press in (8), will be opened a small window relative to the stimulus generator settings. These settings include two output options, current or voltage, and two strategies to suppress

stimulation artifacts. The “Blanking” option is referent to the blanking circuit integrated into the stimulator. This circuit, during the stimulation, disconnects the electrodes from the amplifiers avoiding stimulus artifacts on the recording electrodes. In addition, it prevents the saturation of the amplifiers, which means the reduction of the recovery time. The blanking period is about 600 μs (currently) before and after the stimulus [119], [123]. During this time, a flat line is displayed in the recordings. The “Dedicated Stimulation Electrodes” option, as it says, the electrodes are just for stimulation. This option further prevents the presence of stimulation artifacts that are not completely eliminated, by the blanking circuit, on the surrounding recording electrodes. Sometimes, the blanking action of switching the stimulation electrode between the stimulator (during the stimulation pulse) and the amplifier (to record again), provokes switching artifacts which are not related with the given stimulation. Thus, if the stimulation electrodes are fully dedicated to stimulation, these kind of artifacts are practically removed from the surrounding recording electrodes once the stimulation electrodes are always connected to the stimulator. However, recordings using the stimulation electrodes are not possible due to the elevated noise levels in those electrodes [119], [123].

After defined the stimulation parameters and downloaded the stimulus to the DSP, it is time to configure the “real-time” feedback settings.

The “real-time” feedback is the most important feature of the MEA2100-system according to the main goal of this dissertation, which is the control of the global activity level on the culture (population mean level), using feedback stimulation in response to the variation of neuronal populations firing rate. In a typical situation using similar systems, the recordings are made, the signals are analyzed and afterward, the stimulation is manually triggered. However, this procedure introduces an enormous delay in the control process. The MEA2100-System integrated “real-time” feedback enables a more automated control capable to reduce the response delay to less than 1 ms. This is only possible because the interface board contains a DSP, which connects with the amplifiers and the stimulators and works independently. I.e., as mentioned before, the DSP has access to the recorded data in real-time. It can perform real-time filtering, data analysis such as spike detection and, if a certain condition is satisfied, it can trigger a feedback stimulation according to the stimulation parameters defined in the software [119].

As said before, the feedback settings can be accessed in the MEA2100 box when we open that separator. These settings are displayed in the figure 4.6, and some important features will be described.

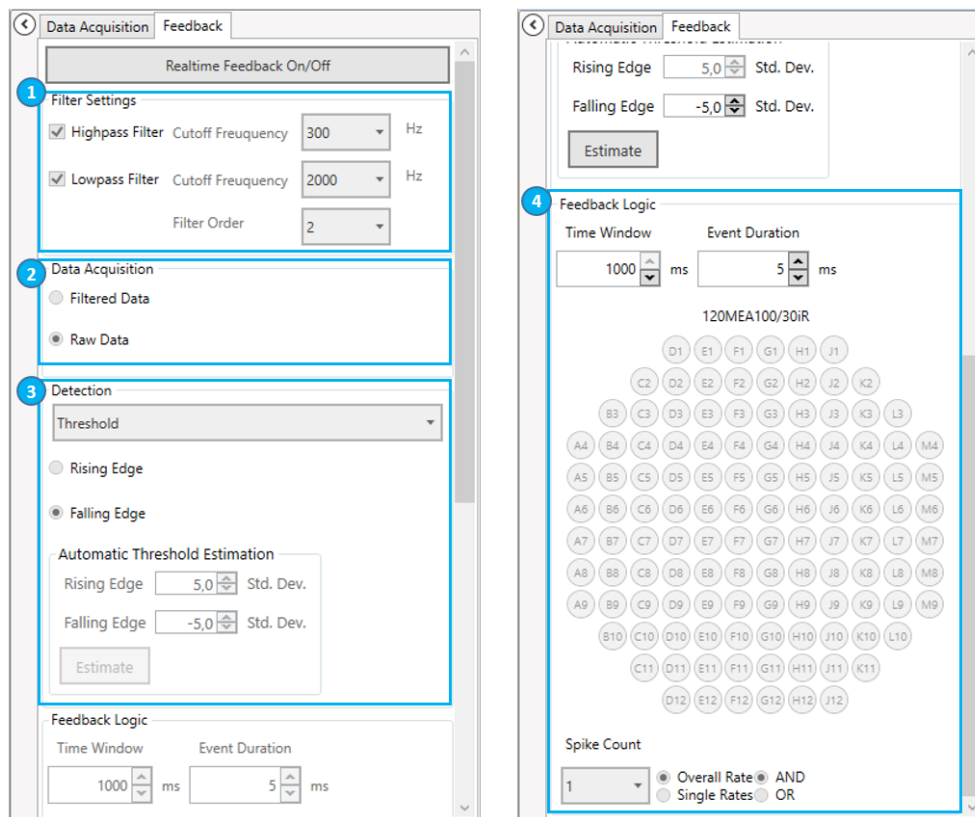


Figure 4.6 - Screen capture of the feedback control window. (1) Block to define the filters; (2) Block to choose whether the acquisition data is filtered or not; (3) Block to define the detection parameters; (4) Block to define the feedback logic.

The selected options and the values presented in the figure 4.6 do not characterize the feedback settings used in the experiments of this work thus, let's focus on the boxes delimited in blue and their functions. In (1), the DSP filtering settings can be set; it is not required to use both filters and, actually, it is not even necessary to fill in this field since in (2), as you can see, the “real-time” feedback can also be performed using raw data. However, in the closed-loop experiments performed in this work, it was used a second order high pass filter with a cut off frequency of 300 Hz to remove the slow wave fluctuations from the recorded signal and the baseline characteristic oscillations resulting from burst activity. This filter is extremely important due to the fact that in (3) when defining an amplitude threshold to detect spikes, it is calculated individually for each channel based on a user-defined factor times the standard deviation of the noise [119], [123]. Thus, if the baseline level of the recorded signal moves up or down mainly due to burst activity, some spikes could not be counted or even some could be wrongly counted. The detection threshold can be either positive or negative, but not both at the same time. The system also allows a manual threshold [119], [123]. In the experiments carried out in this work, the threshold level to detect spikes was negative since all recordings presented mainly falling spikes, and the threshold value was set to five times the standard deviation of the noise.

The most complex part of the real-time feedback is the “Feedback logic” in (4), which defines the condition to trigger feedback stimulation. This logic is made in the DSP. Regarding

the condition defined by the user, the logical state could be TRUE or FALSE, which confirms if the feedback stimulation is triggered or not. First, we will start by the different fields available to fill or select. Starting with the electrodes layout, there could be selected one or more electrodes, which will be used by the DSP to compute the feedback logic and verify if the feedback conditions are or not satisfied. The “Time Window”, in milliseconds, defines the duration time of a moving window that will be used to count the spike rate in the signals. I.e., imagine that for a “Time Window” of 1000 ms we want a “Spike Count” of 10 spikes, this means a firing rate of 10 Hz. This condition just is fulfilled when detected 10 spikes in a second. This window is limited to 1000 ms [123]. The “Event Duration”, in milliseconds, is the time after the detection of a spike that determines that the detection condition is considered satisfied. At that moment the logical state referent to the detection condition becomes TRUE until the end of the event duration. If there is a minimum number of TRUEs equal to the “Spike Count” within the “Time Window”, the feedback stimulation is triggered [123]. When using the option “Single Rates” and more than one electrode, it is necessary to combine the logical states of the selected electrodes with the options “AND” or “OR”, however, this is more complicated to explain and it was not used in our experiments but, for more information you can consult the Multi-Channel Experimenter manual [123]. For “Overall Rate” option or just one electrode selected, the options “AND” or “OR” are not applicable and is exactly what happens in this work experiments. More, the “Event Duration” used in our experiments was 1 ms, which is the approximate duration of APs observed in the recordings.

Finally, to ensure that the experiments have the lowest possible impact on cell viability and to record over longer periods of time, an external temperature controller (TC02) was connected to the MEA2100-System headstage which has a heating element right beneath the MEA. Controlled by the TC02, the heating element enables constant temperature conditions for the cells cultured on the MEAs. The temperature was set to 37°C to mimic the biological conditions. The figure below shows the MEA2100-System setup used in our experiments, including the external temperature controller and shows the schematic model of the “real-time” feedback process.

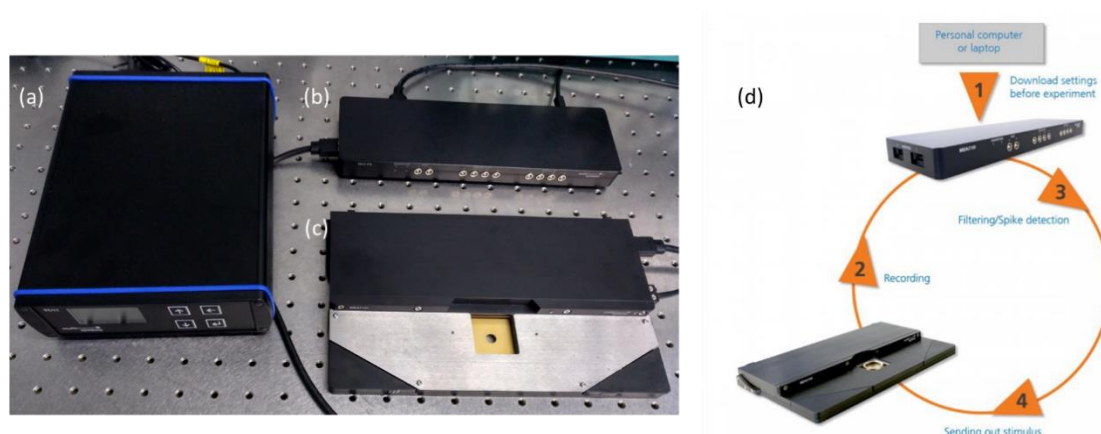


Figure 4.7 - Setup of the MEA2100-System and “real-time” feedback scheme. (a-c) setup of the MEA2100-System available in our lab. (a) external temperature controller (TC02), (b) MCS Interface Board, (c) MEA2100-headstage to record data from one 120MEA chip. (d) Schematic representation of the “real-time” feedback process integrated into MEA2100-120-System. First, we define the condition for the feedback and download it to the interface board (1). During recording (2), the DSP filters the data and detects spikes (3). When the event is detected, the integrated stimulus generator generates the stimulus pulse (4) [124].

4.2.5. Stimuli Validation protocol

First of all, it is important to emphasize that, although these type of MEA-Systems are commercially available and have been used in electrophysiological experiments for a considerable time already (2 decades), the integrated real-time feedback is a feature recently added to these systems. Currently, I can affirm that there are only a few research groups that have this electrophysiological system (MEA2100-System), being the research group where this dissertation work was elaborated, one of them. For these reasons, some difficulties were encountered when defined the stimulation protocols since, so far, there is little available literature about experiments using the real-time feedback of 2100MEA-System. However, we are here to create and not to copy so, the stimulation protocols were created based on published stimulation studies in dissociated cultures on MEAs.

The electrical stimulation in neuronal networks or in single neuronal cells has been used since electrophysiology early days due to the electrical nature of these cells. Therefore, the stimulation effects are well documented in the literature. For instance, Gertz et al. [125] proposed a stimulation protocol to train networks to respond to patterns of stimulation applied to the culture over the MEAs electrodes. Still, the majority of well-defined stimulation protocols to modulate neuronal activity include a set of steps with precise durations of stimulation and specific stimuli frequencies. Those stimulation periods are long, which does not enable their use in our experiments once we are trying to implement a real-time feedback control. This means that this control should have the fastest impact on the modulation of the neuronal activity, i.e., the response to the triggered stimulus should have an “immediate” effect in the activity. Because, unlike what happened in those mentioned protocols where the stimulation is constant during the experiments, in our experiments, the stimulation is given

when the DSP pre-defined condition is satisfied. We cannot ensure that stimulation always occurs at a given frequency throughout the experiment.

The MEA2100-System, as mentioned before, is capable of current or voltage stimulation modes. Although, there are some aspects that should be considered before choosing the type of stimulation. According to the manufacturer's recommendations, the stimuli must be negative monophasic voltage pulses or biphasic voltage pulses (negative phase first) to ensure that the electrode is discharged at the end of the pulse [122]. When applied current pulses, they should be biphasic to actively discharge the electrodes at the end of the stimulation. The easy way is to set the same signal amplitude and duration for each phase. Alternatively, ensure that the product of amplitude and time for each phase is matching, avoiding electrode's damages by electrolysis [122]. For these reasons, voltage pulses were used since with current pulses we would be limited only to biphasic pulses.

Even for the voltage pulses is necessary to pay attention to a few recommendations. Starting with the amplitude of the pulses, this one should be smaller than 1 V for neuronal applications. Bigger values are harmful to the cells and, can also damage the electrodes by electrolysis [122], [126]. The width stimuli pulses are usually between 100 μs and 500 μs [122]. More, the amplitude and duration of the stimulus must be balanced, i.e., a big amplitude should be combined with a small pulse duration.

Wagenaar et al. did a great study of electrical stimulation through MEAs in dissociated cortical neurons cultures [126]. They tested a range of rectangular pulses (current and voltage) with different shapes, amplitudes and durations to study their efficacy. In addition, they determined the parameters' ranges that improve stimulus efficacy without provoking damages in the cells or electrodes. In their studies, for biphasic voltage pulses, they used a range of amplitudes between 100 to 1000 mV with durations of 100 to 800 μs per phase. And, for monophasic voltage pulses, they tested pulses with amplitudes also ranging from 100 to 1000 mV but with a fixed duration of 400 μs . Each pulse was fired 50 times with 1 second between trials [126]. They reported that positive-than-negative biphasic voltage pulses were the most effective tested pulse to evoke activity. By activity, they want to mean APs. Biphasic negative-than-positive voltage pulses were also capable to elicit APs if sufficiently strong [126]. Monophasic negative voltage pulses could also evoke activity but were less effective than the biphasic pulses. The positive monophasic pulses were not capable to evoke many responses. At a fixed duration, activity increased with the increase of the amplitude but, for the same amplitude, the activity do not depend strongly on the duration [126]. More, with similar features, the voltage pulses were more effective than the current pulses [126]. Despite their results shown to be reliable and consistent, they represent an increase in the difficulty of our work since they demonstrated that these vast ranges of tested pulses were always capable to increase the activity of the neuronal cells, with the exception of the positive monophasic pulses. However, these ones could not be used in our system for equipment safety reasons as said before. In this point of work, we were in an impasse since to be able to modulate the neuronal activity we need stimuli to evoke activity but also to inhibit it. Another important

aspect is the manner how the “real-time” feedback of our system works. Since it triggers a stimulus when a certain number of spikes are present within a pre-defined time window, if we increase the activity of the neuronal population by applying a stimulus, that condition tend to be more and more times satisfied which leads to a cascade of triggered stimuli and it is not what we define as control. Thus, for our experiments, we needed stimuli capable to inhibit cells activity. Despite Wagenaar et al. results were a bit demotivating at the beginning of our experiments, they gave us confidence about the type of parameters we could use to define the shape, amplitude, and duration of the stimulation pulses. For these reasons, many experiments were performed (> 750 GB of data) and many of them were discarded. Thus, for obvious reasons, not all experiments are here.

Our initial trials to set up a viable stimulation protocol led us to 4 different types of stimulus in order to try to understand if any of them was able to reduce the firing rate of the primary cortical neuronal cells cultured on the MEAs in an effective and reliable way. The four types of voltage stimulation pulses are displayed in the table 4.1. For the recordings were used different cultures with 15 to 35 DIV. This type of cultures start to firing after approximately 4 DIV and shortly after that time, synchronizes its activity across all culture, resulting mainly in burst activity [103]. Just to clarify, the interval of DIVs used in this work does not mean that during that interval of time were performed recordings every day. It is just an interval to give the indication of how long the neurons were in culture when the recordings were made, and also to ensure that the cells do not die after the stimulation trials. More, the recordings were only performed when the activity on the electrodes seemed to be good. I.e., the electrode displayed an observable spiking activity over the time with a good SNR and, did not fired only when there were global bursts all over the network. Only in that way, with a relatively “constant” firing rate, it was possible to evaluate the stimulation effect. Lastly, small things as the medium change could silence the neuronal activity and the “adaption” phase of the cells to the chips could result in longer periods of weak activity and after a certain time they could “wake-up”. The signals were sampled at 10 kHz (this value is the minimum recommended value to use). This rate is enough to record spikes however, their shape is not very realistic. Although, it is not important in our experiments since we do not do spike sorting or use a detection algorithm based on shape.

Table 4.1 - Summary of voltage stimulation pulses tested.

Pulse shape	Peak-to-peak amplitudes (mV)	Pulse widths (μ s) (per phase)
1- Biphasic negative-than-positive	600	200
2 - Biphasic negative-than-positive	400	500
3 - Monophasic negative	550	180
4 - Monophasic negative	800	280

The complete protocol consisted of the following steps:

- (1) Basal activity: after inserting the chip in the MEA2100-system headstage, wait about 10 minutes to give time to the culture to adapt to its move from the incubator to the system. Next, the spontaneous activity of one electrode is recorded 3 times during 200 s. The interval time between recordings should be as small as possible;
- (2) Feedback stimulation: the activity of the previous electrode during the “real-time” feedback stimulation is recorded 3 times during 200 s. The stimulation is given by 4 electrodes adjacent to the recording electrode distributed in a diamond pattern with the recording electrode in the middle; The feedback “Spike Count” parameter is chosen according to the user’s estimation of the firing rate and should be a value capable to trigger a stimulation pulse. I.e, if the approximated firing rate is 5 Hz, we cannot choose a “Spike Count” of 10 for a “Time Window” of 1000 ms, for instance.
- (3) Basal activity post-stimulation: wait 5 minutes to let the cells recover from the stimulation. Repeat the step (1) and record spontaneous activity.

4.2.6. Neuronal network experiments protocol

According to the results of the stimuli validation, the most reliable and effective stimulus was chosen to use in neuronal network experiments control. The protocol is the same with some differences with regard to the number of electrodes. In the previous section, it was used only one recording electrode and 4 stimulation electrodes. Despite the goal was the control of all neuronal population cultured over the MEAs, it was difficult to have all the recording electrodes with a considerable activity. Sometimes the cells are silent in some parts of the electrodes’ array, in other cases, by looking the MEAs chips on the microscope, we realized that there were no cells on the top of some electrodes. In those cases, instead of using all the electrodes, we selected a block of electrodes with activity to perform the experiments. Within that block, we chose strategically the stimulation electrodes to ensure that any recording electrode has one adjacent stimulation electrode. For the recordings were used different cultures with DIVs between 15 to 25.

4.2.7. Data analysis code

The analysis of the results of the experiment was made in a MATLAB environment. To do that, it was necessary to install the MCS MATLAB toolbox “McsMatlabDataTools”. This toolbox allows us to import HDF5 files. Thus, first we need to convert the recording files created by the MCS Experimenter software using the MCS DataManager software. The spikes were detected just by a threshold crossing. The detection threshold V_D was calculated using the median M_s and the standard deviation σ_s of the recorded signal:

$$V_D = M_s \pm 5 \times \sigma_s. \quad (19)$$

Ideally, the median and the standard deviation should be calculated with the baseline noise level [5], [22]. However, in our recordings, we did not have the occurrence of a large frequency of large spikes that could be wrongly inflated the M_s and σ_s values, being the baseline noise dominant in the signals. More, the data analysis uses the recorded filtered signals where the signal fluctuations have been removed. The detection threshold is always calculated individually for each recording electrode.

Although the spikes recorded were mostly falling spikes, both, falling and rising spikes were detected through our spikes' detector algorithm since we realized that even a small number of rising spikes could make the difference posteriorly when the firing rate was calculated once the recordings just have 200 s. Despite it is a small interval of time to calculate the firing rate for each recording, very long experiments are not good for cell viability and after some trials, we considered that this time reached a balance between the approximation of the firing rate with enough confidence without conditioning the viability of the cells. Remember that the total time of the experiment is approximately 45 min.

After detecting the spikes, we faced another problem. The positive and negative threshold could detect the same spike two times when the spikes have a biphasic shape. The spikes are mainly monophasic negative or positive but in fact, there are biphasic spikes. To ensure that the algorithm did not detect two times the same spike, it uses a window function that runs the vector where the spikes are stored and, any time that more than one spike appears within that window, it guarantees that the first spike is maintained in its position and the other is removed. According to the sampling rate of the recordings, it creates a window with a size corresponding to 1 ms. The reason behind this interval of time it is because we noticed that the difference between the positive and negative shape peaks of biphasic spikes, in general, was less than 1 ms (with some margin of error). We cannot ensure that all spikes comply with this condition because it was impossible to see each one individually but in general, this interval should work perfectly from what we saw.

The next step was to create a mask with the size of the duration of the stimulus pulse. This is because we noticed that even with our experiments being performed with the options "Blanking" and "Dedicated Stimulation Electrodes" selected, all the artifacts sometimes were not removed and could lead us to a wrong firing rate estimation. The system's manufacturer itself says that these options remove the majority of the stimulation artifacts; however, some may be present in the recordings. Therefore, to create the mask we use one stimulation electrode. As a result of the "Blanking" option, during the stimulation period, a "flat line" is exhibited in the signal. Thus, by using a local standard deviation filter twice in the signal and find the places in which the filtered signal is small than 0.1, we could identify the flat lines periods on the stimulation electrode that may be a stimulus. After, to remove the false-negatives, we applied a moving average filter to remove the "fast" flat lines that were not stimulus. Lastly, the zeros and ones mask was created, the zeros correspond to the locations

of the stimuli and when the mask is multiplied by the recorded signals, it is possible to remove completely the stimulation artifacts. This mask is only applied to the feedback recordings.

Finally, the firing rate, in Hz, is calculated by dividing the number of detected spikes by the duration time of the recordings, in seconds.

Chapter 5

Results and Discussion

5.1. Integrate and Fire model with a PID controller

This part of the work consisted in the development of an *in silico* PID controller capable to modulate the neuronal activity of a simulated neuron through the injection of current. The results will be now presented and discussed.

5.1.1. Integrate-and-Fire model implementation

As described in the section 4.1, before introducing the controller component we first needed to implement the *in silico* neuronal model (IF-model). The figure 5.1 (a) shows the result of the simulation using the IF-model implemented in MATLAB. Simulation parameters are described in the legend of the figure. It is possible to notice that neither the form of the curves or their amplitudes can be compared to the characteristic curves of APs. However, it is quite simple to know when an AP occurs. Also, the curve's behavior was previously explained in the figure 2.2 (b). The figure 5.1 (b) gives the firing rate calculated through a Gaussian kernel with a σ of 100.0 milliseconds. In this situation, the Gaussian kernel fits perfectly because the firing rate is only calculated at the end of the simulation. In this part of the work there is no external current injected into the model, the only source of current is the membrane's current intrinsic to the neuron, that was manipulated using the equation 14 to make the simulated neuron fires at 10 Hz what is exactly what gives the kernel's approximation, increasing the confidence in the temporal resolution chosen. Looking at the figure 5.1 (c), it is clear that there are 10 spikes in a window of 1 second.

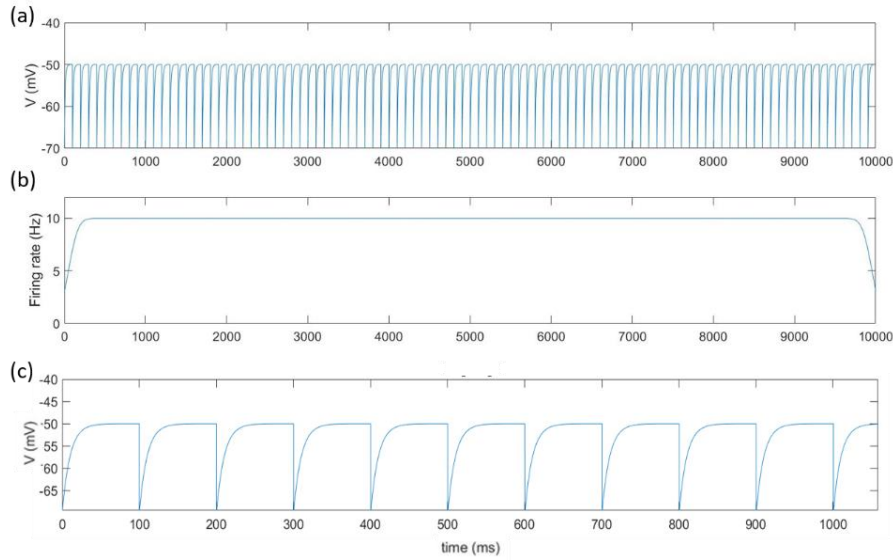


Figure 5.1 - Simulation of a neuron using the IF-model. The parameters used in the simulation were $E_L = V_{reset} = -70 \text{ mV}$, $V_{th} = -50 \text{ mV}$, $\tau_m = 10 \text{ ms}$, $R_m = 20 \text{ M}\Omega$ and $dt = 0.01 \text{ ms}$. The firing rate was defined as 10 Hz. (a) Simulation of spiking behavior during 10000 ms. (b) Firing rate calculated through a Gaussian kernel with a σ of 100 ms. (c) Simulation of spiking behavior during a time window of 1000 ms.

5.1.2. Controller's implementation - “real-time” firing rate calculation

To obtain good control results, the controller needs to have a good approximation of the firing rate at each iteration of the cycle loop, since the control error (e) is the difference between the process variable (firing rate calculated at each iteration) and the setpoint value ($e = r - y$). The validation of the two types of kernels (Gaussian and causal α -function kernel) was performed according to what is described in the Materials and Methods section. The figure 5.2 shows the both kernels created and how they run the vector where the spikes will be stored during the simulation.

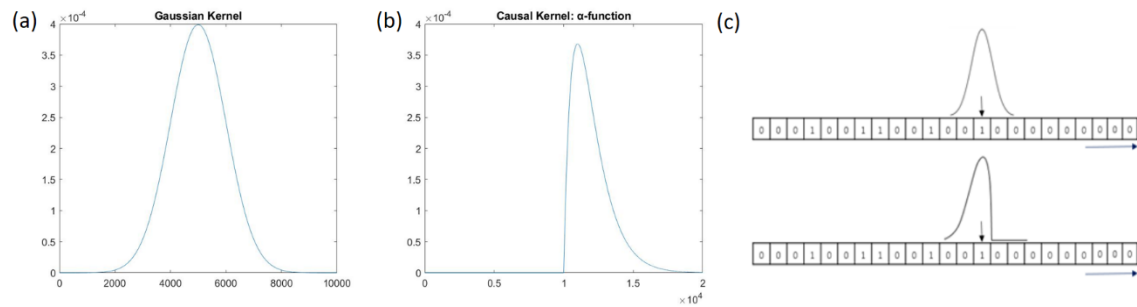


Figure 5.2 - Gaussian and α -function causal kernels curves. (a) Gaussian kernel with a temporal resolution of $\sigma = 100 \text{ ms}$. (b) Causal kernel in the form of an α -function with $\alpha = 0.01$ and a temporal resolution given by $1/\alpha = 100 \text{ ms}$. Both kernels were created in MATLAB. (c) Example of how the kernels run the vector of spikes in a real-time estimation. The blue arrow indicates the direction in which the kernel's window is “sliding” the vector and the black arrow indicates the actual iteration of the control loop. This image is not in scale.

The results from the simulations to validate and compare both the kernels are presented in the figure 5.3. In green is represented a spike train of 60 spikes generated and distributed

randomly until reach the 3 seconds of simulation. The black line shows the firing rate estimation of the Gaussian kernel and the purple line the approximation of the α -function kernel. Both kernels have the same temporal resolution, however, their estimations are considerably different. The reasons why this occur were already explained in this work but with the drawings of the kernels filters, in the figure 5.2, is easier to understand. In general, both are capable to make good estimations despite the Gaussian kernel is always a step forward in relation to the α -function kernel and the continuous transitions are softer. This is due to the smooth nature of the Gaussian curve; when we look at the figure 5.2 (c), it can “predict” what is going to happen after the time t (where the arrow is positioned), integrating the spikes after that time according to its probability density function contributing to a smooth passage. Unlike, the causal kernel has its negative part null and the peak of its curve is located practically above time t , as observed in the figure 5.2(c). Thus, according to its probability density function, if during a transition in the spikes vector from t to $t+1$ corresponds to $0 \rightarrow 1$, the weight of this passage has much more impact in the integration what makes those oscillations in the firing rate estimation. In addition, there is a delay proportional to α . These behaviors are in accordance with the figure 4.2.

Now, let's interpret what happens at $t = 3\text{ s}$ of simulation. Imagine that in a real-time control situation, the current position of the cycle loop is in the iteration that corresponds to 3 seconds. At this point, the black line is in decline since it uses the zeros from the vector after time t to estimate the firing rate. This could influence the error (e) and lead the controller to inject a wrong current in the system. On the other hand, the α -function kernel is more sensitive to the changes in the firing rate as we can see from the blue line, the integration of new spikes that occur over the simulation is noticeable by the small peaks in the curve. Yet, the last peak only occurs after time t due to the delay proportional to α . However, it is still a more realistic approach to a firing rate real-time estimation.

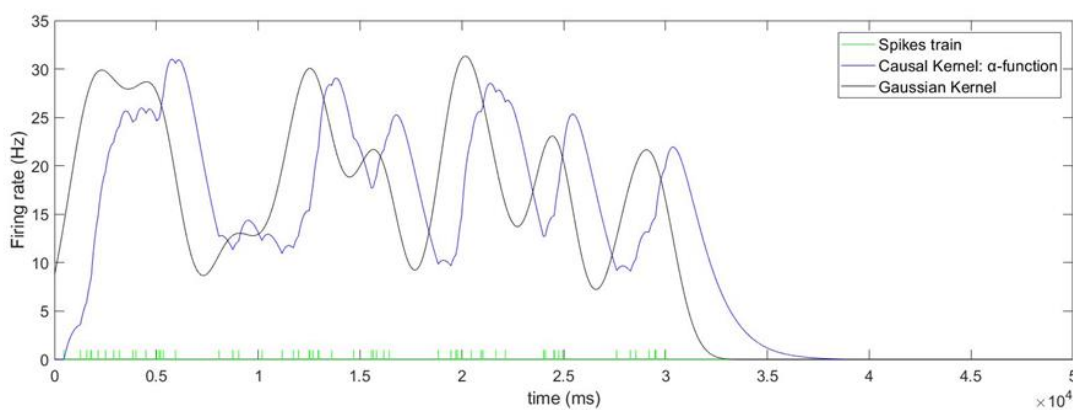


Figure 5.3 - Validation and comparison between both kernels. In green is represented a spike train of 60 spikes generated and distributed randomly until reach the 3 seconds of simulation. The black line shows the firing rate estimation of the Gaussian Kernel and the purple line the approximation of the α -function kernel. Both kernels have the same temporal resolution (100 ms) however, their estimations are considerably different.

5.1.3. PID controller tuning

As addressed before in the section Materials and Methods, the tuning of the gains of the controller was done manually. Starting with the proportional gain (K_p), the results are presented in the figure 5.4.

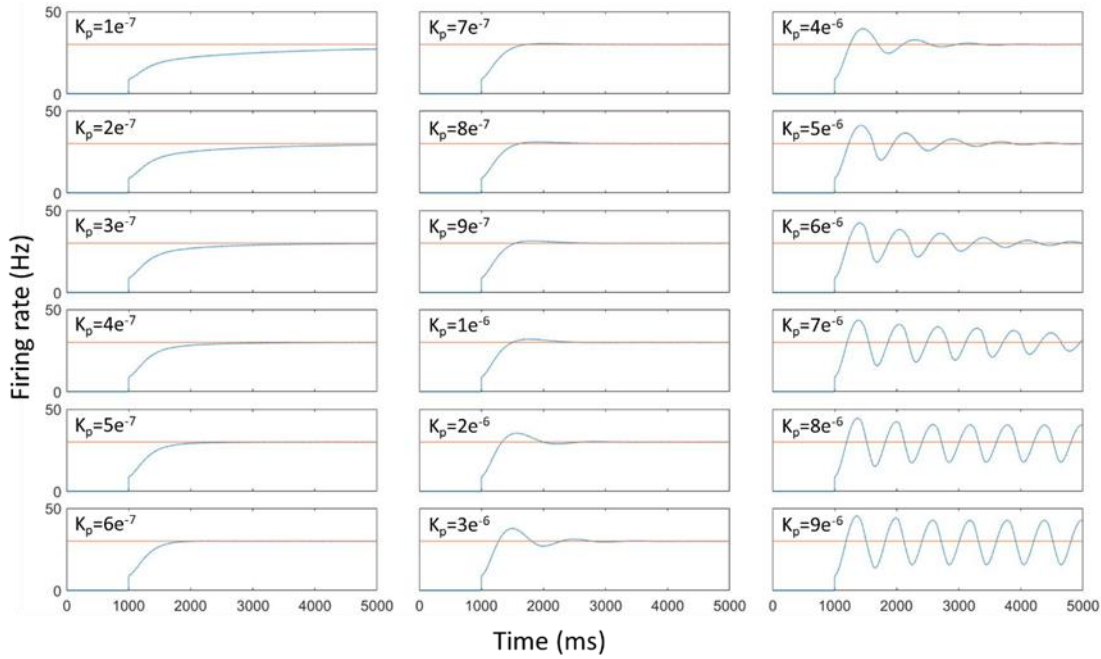


Figure 5.4 - Proportional gain (K_p) tuning of the PID controller. The figure shows the different curve responses (blue line) for different values of K_p . The integral and derivative gains, K_i and K_d , were set to 0. The setpoint value is 30 Hz (red line) and the simulation period was 5000 ms with $dt = 0.1$ ms.

These results were obtained during a simulation period of 5 seconds. Just note that during the first second there is no calculation of the firing rate because this period of time corresponds to the window size of the kernel ($10\sigma = 1000$ steps), and the control only starts after that time. For small values of K_p , in this case, until $K_p = 4 \times 10^{-7}$, the system cannot reach the setpoint value (30 Hz). If the simulation time was larger it eventually would reach that value and stay stable. However, a control system should be fast and one of the aspects that contributes to the velocity of the response is the proportional gain. Thus, increasing K_p becomes the response faster but also increases the overshoot. This is demonstrated in the figure 5.4 with $K_p = 1 \times 10^{-6}$. The first time that the firing rate equals the reference value of 30 Hz occurs at $t = 1.5$ s, what gives a response time of 0.5 s. In this situation, there is a small overshoot. If we continue to increase K_p , the response starts to oscillate at $K_p = 3 \times 10^{-6}$. From this value, the system becomes unstable as shown in the figure above. The value of K_p at which the response started to oscillate was reduced to half ($K_p = 1.5 \times 10^{-6}$) to obtain a “quarter amplitude decay” type response. Then, K_i was increased within a range of values. The results are presented in the figure 5.5.

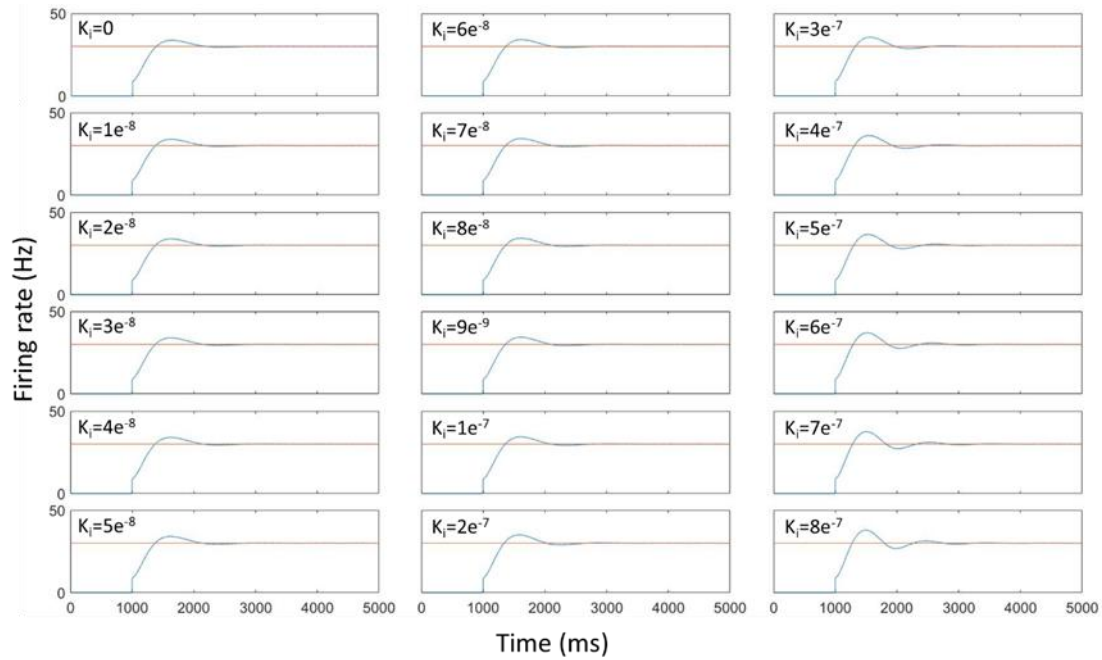


Figure 5.5 - Integral gain (K_i) tuning of the PID controller. The figure shows the different curve responses (blue line) for different values of K_i . The proportional gain, K_p , was set to 1.5×10^{-6} and the derivative gain, K_d , was set to 0. The setpoint value is 30 Hz (red line) and the simulation period was 5000 ms with $dt = 0.1$ ms.

After introduced the integral component of the controller there were no significant improvements in the response. The higher the value of K_i , higher is the overshoot, the response starts to oscillate and eventually becomes unstable. The main goal of the integral component is to remove the steady state error. However, in this case, it is not evident.

After, the derivative component was introduced. The value of K_p remained the same and the value of K_i chosen was $K_i = 1 \times 10^{-7}$. The introduction of this component had as a goal the reduction of the overshoot of the response, anticipating its behavior in advance. Again, we tried a range of values and the results can be observed in the figure 5.7. In addition, we noticed that, there was an oscillation resultant from the delay proportional to α during the firing rate approximation. The figure 5.6 shows this oscillatory behavior of the firing rate curve, as well as in the error curve. These fast changes in the error curve (figure 5.6(e)) could have a significant effect in the derivative component since the rate of change of the error could vary a lot. I.e., it can give the indication to the system that the error is increasing very fast due to a positive accentuated slope but, actually, it is only because of these oscillation peaks of the error curve. To avoid this kind of deregulated action of the derivative part of the controller, it was applied a moving average filter to the error curve that aims to smooth the oscillations, I mean, remove the peaks of the curve and ensure that the tendency of error's variation is maintained but without peaks. We used two different windows to compute this and they are presented in the figure 5.6(f).

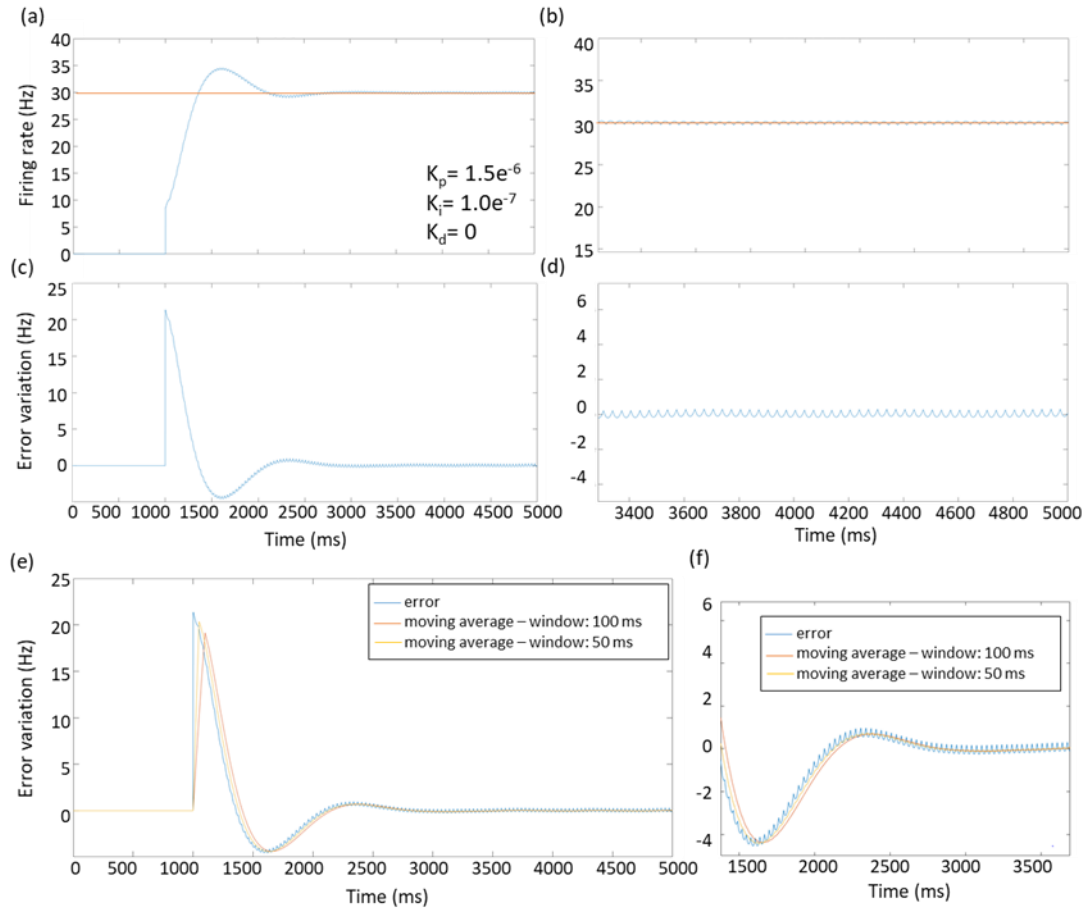


Figure 5.6 - Action of the moving average filter in the control error e of the PID controller. (a) Firing rate curve response (blue line) using the following gains: $K_p = 1.5 \times 10^{-6}$; $K_i = 1.0 \times 10^{-7}$ and $K_d = 0$. (b) Steady-state error of the response. (c) Error variation during the simulation time. (d) Oscillatory behavior of the error. (e, f) Two different size moving average filters applied to the error variation curve.

The results of the figure 5.7 show that until a certain value ($K_d = 3 \times 10^{-4}$), the derivative action of the controller is capable to reduce the overshoot, however, does not eliminate it completely. The settling time is also reduced.

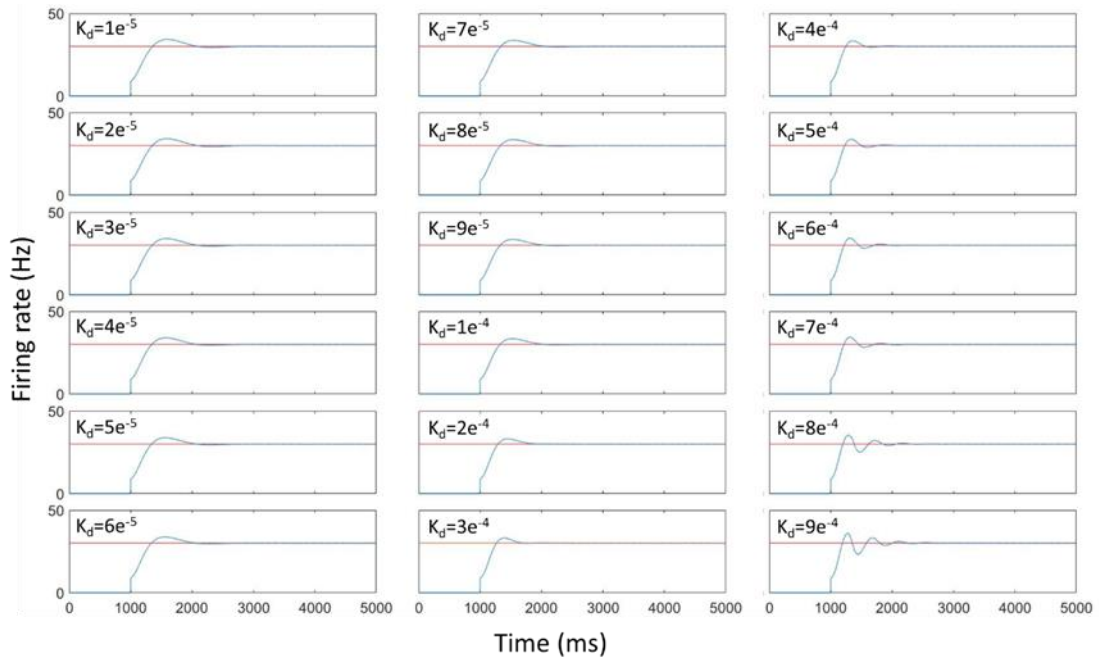


Figure 5.7 - Derivative gain (K_d) tuning of the PID controller. The figure shows the different curve responses (blue line) for different values of K_d . The parameters used were $K_p = 1.5 \times 10^{-6}$ and $K_i = 1.0 \times 10^{-7}$, and the variation of K_d is described in each graph. The setpoint value is 30 Hz and the simulation time was 5 s.

In order to try to remove the overshoot of the response, and verify if a PD controller has a better performance instead of a PI controller or a PID controller, K_i was set to zero since the integral action contributes to increase the overshoot and K_d was increased, remaining $K_p = 1.5 \times 10^{-6}$. The results are accessible in the figure 5.8.

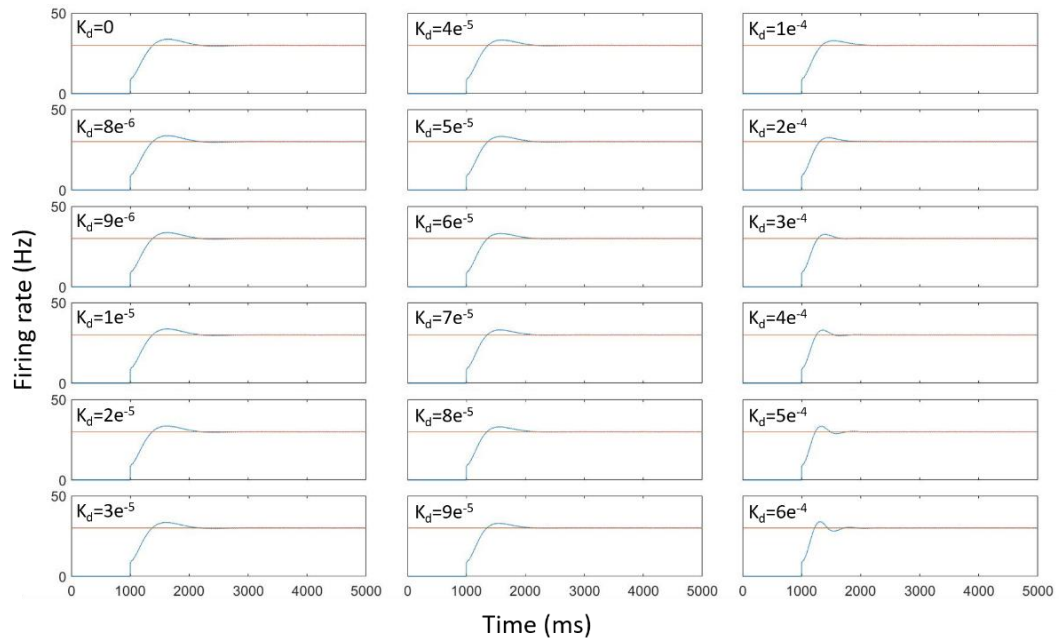


Figure 5.8 -Panel with the different graphs of firing rate (Hz) obtained with derivative gain (K_d) tuning of the PD controller. The figure shows the different curve responses (blue line) for different values of K_d . The parameters used were $K_p = 1.5 \times 10^{-6}$ and $K_i = 0$, and the variation of K_d is described in each graph. The setpoint value is 30 Hz and the simulation period was 5 s.

The results indicate that there is a decrease in the overshoot of the response. Still, it was not completely removed. In general, a rapid response has always associated an overshoot. To eliminate it, K_p and/or K_i should be smaller because these two gains are the main responsible to the occurrence of an overshoot. If we look to the figure 5.4, with only a proportional controller, we realize that, for a $K_p = 6 \times 10^{-7}$ there is no overshoot and the desired firing rate is reached in less than 1 s. However, as said before, the parameters and the type of controller should be chosen according to the needs projected to the developed system that will be controlled. I.e., if the response velocity is extremely important, K_p should be set to obtain that kind of response; if the error elimination is more critical to the system, K_i is the parameter to adjust; if is necessary to reduce the overshoot and make the system more stable, we need to play with K_d . We also noticed that, for a derivative gain bigger than 4×10^{-4} , the response started to oscillate.

Based on the results of the figure 5.7, in our point of view, the values of the parameters that provide the best response are: $K_p = 1.5 \times 10^{-6}$, $K_i = 1.0 \times 10^{-7}$ and $K_d = 2.5 \times 10^{-4}$. The figure 5.9, provides a detailed vision of what happen to the main components of the model during the simulation. This includes the spiking behavior of the simulated neuron, the variation of the firing rate as well as the change in the current injected in the neuron, error variation, rate of change of the error and neuron's membrane current.

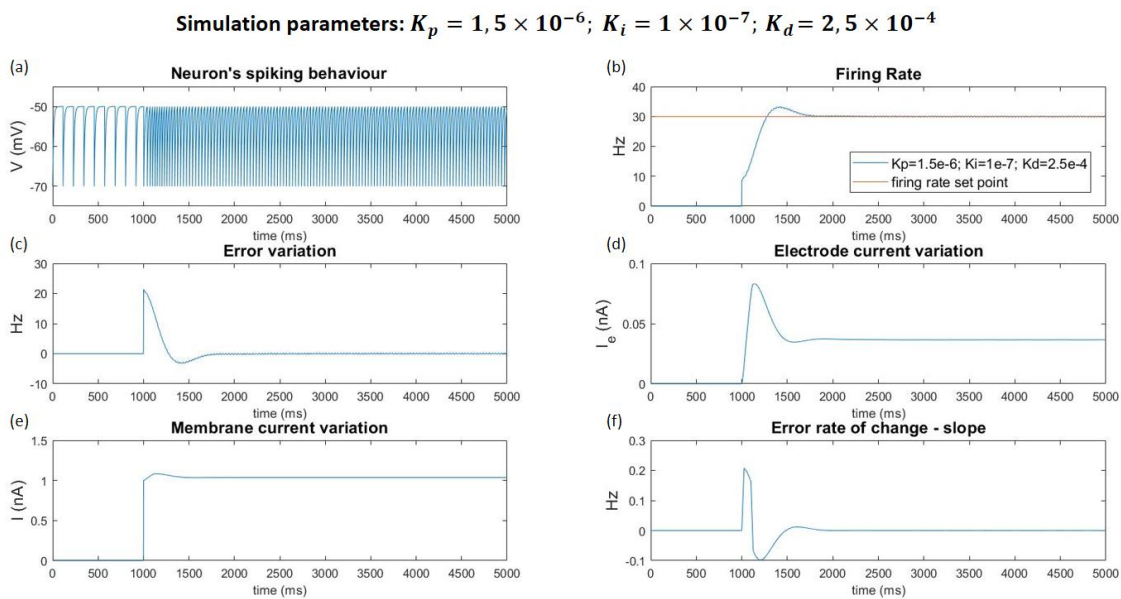


Figure 5.9 - Summary of the results obtained with the model during the simulation. (a) Adaptation of the spiking behavior of the simulated neuron during the simulation. (b) Firing rate curve response (blue line) in relation to the setpoint value - 30 Hz (red line). (c) Error variation curve during the simulation. (d) Adjustment of the electrode's injected current during the simulation. (e) Neuron's membrane current variation over time. (f) Rate of change of the error during the simulation.

The figure above contains a set of subplots to evaluate the performance and the feasibility of the developed control system. In (a), it is possible to see the adaptation of the neuron to the injected current. Again, note that until 1 sec of simulation there is no control and the firing

rate is 10 Hz, as explained at the beginning of this section. After this time, the period between spikes is shorter, a consequence of the injected current to achieve the desired firing rate. In (c), the error is varying throughout the simulation. Here we need to be careful when analyzing this curve because, since the controller is off during the first second, the error is not being calculated in that period. Thus, that's why the curve is at zero. From there, the error is approximately 20 Hz (remember that the neuron is initially firing at 10 Hz and the setpoint value is 30 Hz). The error should be exactly 20 Hz, although, due to the delay of the α -function kernel used to estimate the firing rate, this value is slightly different. Next, when the controller starts operating, the error begins to decrease and, before stabilizing around zero, we can see the error due to the response's overshoot. In (d) is shown the variation of the electrode's current to compensate the error. (e) shows the change in the membrane current over the simulation time. This current is the sum between neuron's intrinsic current and the current injected by the electrode. In (f) is presented the rate of change of the error; the derivative component of the controller is estimated through this curve after filtered, as demonstrated before. Once again, in these 3 last graphs, the tracing before $t = 1$ s does not have significant meaning, it just marks the time during which the controller is turned off.

The evolution of our tuning process can be observed in the figure 5.10. There, the impact of introducing each one of the controller's components is noticeable.

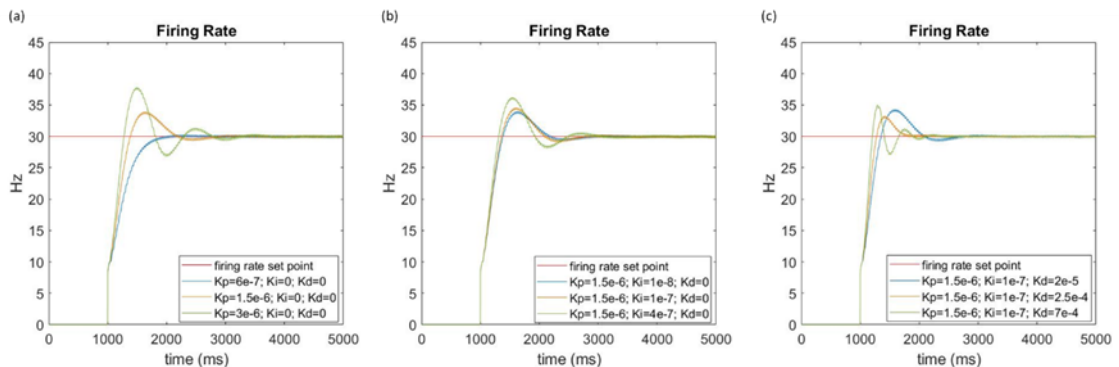


Figure 5.10 - Summary of the tuning process evolution. (a) Action of the proportional component (K_i and K_d were set to 0). (b) Action of the integral component (K_p is constant and K_d is 0). (c) Action of the derivative component (K_p and K_i are constant).

The other strategy used to tune the gains (K_p , K_i and K_d), as mentioned before in the section 4.1, consisted in the evaluation of the area between the setpoint line and the firing rate curve response. This aims to verify which parameters fit a better curve response in relation to the setpoint, to produce the minimum area between them. Based on the results of the previous simulations presented here, a set of values for the gains were selected, 15 values for each one of the gains what results in 3375 combinations. The values used are in the table 5.1.

Table 5.1 - Gains and respective values used in area tuning process.

Gains		Values													
K_p $\times 10^{-7}$	5.0	5.5	6.0	6.5	7.0	7.5	8.0	8.5	9.0	9.5	10.0	15.0	20.0	25.0	30.0
K_i $\times 10^{-8}$	0	1.0	2.0	3.0	4.0	5.0	6.0	7.0	8.0	9.0	10.0	20.0	30.0	40.0	50.0
K_d $\times 10^{-5}$	0	2.0	3.0	4.0	5.0	6.0	7.0	8.0	9.0	10.0	20.0	30.0	40.0	50.0	60.0

The results of the tuning simulations using the values of the table 5.1 demonstrated that the values of the gains which create a response that better fits the setpoint value are $K_p = 5.0 \times 10^{-7}$, $K_i = 1.0 \times 10^{-8}$ and $K_d = 0$. I.e., these values correspond to the small area between the response curve and the setpoint line, as demonstrated in the figure 4.3. The simulation using these parameters is shown in the figure 5.11.

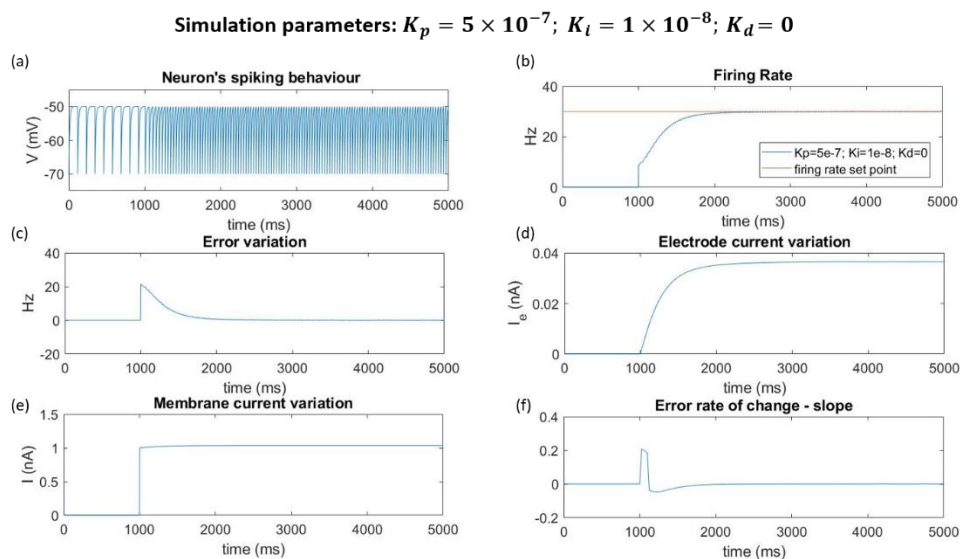


Figure 5.11 - Summary of the results obtained with the model using the parameters obtained using the area tuning process. (a) Adaptation of the spiking behavior of the simulated neuron during the simulation. (b) Firing rate curve response (blue line) in relation to the setpoint value - 30 Hz (red line). (c) Error variation curve during the simulation. (d) Adjustment of the electrode's injected current during the simulation. (e) Neuron's membrane current variation over time. (f) Rate of change of the error during the simulation.

Despite these parameters produce a response that is the closest to the setpoint line (in red), the velocity of the response is not satisfactory. If we look to the first time that the response reaches the reference value, it took more than 1 s to reach that value. In this case, it is our preference to have a faster response, even with a little overshoot since we are talking about events that occur in the millisecond time scale. Therefore, for these reasons the parameters chosen through the manual tuning were selected to continue the validation process of the control system.

The next step of this work was to test if the control system was capable to respond quickly to sudden changes in the firing rate and adapt its response to keep the spiking rate as close as possible to the desired value. During a simulation time of 28 s, it was changed the natural current of the neuron to obtain different firings rates. Each firing rate has a duration of 4 s. Thus, in the total, the firing rate changes 7 times during the simulation period and the firing rate values, in Hz, and, in the order that they appear are the following ones: 45 → 20 → 10 → 40 → 50 → 70 → 25. The results of the simulation are in the figure 5.12.

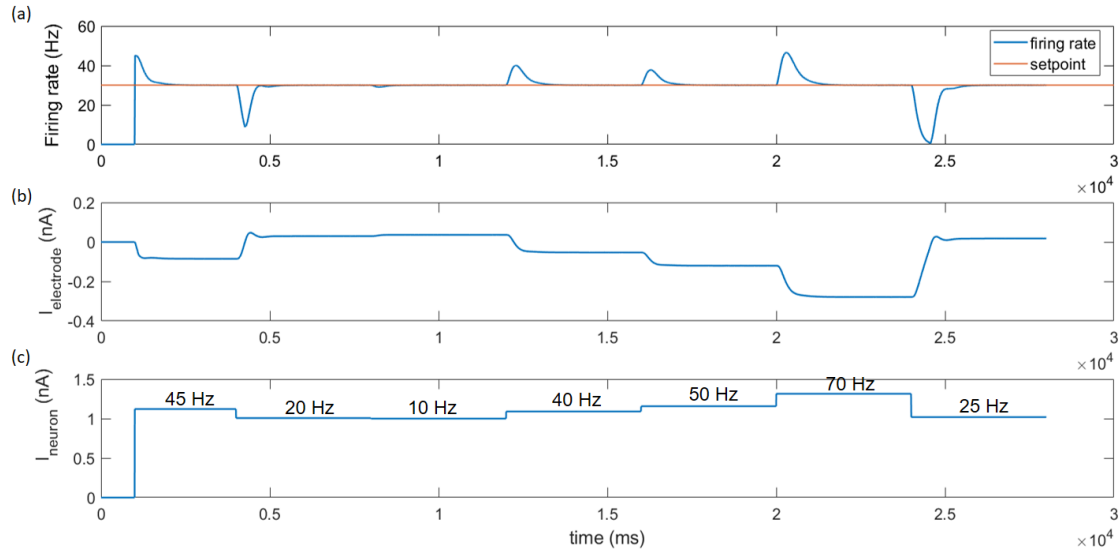


Figure 5.12 - PID controller response to abrupt changes in the firing rate. (a) Firing rate curve response during the simulation. (b) Electrode's current adjustment. (c) Variation in the neuron's intrinsic current to produce well-defined firing rates "steps" on the simulated neuron.

The results show that, despite the abrupt changes in the firing rate of the neuron, the controller is capable to modulate its activity and return the rate to the reference value (30 Hz). Starting with (c), this graph displays the current necessary to the neuron to fire at those values of firing rate (above the curve) over the simulation. We manipulated those values of current. The variation of the electrode's current is demonstrated in (b). This current is manipulated by the controller and is injected into the model to cancel the changes in the firing rate. We see that if the value of the firing rate is greater than the reference value, the current's signal of the electrode is negative and vice-versa. If we look to the response of the system (a), it is clear that the controller is working well since there is a big tendency of the controller to push the firing rate to the setpoint value. The peaks of the curve represent the time where the steps of firing rate are changed, according to (c). As mentioned before, all controllers need a certain time to stabilize its respond (the settling time); of course, it depends on how big is the error. In this case, despite the controller is quick to respond, it could suffer from a delay or an advance when the firing rate is changed (steps of rates in (c)). The first time the control reacts to the firing rate of 45 Hz is in $t > 1$ s (once again, note that the control loop just starts in $t > 1$ s). If we look to the value of the peak in that instant, the value is 45 Hz, exactly what should be. However, if we look to the second transition of the current to 20 Hz, the peak goes

below this value because, in our code, the calculation of the electrode's current necessary to bring the firing rate back to the reference value is only calculated in the final of the loop. I.e., in the next iteration, despite the adjustment of the current is correct for the time at it was calculated, the controller “does not know” that we decided to abruptly change the firing rate in the next iteration. Thus, if the current that enters in the IF-model is the result of $I = I_{neuron} + I_{electrode}$, until that transition, the current of the electrode is negative. And, when summed to the current of the neuron calculated to fire at 20 Hz, it will decrease that value and I is not enough to make the neuron firing at 20 Hz, as it is possible to observe in (a). Hence, in this case, the system will take more time to restore the firing rate to the reference value. However, it could happen the opposite, which is the case of what happens in the transition to 70 Hz since the controller has been contradicting the 50 Hz rate and that negative current ends up to increase the velocity of the response once the peak of that transition does not reach the 70 Hz.

The results referent to the second validation step can be consulted in the figure 5.13. This validation consisted of the introduction of noise in the developed model, to mimic the neuronal noise in biological neuronal circuits. This “synaptic” noise was added to I and the simulation was performed for a duration time of 10 s.

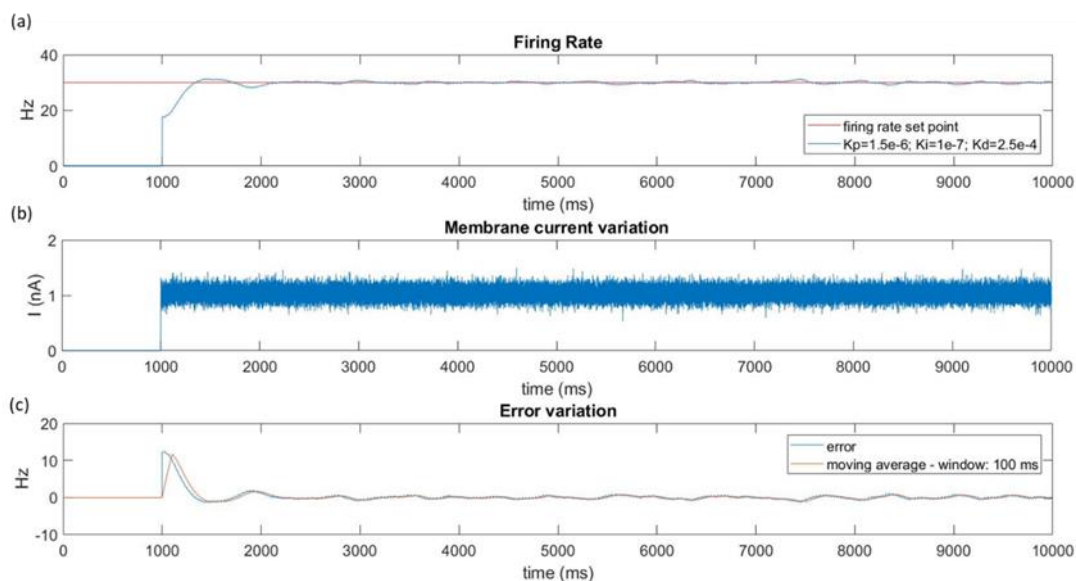


Figure 5.13 - Results of the PID controller response to noise introduction in the simulated neuronal model. (a) Firing rate curve response during the simulation (blue line) in relation to the setpoint (red line). (b) Membrane's current variation with normally distributed random noise (c) Error variation during the simulation (blue line) and corrective action of the moving average filter (red line).

These results demonstrate that even with the presence of disturbances in the system, the controller presents a satisfactory response considering the fact that it is still capable to maintain the firing rate values around the reference value as we can see in (a). It is also necessary to know that unlike the previous validation step with the abrupt changes in the neuron's firing rate, where sufficient time was given to the controller to correct those abrupt changes, that does not happen in this situation. Here, in every iteration of the loop, the

controller is subjected to a new scenario, different from the last iteration. In addition, as shown in (c), the action of the moving average filter applied to the error of the system is fundamental to the performance of the controller by removing those small peak oscillations that could bring additional errors and interferences to the control process. The figure 5.13(b) shows the variation of the membrane current. These values of current are the result of $I_{neuron} + I_{noise} + I_{electrode}$. The noise levels in this simulation vary between -0.5 to 0.5 nA which are significant values considering the sensitivity of the model since a value of $I = 1.000045$ nA corresponds to a firing rate of 10 Hz, as previous used and demonstrated in this work.

Finally, according to Miranda-Domínguez et al. in [107], a good closed-loop performance of the controller implies the correction of the error rapidly, the closed-loop system must be stable and there is on average no error [107]. We think that our results agree with these assumptions.

5.2. “Real-time” closed-loop control

This experimental part of the work consisted in a first validation of four different stimuli to verify what stimulus was more effective and, the second part involves the use of the selected stimulus in neuronal networks control studies.

5.2.1. Stimuli validation experiments

The figure 5.14 (a) shows a real-time recording using the MEA2100-120-System and the figures 5.14 (b) and (c) show microscope images of cultured primary cortical neuron cells over the microelectrodes of a 120MEA chip with a center-to-center inter-electrode spacing of 100 and 200 μm , respectively.

The table 5.2 presents a summary of the performed experiments. In this table can be found specific information of each experiment such as the type of MEAs chips, the electrodes used to record and to stimulate, the type of stimulus applied, the “Spike Count” defined in the feedback control settings and what was the aim of the experiment.

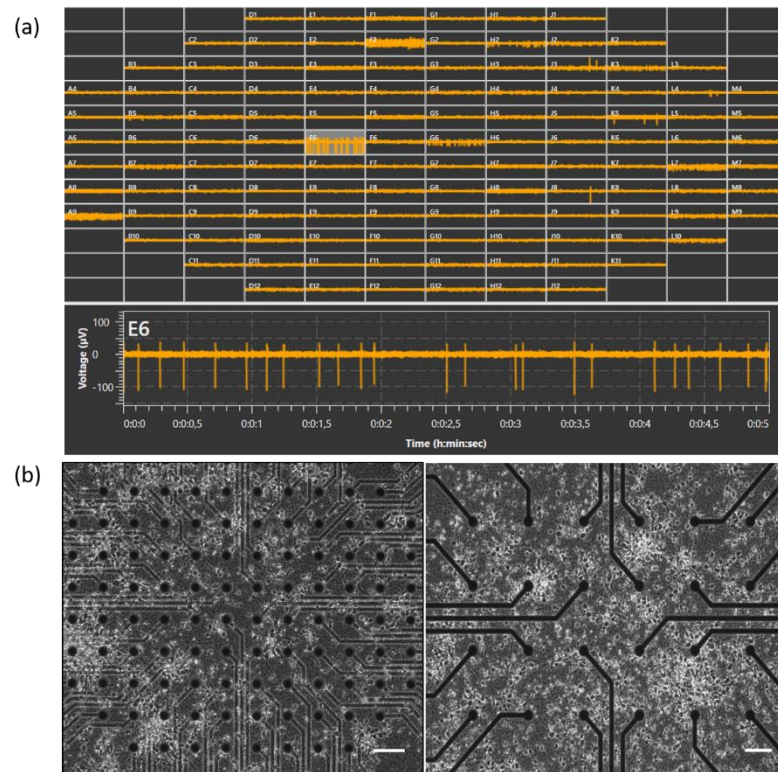


Figure 5.14 - Example of a real-time recording using the MEA2100-120-System. (a) Screen capture of the data acquisition window (on top); recording in a specific electrode (E6) showing spiking activity (on bottom). (b, c) Microscope images of the cultured primary cortical neuron cells over the microelectrode array of a 120MEA chip with a center-to-center inter-electrode spacing of 100 and 200 µm, respectively. (b) Scale bars 100 µm.

Table 5.2 - Summary of the experiments features.

Trial	MEAs chip	Recording electrode(s)	Stimulation electrodes	Stimulus pulse	Spike Count	Goal
1	120MEA	B5	B4, A5, B6, C5	1 *	3	Stimulus validation
2	120MEA	H2	H1, G2, H3, J2	2 *	5	Stimulus validation
3	120MEA	H6	H5, G6, H7, J6	3 *	4	Stimulus validation
4	120MEA	K10	K9, J10, K11, L10	4 *	3	Stimulus validation
5	120MEA	E6	E5, D6, E7, F6	1 *	3	Stimulus validation
6	120MEA	H2	H1, G2, H3, J2	2 *	5	Stimulus validation
7	120MEA	B7	B6, A7, B8, C7	3 *	5	Stimulus validation
8	120MEA	K5	K4, J5, K6, L5	4 *	5	Stimulus validation
9	120MEA	B5	B4, A5, B6, C5	1 **	3	Stimulus validation
10	120MEA	H2	H1, G2, H3, J2	2 **	4	Stimulus validation
11	120MEA	L4	L3, K4, L5, M4	3 **	3	Stimulus validation
12	120MEA	K10	K9, J10, K11, L10	4 **	3	Stimulus validation
13	120MEA	E6	E5, D6, E7, F6	1 **	5	Stimulus validation
14	120MEA	H2	H1, G2, H3, J2	2 **	5	Stimulus validation
15	120MEA	L7	L6, K7, L8, M7	3 **	3	Stimulus validation
16	120MEA	H6	H5, G6, H7, J6	4 **	4	Stimulus validation

17	256MEA	A2 ... L2 A13 ... L13	A3, D3, G3, K3 A6, D6, G6, K6 A9, D9, G9, K9 A12, D12, G12, K12	1 **	11	Network control
18	256MEA	A7 ... F7 A12 ... F12	B8, B11 E8, E11	1 **	10	Network control
19	256MEA	A7 ... F7 A12 ... F12	B8, B11 E8, E11	1 **	10	Network control
20	256MEA	A7 ... F7 A12 ... F12	B8, B11 E8, E11	1 **	8	Network control
21	256MEA	K9 ... K14 P9 ... P14	L10, L13 O10, O13	1 **	9	Network control
22	256MEA	A7 ... F7 A12 ... F12	B8, B11 E8, E11	1 **	7	Network control
23	120MEA	D2	D1, C2, D3, E2	1 ***	8	Stimulus validation
24	120MEA	D2	D1, C2, D3, E2	1 ***	10	Stimulus validation
25	256MEA	K9 ... K14 P9 ... P14	L10, L13 O10, O13	1 ***	8	Network control

* Stimulus with an initial stationary phase of 50 ms and amplitude 0 mV

** Stimulus without an initial stationary phase

*** Recordings with normalized baseline noise level conditions

Before discussing the results, it is necessary to explain the asterisks (*) in front of each stimulus number. This explanation will be given throughout the text. In the case of one (*), this means that the pulse has an initial stationary phase with 50 ms of duration and 0 mV of amplitude. The reasons to use this stationary phase to precede the stimulus were: first, we needed a way to easily identify the stimulus when we were looking to the recordings. We could look to the signals from the stimulation electrodes and see the flat line that corresponds to the triggered stimulation instant. In addition, we could see in the recording an artifact. Despite this visual identification, our main concern was to ensure that the stimulus was really well identified in our MATLAB code to create the mask to remove stimuli from the recordings. As the sampling rate used was 10 kHz, and the stimulus pulse duration is just a few hundreds of microseconds, the stimuli detection could not be successful. The last reason was to avoid applying a stimulus during an AP, although, this would not happen since the “real-time” feedback, in reality, has a delay of 1 ms as previously mentioned. The experiments with this type of stimuli were performed in an early phase of the work, when we were exploring the 2100MEA-System “real-time” feedback. The results of the experiments performed with this type of stimuli are displayed in the figure 5.15 (experiments 1 - 8). Following the protocol, in each experiment, 3 assays were used to estimate the mean firing rate of the primary cortical neuronal cells in three different conditions: (1) spontaneous activity (basal activity), (2) “real-time” feedback stimulation and (3) post-feedback spontaneous activity. These preliminary results indicated that the stimuli 1 (biphasic negative-then-positive with a pulse duration of 200 μ s per phase and an amplitude peak-to-peak of 600 mV) could be capable of inhibiting the spiking activity of the neuronal cells cultured on the top of the electrodes. In the figure 5.15 (a) the firing rate was reduced in spite of the initial basal activity being already quite small. In (b) we see an abrupt reduction in the firing rate during the “real-time” feedback. From a considerable rate on average around 3 Hz, the rate suffers a reduction of more than 50 %. The other results did not satisfy our goal, which was to find an inhibitory stimulus.

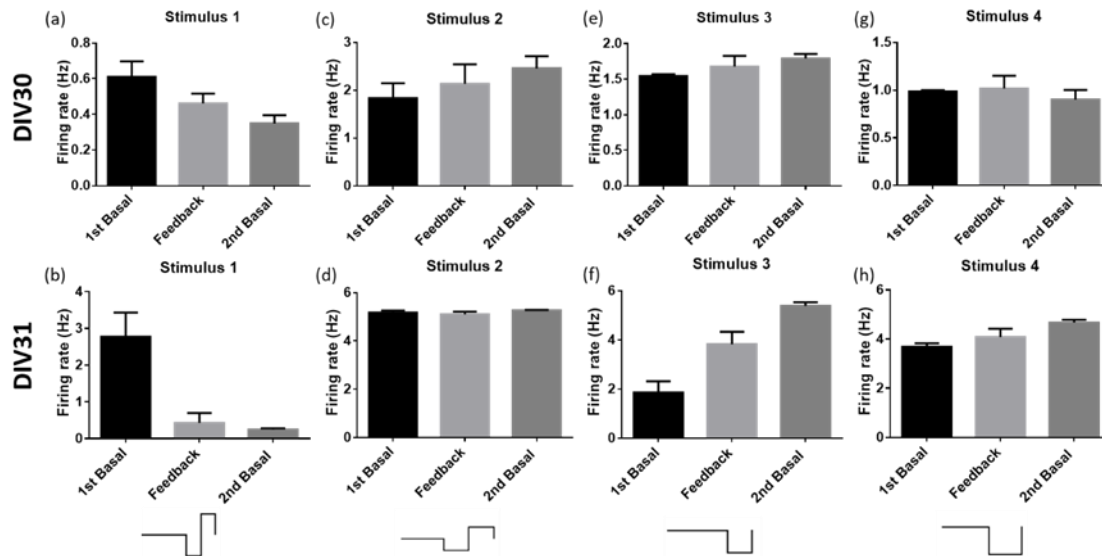


Figure 5.15 - Activity mean levels and respective standard deviations of the experiments (1 - 8) to validate the stimuli (with a stationary phase of 50 ms). (a,b) Biphasic negative-then-positive pulse with a width of $200\ \mu\text{s}$ and $300\ \text{mV}$ per phase. (c,d) Biphasic negative-then-positive pulse with a width of $500\ \mu\text{s}$ and $200\ \text{mV}$ per phase. (e,f) Monophasic negative pulse with a width of $180\ \mu\text{s}$ and $550\ \text{mV}$. (g,h) Monophasic negative pulse with a width of $280\ \mu\text{s}$ and $800\ \text{mV}$. (a, c, e, g) Cells at 30DIV. (b, d, f, h) Cells at 31DIV.

Even though we consider that the stationary phase of the stimuli was not a sufficient justification for obtaining such a large discrepancy in the results of the stimulus 1 compared to the other tested stimuli, the truth is that the occurrence of bursts within those 50 ms windows could, in fact, make the difference since the recordings are only about 200 s. To be sure that it is not the cause of such discrepancies, we followed the same protocol but this time using the same stimuli without the stationary phase. Due to the blanking time before and after the stimulus, they are easily identified by our code to create the mask. These stimuli are marked in the table 5.2 by two asterisks (**). The results of those experiments (9 - 16) can be consulted in the figure 5.16. Once again, the stimulus 1 was able to inhibit cell's activity. In figure 5.16 (a) it is possible to see that the mean value of the feedback trials is smaller than the mean value of the basal activity pre-feedback although, the standard deviation is quite large. This could be the result of bursting activity in the trial, for instance. Still, the results in the figure 5.16 (b) show a strong reduction in the firing rate during the feedback trials and reinforces once again that this stimulus could be exactly what we were looking for. More, in both, figures 5.15 (b) and 5.16 (b), the cells were almost completely silenced after the feedback stimulation. We were not surprised by the results of the figures 5.16 (c) and (d) since in the figure 5.15 (d) we already saw a slight reduction of the mean firing rate during the “real-time” feedback assays. More, both stimuli 1 and 2 are biphasic negative-then-positive with similar parameters and it was expected that they had similar behaviors in respect to their effects in neuronal activity modulation. We need just to highlight the fact that in figure 5.15 (b), in concordance with the firing rate significant reduction, it reveals a very small standard deviation indicating a possible fine control of cell's activity. The experiments where the stimuli 3 and 4 were used,

revealed inconsistency during the trials and for this reason, they were excluded from the next phase of our work.

Lastly, just to emphasize that the results displayed in the upper line of the figures 5.15 and 5.16 were performed using the same MEA chip and the same happened to the bottom lines. The stimulation effect is reversible and the activity tends to return or overcome the basal level, even during the course of the experiment or in the next day as shown in the mentioned figures. We did not make viability assays during the experiments although, during the days that the cells have been in culture, we monitored their state through observations of the culture under the microscope and also, we monitored their electrical properties through the MEA2100-System, to ensure that the cultures were in a good state to be used in our experiments.

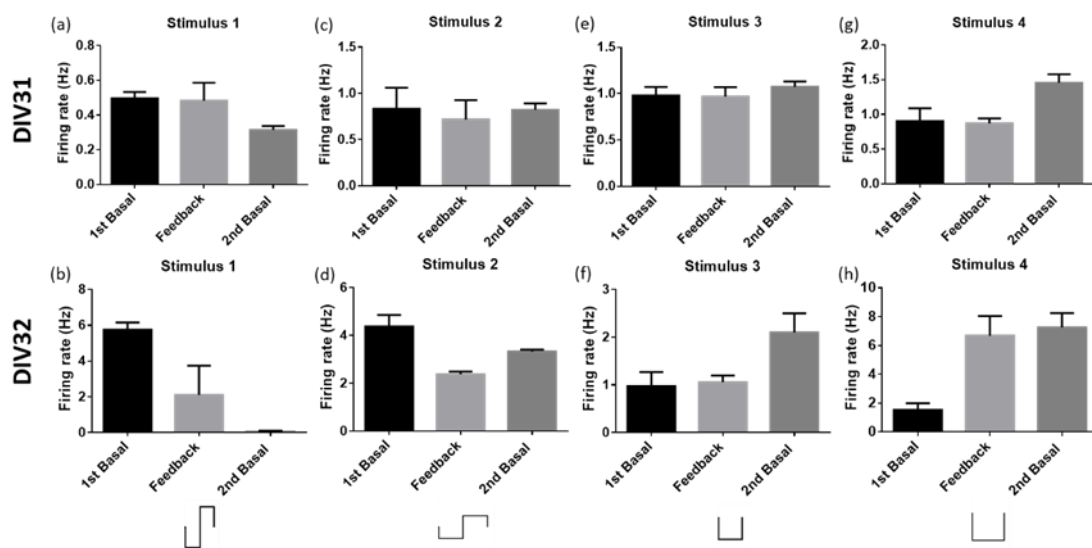


Figure 5.16 - Activity mean levels and respective standard deviations of the experiments (9 - 16) to validate the stimuli (without a stationary phase). (a,b) Biphasic negative-then-positive pulse with a width of $200 \mu s$ and $300 mV$ per phase. (c,d) Biphasic negative-then-positive pulse with a width of $500 \mu s$ and $200 mV$ per phase. (e,f) Monophasic negative pulse with a width of $180 \mu s$ and $550 mV$. (g,h) Monophasic negative pulse with a width of $280 \mu s$ and $800 mV$. (a, c, e, g) Cells at 31DIV. (b, d, f, h) Cells at 32DIV.

The results previously presented are exhibited in the figure 5.17 in the form of a ratio interval between the feedback mean firing rates and the basal pre-feedback mean firing rates. In this way is easier to see the effect of the stimuli in the previous experiments. One ratio interval inferior to one means that the stimulus tends to inhibit the spiking activity, otherwise, it tends to evoke APs (increase the activity).

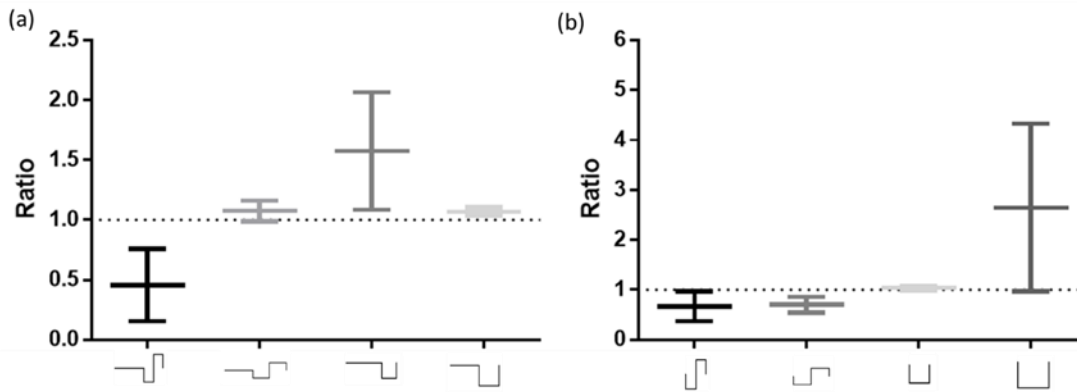


Figure 5.17 - Stimuli effect in the form of a ratio interval calculated between the feedback mean firing rates and the basal pre-feedback mean firing rates. (a) Ratio calculated from the results of the figure 5.15 (experiments 1 - 8). (b) Ratio calculated from the results of the figure 5.16 (experiments 9 - 16).

Before taking the last considerations about the validation of the stimuli, is only missing the explanation for the stimulus with three asterisks (***). As you can see from the table 5.2, these experiments (23 - 24) were one of the last experiments to be performed. Although, it says “Stimulus validation”. The reason to repeat the stimulus 1 validation was due to the fact that during our experiments using the MEA2100-256-System to try to control the activity of the network, or just part of that, we realized that (for reasons intrinsic to the system that we could not control), the baseline noise of the recording electrodes increased with the number of dedicated stimulation electrodes selected. This noise was not visually perceptible when using a scale in the range of the recorded APs amplitudes ($\sim 100 \mu V$). Although, during one experiment setup, we noticed a small noise elevation. Therefore, to have sure that our choice of the stimulus to use in the neuronal population activity control experiments (stimulus 1) was right, we repeated once again the stimuli validation protocol for the stimulus 1 (but in the MEA2100-120-System like the other experiments to validate the stimulus).

The three asterisks (***) in front of the stimulus 1 mean that in all the 3 phases of the protocol, the stimulation electrodes were always selected. Thus, the noise would be always present in the recordings and we did not take the risk of losing spikes due to a wrong detection threshold estimation caused by the increase of noise with consequences in the standard deviation value. The results are presented in the figure 5.18.

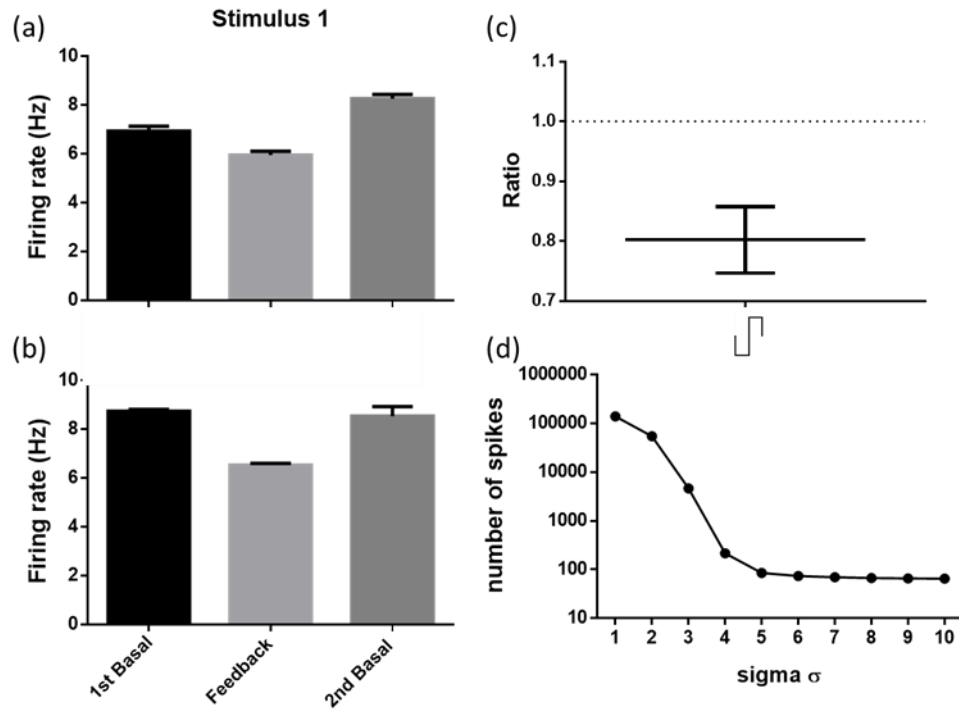


Figure 5.18 - Results of experiments 23 and 24 with a normalized noise level. (a, b) Activity mean levels and respective standard deviations using a biphasic negative-than-positive pulse with a width of $200 \mu s$ and $300 mV$ per phase. (a) Cells at 20DIV. (b) Cells at 21DIV. (c) Stimuli effect in the form of a ratio interval calculated between the feedback mean firing rates and the basal pre-feedback mean firing rates using the results of a and b. (d) Example of the variation curve of the number of detected spikes in relation to sigma σ .

These results confirm that a possible increase in the noise levels was not significant to be considered the main cause of the reduction in the firing rate on the previous results. At least, capable to provoke inhibitions in such large scales. More, by looking to the recorded signals we could not identify any perceptible increase in the baseline level of the signal in the MEA2100-120-System. The figure 5.18 (d) shows the variation in the number of spikes detected for different values of σ . It is noticeable that the accentuated decrease in the spikes number is between 3 and 4 σ , after that the curve tends to stabilize. Since we used a factor of 5 times σ to detect APs in our experiments, the small increase of the noise levels did not have such significant impact in the reduction of the activity. In addition, with these results, it is clear that the stimulus 1 is capable to reduce the neuronal activity of the cells over/near the recording electrode.

Finally, the last considerations about the validation of the stimuli are the following:

- These results show that the stimulus 1 was more consistent in inhibiting neuronal activity among all trials. Although the stimulus 2 also demonstrated good results in figure 5.16, we chose the stimuli 1 to the next set of experiments (network activity control) by the consistency demonstrated. Moreover, the product between its duration and amplitude is smaller compared with the stimulus 2, which is safer for the cells. In addition, its duration is smaller which reduces the time without recording signals by the blanking action of the system;

- We did not expect these results since according to Wagenaar et al. [126], ES by MEAs has been used to elicit activity in dissociated cultures and in their study, using cortical neurons, both biphasic negative-than-positive and monophasic negative voltage pulses were effective in evoking action potentials. In each trial, they tested the response (number of spikes) in the first 20 ms after stimulation. These responses to single events stimulations could not be compared with our “real-time” feedback stimulation. In addition, Vardi et al. in [127] did a study to understand the mechanisms underlying the low firing rates in neuronal networks (1 - 3 Hz) where were used monophasic negative pulses with similar parameters (width and amplitude) to the ones used in stimuli 3 and 4. This low firing rate results from the balance between excitatory and inhibitory synapses and their neuronal temporal coding, with a millisecond precision [127]. They reported that a stimulus similar to stimulus 3 enhances the inhibitory effect and another stimulus similar to stimulus 4 evoked neuronal response. However, the difference between their stimuli parameters and ours is in the width of the pulse. Our system has a delay of $40\ \mu\text{s}$ in each rising and falling phase of the pulse, to reach the maximum amplitude and to return to zero, respectively, which gives a difference of $80\ \mu\text{s}$ in relation to their stimuli. That difference in the pulses’ duration could be one of the factors that contribute to the disparity between our results and the results from their study. More, their results were obtained using low stimulation rates with the precision of neuronal response timings [127] and, in our experiments, we do not control the stimuli frequency since a stimulus is triggered when the feedback condition is fulfilled.
- Dissociated cortical cultures have a high propensity to bursting. According to Wagenaar et al. in [103], global bursts start to appear approximately at 7 DIV and after approximately 20 - 25 DIV, they start to dominate the culture activity [103]. In our experiments we started to see activity approximately at 7 DIV and the first bursts at 11 - 12 DIV. Although, this global synchronized bursting activity is more evident in high-density cultures [103]. Since burst activity depends on the formation of a network between the isolated and cultured cells, this behaviour may not be observed exactly after this mentioned DIV; in fact, our cultures, in general, took more time. Despite we did not use cultures with a dominant bursting activity, it is normal the occurrence of some burst activity during our experiments. Therefore, the frequency of triggered stimuli could be changed by bursting activity, which is a factor that we cannot control. For instance, during a burst, the feedback condition could be fulfilled many times and various stimuli could be triggered even if the rate (defined by the “Time Window” and the “Spike Count”) until the burst occurrence was lower than that defined rate. Moreover, periods with rare occurrence of spikes can also not trigger stimulation. According to Vardi et al. study [127], stimulation frequency has a great impact on neuronal activity control and if we cannot control it, it is one more challenge to modulate neuronal activity.

- The cultures variability should always be considered in this type of experiments. Despite the use of different cultures, more experiments need to be done to ensure the effectiveness of the stimulus to inhibit neuronal activity.
- Finally, the neuronal behavior post-stimulation demonstrated that the stimulation effect is reversible and the stimuli did not kill the cells. They maintained their electrical activity. In some cases, the cells were almost completely silenced, which is the case of the recordings where the stimulus 1 was applied, although, in the following day the cells returned to their normal activity level. In other cases, their activity started to increase immediately after the end of the feedback stimulation.

5.2.2. Neuronal network control experiments

The next set of results addresses some experiments where we applied the previously chosen stimulus to a large area of the neuronal culture through various stimulation electrodes uniformly distributed within the array of recording electrodes. The distribution of the stimulation electrodes was done in a way that ensures that each recording electrode has one stimulation electrode in its vicinity. The figure 5.19, display the two MEA layouts used in the experiments. The blue “boxes” correspond to the MEAs area that exhibited more activity during our experiments. The blue circles are the recording electrodes and the green ones are the electrodes used to stimulate. Here they are in green to be easily identified but in the software, they will appear in blue like the others because this window is just to select the electrodes that we want to use in the recordings. The other areas of the two used 256MEA chips had poor activity and, since the recordings produce a considerable amount of data, we opted to deselect the other electrodes.

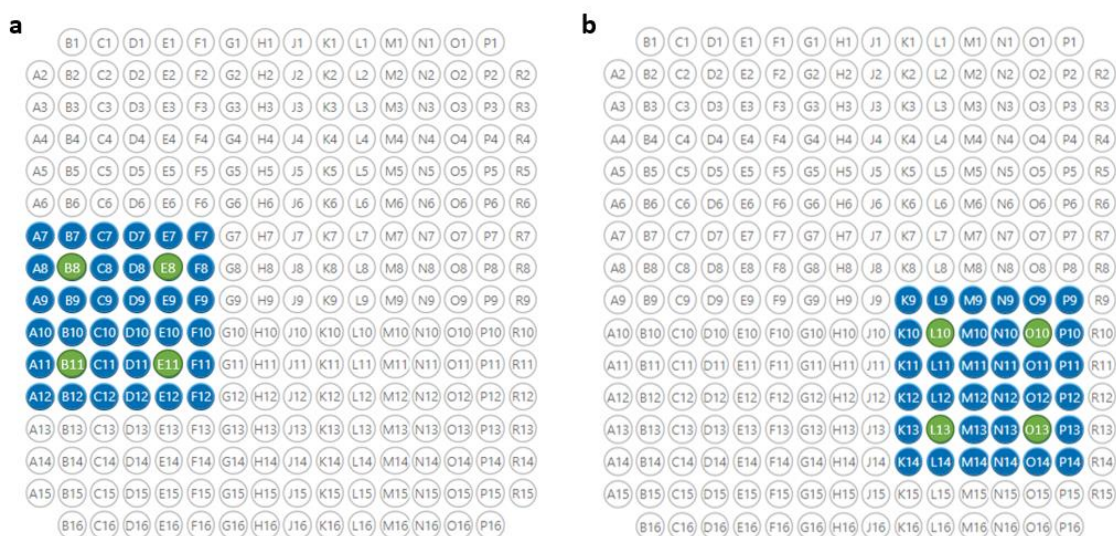


Figure 5.19 - Screen capture of the selected electrodes used in the experiments (18-22, 25). Recording electrodes (blue circles); Stimulation electrodes (green circles).

The results presented in the figure 5.20 compare three experiments using the same primary neuronal culture. These experiments correspond in the table 5.2 to the numbers 18, 20 and 22 (DIV19 - 22) and were performed with the MEA layout of the figure 5.19(a). The experiment 19 was also performed with the same MEA chip however, just a small number of electrodes had a considerable activity and for this reason, it is not shown in the figure below. To evaluate the neuronal activity of the network we only selected the electrodes with an activity larger than 1 Hz (at least in one of the plots) and correspond to approximately 12 electrodes.

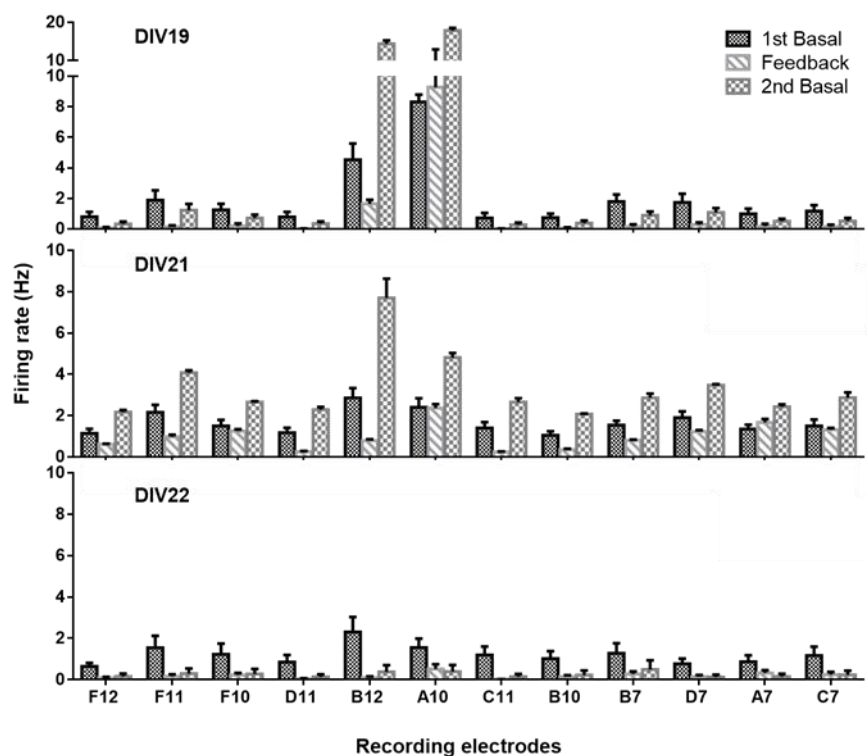


Figure 5.20 - Bar plot graphs showing the activity mean levels and respective standard deviations of the neuronal network experiments (18,20,22). In the figure are only present the electrodes that exhibited more than 1 Hz of activity. The respective DIVs are shown in the graphs.

In general, all the mean firing rates computed for each electrode were reduced during the “real-time” feedback. If we compare the “1st Basal” bar with the “Feedback” bar, the only two electrodes that disagree with the previous statement are the electrodes A10 at 19DIV and A7 at 21DIV. In the experiment 19 (data not shown), in 20DIV, despite the poor activity on almost all electrodes, overall, electrodes’ activity decreased, less in the electrode A7, similar to 21DIV results. However, the “Feedback” rate is in a small step below the spontaneous basal activity pre-feedback stimulation similar to DIV20 results. If we look at the following DIVs, A10 “Feedback” firing rate has a significant decrease as it is possible to see. There are several factors that may have contributed to this different behavior of the electrodes A10 and A7 in relation to the others; they were addressed before in this section when discussed the results of the stimuli validation. Another hypothesis can be the fact that these two electrodes are in the

border of the MEA. I.e, cultures of dissociated neurons after the isolation process adhere to the substrate and start to create connections between them to create the neuronal network characteristic of neurons. The area of the MEAs only corresponds to approximately 2% of the area of the chip where the neurons are cultured. Therefore, the neurons near/top of the electrodes A10 and A7 could be receiving more synaptic excitatory inputs from the rest of the culture (that did not receive any type of direct stimulation through the electrodes). In addition, in these experiments is even more complicated to set the “Spikes Count” value since we need to look for a larger number of electrodes and estimate the number of spikes within a 1000 ms window, which is not the ideal method. Lastly, it is fair to say that, in general, the feedback stimulation was capable to inhibit part of the activity of the neuronal network over the stimulation electrodes range, not only in each experiment but also, throughout the days of experiments, the studied network is moving towards a decrease in its global activity. Despite the stimulation, this also could be a result of the consecutive and relatively longer ($> 30 \text{ min}$) experiments. With the temperature regulator we expect to minimize the temperature impact in the culture, however, there are a lot of other factors such as the lack of a controlled atmosphere like the one encountered in an incubator, among others, that could lead to the decline of the activity, or even of the culture. The response post-feedback was inconsistent, sometimes the activity surpassed the basal activity pre-feedback. The results of the figure 5.21 show exactly this behavior. Although, in other cases, this did not happen and we will not take considerations from that. Again, plasticity studies are required to evaluate these events and, plasticity is not the focus of this work.

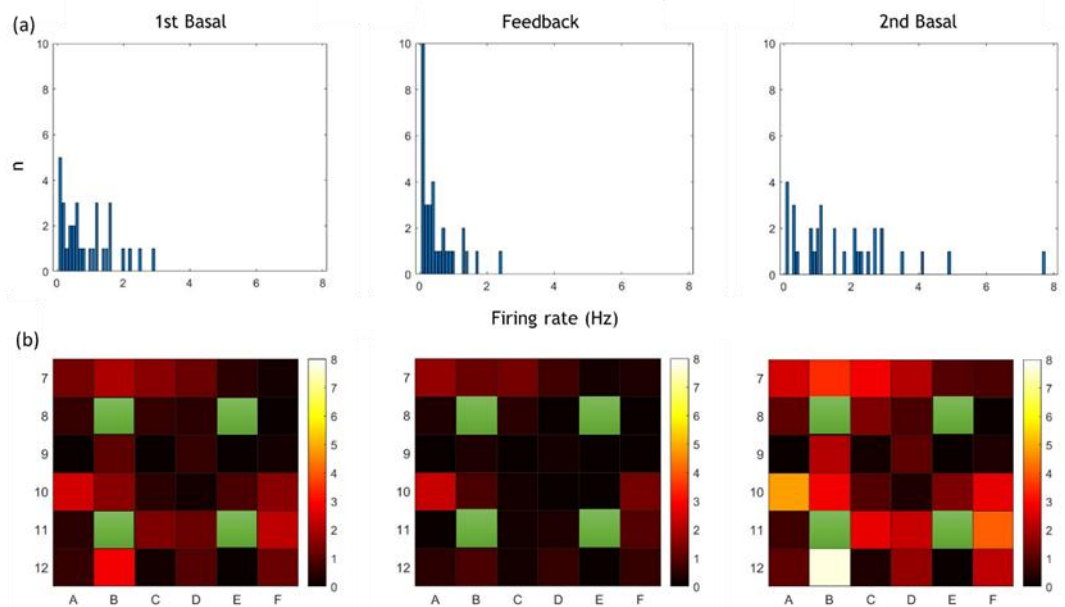


Figure 5.21 - Complementary results of the experiment 20 (at 21DIV). (a) Histograms (in the form of bar plots) showing the variation in the firing rates of all recording electrodes during the experiment. (b) Color maps showing the spatial distribution of the activity in the recording electrodes over the experiment. The green squares correspond to the stimulation electrodes.

The figure above completes the results obtained from the experiment 20 (21DIV). In figure 5.21 (a), the histograms (in the form of bar plots), distribute the firing rates calculated in our

experiment by their number of occurrences within well-defined rate intervals. In the feedback plot, we can see a shift in the frequencies to the left side of the graph in the direction of small frequency values when compared with the basal activity pre-stimulation graph. This behavior is also observed in the histogram plots of the other experiments presented in the figures 1, 2 and 3 (available in Appendix A). The colormaps (figure 5.21(b)), give us a visual perception of the firing rate spatially distributed over the recording electrodes. The green squares are the stimulation electrodes. Once again, the colormaps of the remaining experiments can be consulted in Appendix A.

The MEA layout of the figure 5.19 (b) was used in the experiments 21 and 25. Another primary cortical culture was made in a different 256MEA chip and the experiments were performed in DIV21 and 22. Note that the experiment 25 has the three asterisks (***) in the stimulus column of the table 5.2. This means that this last experiment, similar to the experiments 23 and 24, was also made with the stimulation electrodes selected since the beginning of the experiments. I.e., like the feedback recordings, both basal activity (1st and 2nd) had the stimulation electrodes always dedicated to stimulation. This enables us to normalize the 3 trials for each protocol phase (“1st Basal”, “Feedback” and “2nd Basal”) in relation to the system noise levels. These results can be consulted in the figure 5.22. To analyze the data were only considered the electrodes with a firing rate larger than 0.5 Hz (at least in one of the compared DIVs), which are half of the recorded electrodes (16 in 32).

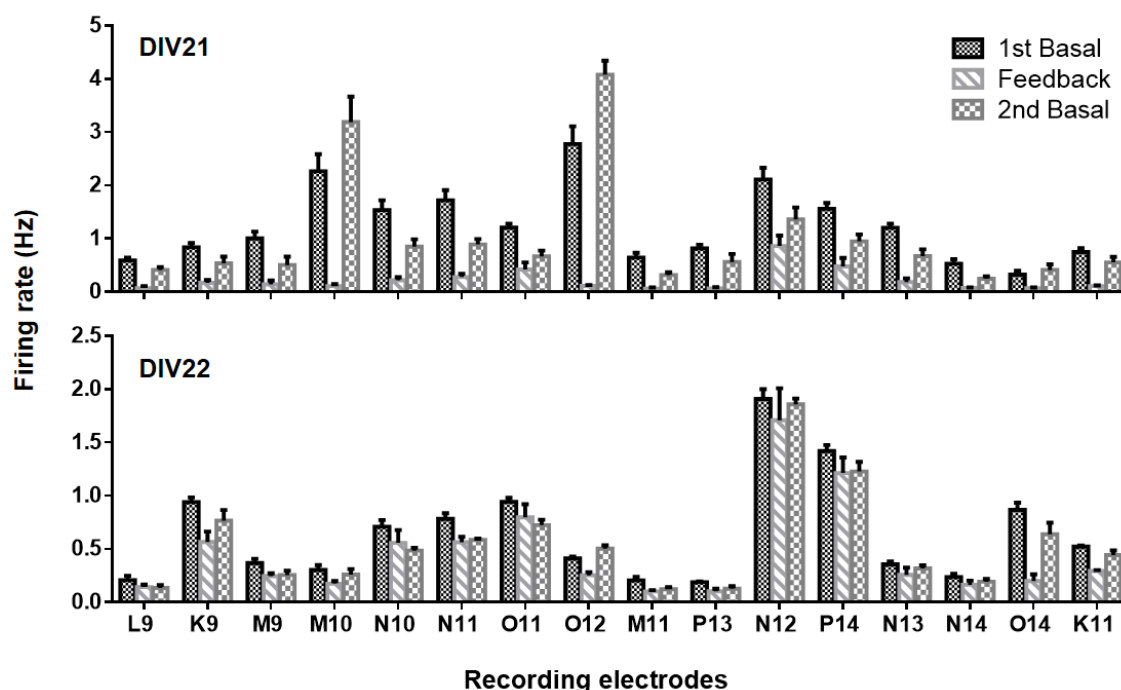


Figure 5.22 - Bar plot graphs showing the activity mean levels and respective standard deviations of the neuronal network experiments (23,24). In the figure are only present the electrodes that exhibited more than 0.5 Hz of activity. The respective DIVs are shown in the graphs. The bottom graph results were obtained in normalized noise conditions.

Once again the results exhibited a reduction in the firing rate in all electrodes, according to what we had seen in the results previously shown. Despite the reduction in the overall firing rate in DIV22 compared with DIV21, the experiment 25 (DIV22) is truly relevant in the sense that with a normalized noise throughout all the 9 recordings of this experiment, we can see an inhibition of the network activity. The only electrode with a significant standard deviation from the mean is the electrode N12. The complementary analysis of the experiment 25 is presented in the figure 5.23 and, in the case of experiment 21, it can be found in Appendix A.

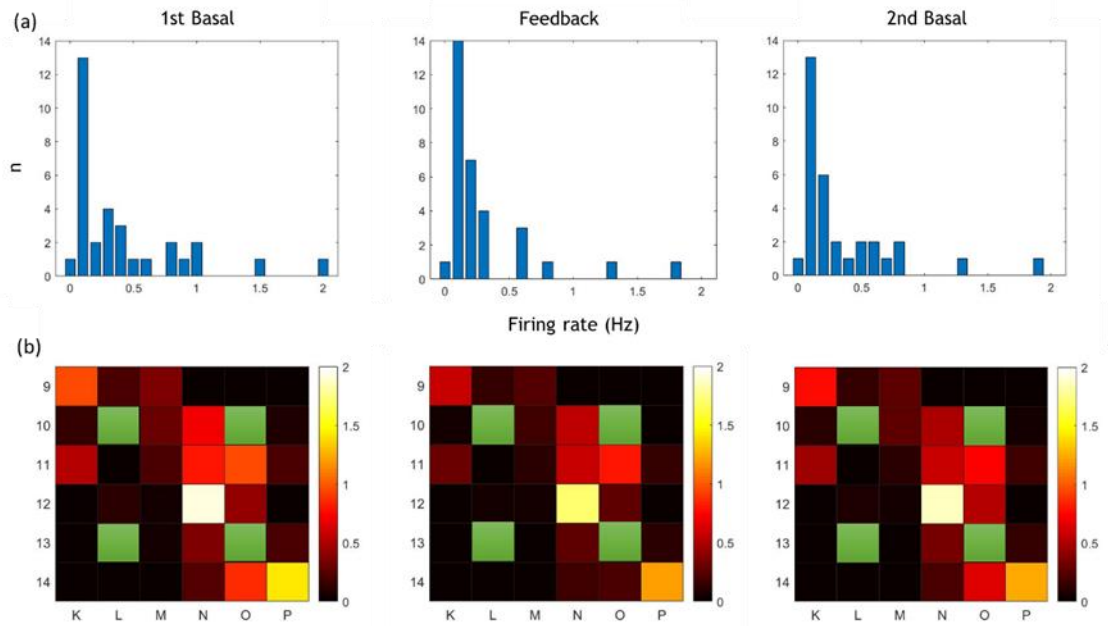


Figure 5.23 - Complementary results of the experiment 25 (at 22DIV) with normalized noise conditions. (a) Histograms (in the form of bar plots) showing the variation in the firing rates of all recording electrodes during the experiment. (b) Color maps showing the spatial distribution of the activity in the recording electrodes over the experiment. The green squares correspond to the stimulation electrodes.

It is important to discuss the reduction of the activity from DIV21 to DIV22. This reduction may be a result of the day before experiment similar to what happened in the course of the experiments 18, 20 and 22 (figure 5.20). Although, the other hypothesis is that the non-standardization of the noise levels throughout the entire experiment could contribute to a bigger level of activity during the Basal recordings. The noise levels without select dedicated stimulation electrodes and with their selection are presented in the figure 5.24, as well as the curves which characterize the number of spikes detected with the sigma variation.

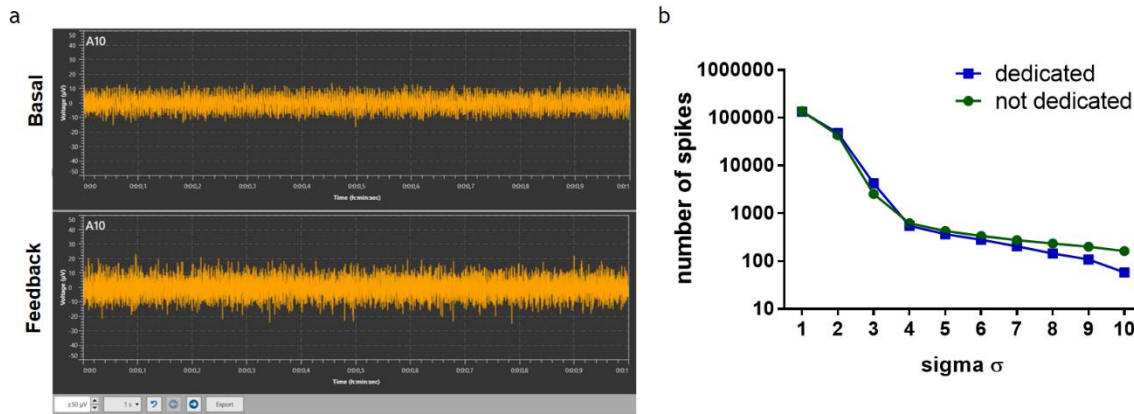


Figure 5.24 - Baseline noise levels of the system using dedicated and not dedicated stimulation electrodes. (a) Comparison between the baseline noise levels in basal recordings without select dedicated electrodes to stimulation ($\sim \pm 10 \mu V$) and in feedback recordings with dedicated stimulation electrodes ($\sim \pm 20 \mu V$). (b) Example of the variation curve of the number of detected spikes in relation to sigma σ , in both cases.

In the figure 5.24 (a-Basal) is compared the baseline level of our recordings without select dedicated stimulation electrodes (Basal recordings) and, this level ranges around $\pm 10 \mu V$ while in the figure 5.24 (a-Feedback), this value ranges around $\pm 20 \mu V$ when the stimulation electrodes are dedicated to stimulation (Feedback recordings), which is a considerable difference. If we compare the curves in the figure 5.24 (b) (for the same electrode), the curves have similar behavior and for a factor of 5 times the σ , the spikes number is similar but slightly inferior to the dedicated stimulation electrodes. It is possible that, using the MEA2100-256-System some small APs will not be counted in the Feedback recordings however, we do not believe that such large reductions in some cases were due to this undetection of some APs. In addition, the experiment 25 with noise normalized conditions give us a lot of confidence in the ability of the stimulus 1 to inhibit the activity of the neuronal network.

The experiment 17 will not be discussed here since were used 12 dedicated stimulation electrodes which, increased the systems' noise ($\pm 25 - 30 \mu V$ signal's baseline level). However, it was used an area of 132 electrodes which enabled the study of a large neuronal network. For these reasons, the results are available in the Appendix A.

Finally, to conclude this section, with the MEA2100-System we can close the loop between recording and "real-time" feedback stimulation even though, in a limited way. It should be noted that the system has a delay of about 1 ms, however, it is very small. Although we demonstrated that we can inhibit the activity of neuronal cells with our protocol and validated stimulus, it was very limited in the sense that we did not have a fine control of the activity levels. I. e., we could not maintain the cells firing within a well-defined interval of firing rates. The lack of a more precise tool to estimate the mean firing rate of the neuronal cells (instead of a small window of time that count the number of spikes within it) is also another restriction to achieve a good control. To overcome these limitations our work is going beyond a control using only the MCS Experimenter software to apply the closed-loop control. We are progressing to a direct control of the DSP of the MEA2100-System through MATLAB to design and implement our own closed-loop control system. More details will be presented further ahead.

5.3. Future Perspectives

The MEA2100-System is equipped with a freely programmable DSP that allows the access to the data stream from all electrodes in real-time and, it also can access the stimulators. Thus, the next step of this work will be the creation of a closed-loop control system by controlling directly the DSP via MATLAB. This will reduce the time delay of about 1 ms when controlled by the data acquisition software (MSC Experimenter). So far, with MATLAB we are able to initialize the system, set up the recording parameters like the sample rate, convert the recorded data units to μV , select the electrodes and plot the recorded data in real-time. Future work will go through the implementation of an algorithm to make a feasibility estimation of the firing rate in real-time, capable to lead with some limitations of the current acquisition software as the occurrence of burst activity. In an initial phase of the work, the feedback should be capable to maintain the firing rate values within a range defined by the user. This will be done by implement at least two feedback conditions: one to trigger an excitatory stimulation every time the firing rate is below the minimum range limit and another condition to do the opposite, i.e., trigger an inhibitory stimulation when the firing rate overcomes the maximum defined value. More, the data stream for each electrode must be individually monitored and if any of the feedback conditions is fulfilled, a targeted stimulation should be triggered in that electrode. To do that, the electrodes cannot be dedicated only to stimulation, they also need to record. Maybe, instead of an individual monitoring added to an individual stimulation of each electrode, we should start to divide the MEA in small regions and try to modulate their activity.

Finally, in this dissertation, we already have shown a proof-of-concept of how to control and modulate the firing rate using a classical PID controller implemented in an *in silico* model of a neuron. Another daring step could be the design and implementation of a controller of this type in MATLAB capable to modulate the stimulus parameters according to the controlling needs to maintain the firing rate at a stable level. On the other hand, impose specific behaviors, for instance, originate a burst in a precise part of the neuronal culture or even detect a recognizable electrical signature such as an epileptiform activity and trigger a specific stimulus. This could be hard and too ambitious goals to achieve but let's see what the future holds...

Chapter 6

Conclusion

The majority of medical treatments using ES are open-loop systems where the stimulation parameters remain constant despite the brain's state or the disease progress level. From a clinical point of view, it is expected that real-time closed-loop systems will be more effective to treat neuronal disorders since stimulation will be adapted according to the state of each patient, in a continuous and dynamic way, similar to what happens in a normal brain circuitry. Although to autonomously control and modulate neuronal activity, new neuro-electronic interfaces are needed, capable of both recording and stimulating.

In electrophysiology, MEAs are the best platforms at network-level used to simultaneous, parallel, multisite and long-term recordings and stimulations of neuronal populations. However, as reviewed in the present work, the standard MEAs have many limitations such as their low level of electrical coupling with the cells and their SNR. Despite closed-loop systems have the potential to be the true solution for the identified problem in current neurorehabilitation treatments, significant improvements in neuro-electronic interfaces should be done. Many labs already started to improve this by developing a new type of microelectrodes- 3D-structured microelectrodes - which protrude from a planar substrate.

This work demonstrates two different control methodologies using closed-loop systems to control neuronal activity. The first one is a theoretical proof-of-concept that shows that classical PID controllers have the potential to be implemented in closed-loop control systems to modulate neuronal activity. The results of the simulations prove that despite abrupt changes in the firing rate of the simulated neuron or, the introduction of noise in the system, the controller is always capable to adjust the current injected in the model according to the system's needs to bring back the firing rate to the reference value. The controller demonstrated a fast response and the closed-loop system stayed stable during the simulations. Although, it is important to emphasize that this was only a proof-of-concept and for a clinical application, the controller should be much more robust.

The results of the “real-time” closed-loop experiments using the MEA2100-System are consistent. The experiments to validate the stimuli show that a biphasic negative-than-positive stimulation pulse with an amplitude of 300 mV and 200 μ s of duration per phase was the most effective stimulus to inhibit the neuronal activity. Moreover, when used the same stimulus in the experiments to modulate the mean activity at the network level, the results are once again in accordance with the stimuli validation studies. Despite the listed limitations of this control system, it was demonstrated that is possible to close the loop between recording and “real-time” feedback stimulation to constrain the global activity below its spontaneous basal level of firing rate. In addition, the freely programmable MEA2100-System’s DSP could be explored to significantly improve the performance of the “real-time” feedback and, possible future work should take this into account.

References

- [1] D. Purves *et al.*, Eds., *Neuroscience*, 3rd ed. Sunderland, MA: Sinauer Associates, Inc., 2004.
- [2] R. Chen, A. Canales, and P. Anikeeva, "Neural recording and modulation technologies," *Nat. Rev. Mater.*, vol. 2, pp. 1-16, 2017.
- [3] M.-G. Liu, X.-F. Chen, T. He, Z. Li, and J. Chen, "Use of multi-electrode array recordings in studies of network synaptic plasticity in both time and space," *Neurosci. Bull.*, vol. 28, no. 4, pp. 409-422, 2012.
- [4] F. A. C. Azevedo *et al.*, "Equal numbers of neuronal and nonneuronal cells make the human brain an isometrically scaled-up primate brain," *J. Comp. Neurol.*, vol. 513, no. 5, pp. 532-541, 2009.
- [5] M. E. J. Obien, K. Deligkaris, T. Bullmann, D. J. Bakkum, and U. Frey, "Revealing neuronal function through microelectrode array recordings," *Front. Neurosci.*, vol. 8, no. 423, pp. 1-30, 2015.
- [6] R. Kim, S. Joo, H. Jung, N. Hong, and Y. Nam, "Recent Trends in Microelectrode Array Technology for In Vitro Neural Interface Platform," *Biomed. Eng. Lett.*, vol. 4, pp. 129-141, 2014.
- [7] D. Sterratt, B. Graham, A. Gillies, and D. Willshaw, *Principles of Computational Modelling in Neuroscience*. Cambridge University Press, 2012.
- [8] M. E. Spira and A. Hai, "Multi-electrode array technologies for neuroscience and cardiology," *Nat. Nanotechnol.*, vol. 8, no. 2, pp. 83-94, 2013.
- [9] M. R. Angle, B. Cui, and N. A. Melosh, "Nanotechnology and neurophysiology," *Curr. Opin. Neurobiol.*, vol. 32, pp. 132-140, 2015.
- [10] J. Pakpoor and M. Goldacre, "Neuroepidemiology: The increasing burden of mortality from neurological diseases," *Nat. Rev. Neurol.*, vol. 13, no. 9, pp. 518-519, 2017.
- [11] D. Silberberg, N. P. Anand, K. Michels, and R. N. Kaloria, "Brain and other system disorders across the lifespan — global challenges and opportunities," *Nature*, vol. 527, no. 7578, pp. S151-S154, 2015.
- [12] E. Castel-Lacanal, "Sites of electrical stimulation used in neurology," *Ann. Phys. Rehabil. Med.*, vol. 58, no. 4, pp. 201-207, 2015.
- [13] M. S. Sharifi, "Treatment of neurological and psychiatric disorders with deep brain stimulation; Raising hopes and future challenges," *Basic Clin. Neurosci.*, vol. 4, no. 3, pp. 84-88, 2013.
- [14] M. Arsiero, H.-R. Luscher, and M. Giugliano, "Real-Time closed-loop electrophysiology: towards new frontiers in in vitro investigations in the neurosciences," *Arch. Ital. Biol.*, vol. 145, pp. 193-209, 2007.

- [15] D. R. Kipke *et al.*, “Advanced Neurotechnologies for Chronic Neural Interfaces: New Horizons and Clinical Opportunities,” *J. Neurosci.*, vol. 28, no. 46, pp. 11830-11838, 2008.
- [16] J. D. Rolston, R. E. Gross, and S. M. Potter, “Closed-loop, open-source electrophysiology,” *Front. Neurosci.*, vol. 4, pp. 1-8, 2010.
- [17] X. L. Chen, Y. Y. Xiong, G. L. Xu, and X. F. Liu, “Deep Brain Stimulation,” *Interv. Neurol.*, vol. 1, pp. 200-212, 2012.
- [18] P. Hickey and M. Stacy, “Deep Brain Stimulation : A Paradigm Shifting Approach to Treat Parkinson ’ s Disease,” *Front. Neurosci.*, vol. 10, pp. 1-11, 2016.
- [19] B. S. Wilson and M. F. Dorman, “Interfacing sensors with the nervous system: Lessons from the development and success of the cochlear implant,” *IEEE Sens. J.*, vol. 8, no. 1, pp. 131-147, 2008.
- [20] A. K. Ahuja *et al.*, “Blind subjects implanted with the Argus II retinal prosthesis are able to improve performance in a spatial-motor task,” *Br. J. Ophthalmol.*, vol. 95, no. 4, pp. 539-543, 2011.
- [21] E. Zrenner *et al.*, “Subretinal electronic chips allow blind patients to read letters and combine them to words,” *Proc. R. Soc.*, vol. 278, no. 1711, pp. 1489-1497, 2011.
- [22] J. D. Rolston, R. E. Gross, and S. M. Potter, “A low-cost multielectrode system for data acquisition enabling real-time closed-loop processing with rapid recovery from stimulation artifacts,” *Front. Neuroeng.*, vol. 2, pp. 1-17, 2009.
- [23] T. W. Berger *et al.*, “Restoring lost cognitive function,” *IEEE Eng. Med. Biol. Mag.*, vol. 24, no. 5, pp. 30-44, 2005.
- [24] J. Dragas *et al.*, “In Vitro Multi-Functional Microelectrode Array Featuring 59760 Electrodes, 2048 Electrophysiology Channels , Stimulation , Impedance Measurement , and Neurotransmitter Detection Channels,” *IEEE J. Solid-State Circuits*, vol. 52, no. 6, pp. 1576-1590, 2017.
- [25] P. Dayan and L. F. Abbott, *Theoretical Neuroscience: Computational and Mathematical Modeling of Neural Systems*, 6th ed. Massachusetts Institute of Technology Press, 2005.
- [26] A. L. Hodgkin and A. F. Huxley, “A quantitative description of membrane current and its applicaiton to conduction and excitation in nerve,” *J. Physiol.*, vol. 117, no. 4, pp. 500-544, 1952.
- [27] S. Finger, “Benjamin Franklin, electricity, and the palsies: On the 300th anniversary of his birth,” *Hist. Neurol.*, vol. 66, no. 10, pp. 1559-1563, 2006.
- [28] D. Khudhair, S. Nahavandi, H. Garmestani, and A. Bhatti, “Microelectrode Arrays: Architecture, Challenges and Engineering Solutions,” in *Emerging Trends in Neuro Engineering and Neural Computation*, Singapore: Springer Nature, 2017, pp. 41-60.
- [29] H. N. Rubaiy, “A Short Guide to Electrophysiology and Ion Channels,” *J. Pharm. Pharm. Sci.*, vol. 20, pp. 48-67, 2017.
- [30] M. Piccolino, “Animal electricity and the birth of electrophysiology: The legacy of Luigi Galvani,” *Brain Res. Bull.*, vol. 46, no. 5, pp. 381-407, 1998.
- [31] M. Piccolino, “Luigi Galvani and animal electricity: Two centuries after the foundation of electrophysiology,” *Trends Neurosci.*, vol. 20, no. 10, pp. 443-448, 1997.
- [32] B. Hille, *Ion Channels of Excitable Membrans*, 3rd ed. Sunderland, MA: Sinauer Associates, Inc., 2001.
- [33] A. L. Hodgkin and A. F. Huxley, “Action Potentials Recorded from Inside a Nerve Fiber,” *Nature*, vol. 144, pp. 710-711, 1939.
- [34] A. L. Hodgkin and A. F. Huxley, “Movement of sodium and potassium ions during nervous activity,” *Cold Spring Harb. Symp. Quant. Biol.*, vol. 17, pp. 43-52, 1952.
- [35] E. Neher, B. Sakmann, and J. H. Steinbach, “The extracellular patch clamp: A method for resolving currents through individual open channels in biological membranes,” *Pflügers Arch. Eur. J. Physiol.*, vol. 375, no. 2, pp. 219-228, 1978.
- [36] C. Thomas, L. Springer, P. Loeb, G. Berwald-Netter, and Y. Okun, “A Miniature

- Microelectrode Array to Monitor the Bioelectric Activity of Cultured Cells,” *Exp. Cell Res.*, vol. 74, no. 972, pp. 61-66, 1972.
- [37] G. W. Gross, E. Rieske, G. W. Kreutzberg, and A. Meyer, “A new fixed-array multi-microelectrode system designed for long-term monitoring of extracellular single unit neuronal activity in vitro,” *Neurosci. Lett.*, vol. 6, no. 2-3, pp. 101-105, 1977.
- [38] G. W. Gross, “Simultaneous Single Unit Recording in vitro with a Photoetched Laser Deinsulated Gold Multimicroelectrode Surface,” *IEEE Trans. Biomed. Eng.*, vol. BME-26, no. 5, pp. 273-279, 1979.
- [39] J. Pine, “Recording action potentials from cultured neurons with extracellular microcircuit electrodes,” *J. Neurosci. Methods*, vol. 2, no. 1, pp. 19-31, 1980.
- [40] W. Nisch, J. Böck, U. Egert, H. Hämmerle, and A. Mohr, “A thin film microelectrode array for monitoring extracellular neuronal activity in vitro,” *Biosens. Bioelectron.*, vol. 9, no. 9-10, pp. 737-741, 1994.
- [41] U. Egert *et al.*, “A novel organotypic long-term culture of the rat hippocampus on substrate-integrated multielectrode arrays,” *Brain Res. Protoc.*, vol. 2, no. 4, pp. 229-242, 1998.
- [42] H. Oka, K. Shimono, R. Ogawa, H. Sugihara, and M. Taketani, “A new planar multielectrode array for extracellular recording: application to hippocampal acute slice,” *J. Neurosci. Methods*, vol. 93, pp. 61-67, 1999.
- [43] M. M. Heinreicher, “Principles of Extracellular Single-Unit Recording,” in *Microelectrode Recording in Movement Disorder Surgery*, Z. Israel and K. Burchiel, Eds. Thieme, 2004, pp. 8-13.
- [44] D. A. Henze, Z. Borhegyi, J. Csicsvari, A. Mamiya, K. D. Harris, and G. Buzsáki, “Intracellular features predicted by extracellular recordings in the hippocampus in vivo,” *J. Neurophysiol.*, vol. 84, no. 1, pp. 390-400, 2000.
- [45] G. Buzsáki, C. A. Anastassiou, and C. Koch, “The origin of extracellular fields and currents – EEG , ECoG , LFP and spikes,” *Nat. Rev. Neurosci.*, vol. 13, pp. 407-420, 2012.
- [46] R. Quian Quiroga, “What is the real shape of extracellular spikes?,” *J. Neurosci. Methods*, vol. 177, no. 1, pp. 194-198, 2009.
- [47] U. Frey, U. Egert, F. Heer, S. Hafizovic, and A. Hierlemann, “Microelectronic system for high-resolution mapping of extracellular electric fields applied to brain slices,” *Biosens. Bioelectron.*, vol. 24, no. 7, pp. 2191-2198, 2009.
- [48] S. Shoham, D. H. O’Connor, and R. Segev, “How silent is the brain: Is there a ‘dark matter’ problem in neuroscience?,” *J. Comp. Physiol. A*, vol. 192, no. 8, pp. 777-784, 2006.
- [49] M. Mayford, S. A. Siegelbaum, and E. R. Kandel, “Synapses and Memory Storage,” *Cold Spring Harb. Perspect. Biol.*, vol. 4, no. 6, pp. 1-18, 2012.
- [50] A. L. Barth and J. F. A. Poulet, “Experimental evidence for sparse firing in the neocortex,” *Trends Neurosci.*, vol. 35, no. 6, pp. 345-355, 2012.
- [51] A. Belitski *et al.*, “Low-Frequency Local Field Potentials and Spikes in Primary Visual Cortex Convey Independent Visual Information,” *J. Neurosci.*, vol. 28, no. 22, pp. 5696-5709, 2008.
- [52] J. J. Sun, W. Kilb, and H. J. Luhmann, “Self-organization of repetitive spike patterns in developing neuronal networks in vitro,” *Eur. J. Neurosci.*, vol. 32, no. 8, pp. 1289-1299, 2010.
- [53] J. O’Neill, T. J. Senior, K. Allen, J. R. Huxter, and J. Csicsvari, “Reactivation of experience-dependent cell assembly patterns in the hippocampus,” *Nat. Neurosci.*, vol. 11, no. 2, pp. 209-215, 2008.
- [54] T. Abel, R. Havekes, J. M. Saletin, and M. P. Walker, “Sleep, plasticity and memory from molecules to whole-brain networks,” *Curr. Biol.*, vol. 23, no. 17, pp. R774-R788, 2013.
- [55] A. Hai, J. Shappir, and M. E. Spira, “Long-Term , Multisite , Parallel , In-Cell Recording and Stimulation by an Array of Extracellular Microelectrodes,” *J. Neurophysiol.*, vol. 104,

- pp. 559-568, 2010.
- [56] B. Sakmann and E. Neher, "Patch Clamp Techniques for Studying Ionic Channels in Excitable Membranes," *Annu. Rev. Physiol.*, vol. 46, no. 1, pp. 455-472, 1984.
 - [57] A. Verkhratsky, O. A. Krishtal, and O. H. Petersen, "From Galvani to patch clamp: The development of electrophysiology," *Pflugers Arch. Eur. J. Physiol.*, vol. 453, no. 3, pp. 233-247, 2006.
 - [58] C. Wood, C. Williams, and G. J. Waldron, "Patch clamping by numbers," *Drug Discov. Today*, vol. 9, no. 10, pp. 434-441, 2004.
 - [59] F. Franke *et al.*, "High-density microelectrode array recordings and real-time spike sorting for closed-loop experiments: an emerging technology to study neural plasticity," *Front. Neural Circuits*, vol. 6, pp. 1-7, 2012.
 - [60] L. Berdondini, K. Imfeld, A. Maccione, M. Tedesco, and S. Neukom, "Active pixel sensor array for high spatio-temporal resolution electrophysiological recordings from single cell to large scale neuronal networks," *Lab Chip*, vol. 9, no. 18, pp. 2644-2651, 2009.
 - [61] M. Hutzler, A. Lambacher, B. Eversmann, M. Jenkner, R. Thewes, and P. Fromherz, "High-Resolution Multitransistor Array Recording of Electrical Field Potentials in Cultured Brain Slices," *J. Neurophysiol.*, vol. 96, no. 3, pp. 1638-1645, 2006.
 - [62] A. Hai, J. Shappir, and M. E. Spira, "In-cell recordings by extracellular microelectrodes," *Nat. Methods*, vol. 7, no. 3, pp. 200-202, 2010.
 - [63] N. Shmoel, N. Rabieh, S. M. Ojovan, H. Erez, E. Maydan, and M. E. Spira, "Multisite electrophysiological recordings by self-assembled loose-patch-like junctions between cultured hippocampal neurons and mushroom-shaped microelectrodes," *Sci. Rep.*, vol. 6, pp. 1-11, 2016.
 - [64] P. Fromherz, A. Offenhausser, T. Vetter, and J. Weis, "A Neuron-Silicon Junction: A Retzius Cell of the Leech on an Insulated-Gate Field-Effect Transistor," *Science*, vol. 252, pp. 1290-1293, 1991.
 - [65] P. Fromherz, "Three levels of neuroelectronic interfacing: Silicon chips with ion channels, nerve cells, and brain tissue," *Ann. N. Y. Acad. Sci.*, vol. 1093, pp. 143-160, 2006.
 - [66] G. T. Einevoll, F. Franke, E. Hagen, C. Pouzat, and K. D. Harris, "Towards reliable spike-train recordings from thousands of neurons with multielectrodes," *Curr. Opin. Neurobiol.*, vol. 22, no. 1, pp. 11-17, 2012.
 - [67] G. T. Einevoll, C. Kayser, N. K. Logothetis, and S. Panzeri, "Modelling and analysis of local field potentials for studying the function of cortical circuits," *Nat. Rev. Neurosci.*, vol. 14, no. 11, pp. 770-785, 2013.
 - [68] G. Neves, S. F. Cooke, and T. V. P. Bliss, "Synaptic plasticity, memory and the hippocampus: a neural network approach to causality," *Nat. Rev. Neurosci.*, vol. 9, no. 1, pp. 65-75, 2008.
 - [69] S. M. Ojovan *et al.*, "A feasibility study of multi-site, intracellular recordings from mammalian neurons by extracellular gold mushroom-shaped microelectrodes," *Sci. Rep.*, vol. 5, pp. 1-14, 2015.
 - [70] A. Cohen, J. Shappir, S. Yitzchaik, and M. E. Spira, "Reversible transition of extracellular field potential recordings to intracellular recordings of action potentials generated by neurons grown on transistors," *Biosens. Bioelectron.*, vol. 23, no. 6, pp. 811-819, 2008.
 - [71] M. Jenkner and P. Fromherz, "Bistability of membrane conductance in cell adhesion observed in a neuron transistor," *Phys. Rev. Lett.*, vol. 79, no. 23, pp. 4705-4708, 1997.
 - [72] A. Hai *et al.*, "Spine-shaped gold protrusions improve the adherence and electrical coupling of neurons with the surface of micro-electronic devices," *J. R. Soc. Interface*, vol. 6, no. 41, pp. 1153-65, 2009.
 - [73] R. H. Olsson, D. L. Buhl, A. M. Sirota, G. Buzsaki, and K. D. Wise, "Band-tunable and multiplexed integrated circuits for simultaneous recording and stimulation with microelectrode arrays," *IEEE Trans. Biomed. Eng.*, vol. 52, no. 7, pp. 1303-1311, 2005.

- [74] T. Hashimoto, C. M. Elder, and J. L. Vitek, "A template subtraction method for stimulus artifact removal in high-frequency deep brain stimulation," *J. Neurosci. Methods*, vol. 113, no. 2, pp. 181-186, 2002.
- [75] D. A. Wagenaar and S. M. Potter, "Real-Time Multi-Channel Stimulus Artifact Suppression by Local Curve Fitting," *J. Neurosci. Methods*, vol. 120, no. 2, pp. 113-120, 2002.
- [76] F. Heer, S. Hafizovic, W. Franks, A. Blau, C. Ziegler, and A. Hierlemann, "CMOS microelectrode array for bidirectional interaction with neuronal networks," *IEEE J. Solid-State Circuits*, vol. 41, no. 7, pp. 1620-1629, 2006.
- [77] U. Frey *et al.*, "Switch-matrix-based high-density microelectrode array in CMOS technology," *IEEE J. Solid-State Circuits*, vol. 45, no. 2, pp. 467-482, 2010.
- [78] A. Hassibi, R. Navid, R. W. Dutton, and T. H. Lee, "Comprehensive study of noise processes in electrode electrolyte interfaces," *J. Appl. Phys.*, vol. 96, no. 2, pp. 1074-1082, 2004.
- [79] X. Liu, A. Demosthenous, and N. Donaldson, "On the noise performance of Pt electrodes.," in *29th Annual International Conference of the IEEE Engineering in Medicine and Biology Society*, 2007, pp. 434-436.
- [80] L. A. Camuñas-Mesa and R. Q. Quiroga, "A Detailed and Fast Model of Extracellular Recordings," *Neural Comput.*, vol. 25, no. 5, pp. 1191-1212, 2013.
- [81] Y. Nam and B. C. Wheeler, "In vitro microelectrode array technology and neural recordings.," *Crit. Rev. Biomed. Eng.*, vol. 39, no. 1, pp. 45-61, 2011.
- [82] K. A. Ludwig, J. D. Uram, J. Yang, D. C. Martin, and D. R. Kipke, "Chronic neural recordings using silicon microelectrode arrays electrochemically deposited with a poly(3,4-ethylenedioxythiophene) (PEDOT) film," *J. Neural Eng.*, vol. 3, no. 1, pp. 59-70, 2006.
- [83] D. Brüggemann, B. Wolfrum, V. Maybeck, Y. Mourzina, M. Jansen, and A. Offenhäusser, "Nanostructured gold microelectrodes for extracellular recording from electrogenic cells," *Nanotechnology*, vol. 22, no. 26, pp. 1-7, 2011.
- [84] E. W. Keefer, B. R. Botterman, M. I. Romero, A. F. Rossi, and G. W. Gross, "Carbon nanotube coating improves neuronal recordings," *Nat. Nanotechnol.*, vol. 3, no. 7, pp. 434-439, 2008.
- [85] A. Hai and M. E. Spira, "On-chip electroporation, membrane repair dynamics and transient in-cell recordings by arrays of gold mushroom-shaped microelectrodes," *Lab Chip*, vol. 12, no. 16, pp. 2865-2873, 2012.
- [86] X. Duan and C. M. Lieber, "Nanoelectronics meets biology: From new nanoscale devices for live-cell recording to 3D innervated tissues," *Chem. - An Asian J.*, vol. 8, no. 10, pp. 2304-2314, 2013.
- [87] J. T. Robinson, M. Jorgolli, A. K. Shalek, M.-H. Yoon, R. S. Gertner, and H. Park, "Vertical nanowire electrode arrays as a scalable platform for intracellular interfacing to neuronal circuits," *Nat. Nanotechnol.*, vol. 7, no. 3, pp. 1-16, 2012.
- [88] M. R. Angle and A. T. Schaefer, "Neuronal recordings with solid-conductor intracellular nanoelectrodes (SCINs)," *PLoS One*, vol. 7, no. 8, pp. 1-8, 2012.
- [89] C. Xie, Z. Lin, L. Hanson, Y. Cui, and B. Cui, "Intracellular recording of action potentials by nanopillar electroporation," *Nat. Nanotechnol.*, vol. 7, no. 3, pp. 185-190, 2012.
- [90] A. Hai *et al.*, "Changing gears from chemical adhesion of cells to flat substrata toward engulfment of micro-protrusions by active mechanisms.," *J. Neural Eng.*, vol. 6, no. 6, pp. 1-12, 2009.
- [91] M. E. Spira *et al.*, "Improved neuronal adhesion to the surface of electronic device by engulfment of protruding micro-nails fabricated on the chip surface," in *TRANSDUCERS and EUROSENSORS '07 - 14th International Conference on Solid-State Sensors, Actuators and Microsystems*, 2007, pp. 1247-1250.
- [92] G. Panaitov, S. Thiery, B. Hofmann, and A. Offenhäusser, "Fabrication of gold micro-spine structures for improvement of cell/device adhesion," *Microelectron. Eng.*, vol. 88, no. 8, pp. 1840-1844, 2011.

- [93] F. Santoro, J. Schnitker, G. Panaitov, and A. Offenhausser, "On chip guidance and recording of cardiomyocytes with 3D mushroom-shaped electrodes," *Nano Lett.*, vol. 13, no. 11, pp. 5379-5384, 2013.
- [94] A. Matus, "Growth of dendritic spines: A continuing story," *Curr. Opin. Neurobiol.*, vol. 15, no. 1, pp. 67-72, 2005.
- [95] Y. Hayashi and A. K. Majewska, "Dendritic spine geometry: Functional implication and regulation," *Neuron*, vol. 46, no. 4, pp. 529-532, 2005.
- [96] J. P. Spatz and B. Geiger, "Molecular Engineering of Cellular Environments: Cell Adhesion to Nano-Digital Surfaces," *Methods Cell Biol.*, vol. 83, no. 07, pp. 89-111, 2007.
- [97] R. C. May and L. M. Machesky, "Phagocytosis and the actin cytoskeleton," *J. Cell Sci.*, vol. 114, no. 6, pp. 1061-1077, 2001.
- [98] L. M. Stuart and R. A. B. Ezekowitz, "Phagocytosis: Elegant complexity," *Immunity*, vol. 22, no. 5, pp. 539-550, 2005.
- [99] S. Aimon, A. Callan-Jones, A. Berthaud, M. Pinot, G. E. S. Toombes, and P. Bassereau, "Membrane shape modulates transmembrane protein distribution," *Dev. Cell*, vol. 28, no. 2, pp. 212-218, 2014.
- [100] V. Vogel and M. Sheetz, "Local force and geometry sensing regulate cell functions," *Nat. Rev. Mol. Cell Biol.*, vol. 7, no. 4, pp. 265-275, 2006.
- [101] J. Müller, D. J. Bakkum, and A. Hierlemann, "Sub-millisecond closed-loop feedback stimulation between arbitrary sets of individual neurons," *Front. Neural Circuits*, vol. 6, pp. 1-11, 2013.
- [102] S. Hafizovic *et al.*, "A CMOS-based microelectrode array for interaction with neuronal cultures," *J. Neurosci. Methods*, vol. 164, no. 1, pp. 93-106, 2007.
- [103] D. A. Wagenaar, R. Madhavan, J. Pine, and S. M. Potter, "Controlling Bursting in Cortical Cultures with Closed-Loop Multi-Electrode Stimulation," *J. Neurosci.*, vol. 25, no. 3, pp. 680-688, 2005.
- [104] R. Q. Quiroga, "Spike sorting," *Scholarpedia*, vol. 2, no. 12, p. 3583, 2007.
- [105] R. Q. Quiroga, Z. Nadasdy, and Y. Ben-Shaul, "Unsupervised Spike Detection and Sorting with Wavelets and Superparamagnetic Clustering," *Neural Comput.*, vol. 16, no. 8, pp. 1661-1687, 2004.
- [106] S. G. Mallat, "A theory for multiresolution signal decomposition: the wavelet representation," *IEEE Trans. Pattern Anal. Mach. Intell.*, vol. 11, no. 7, pp. 674-693, 1989.
- [107] O. Miranda-Domínguez, J. Gonia, and T. I. Netoff, "Firing rate control of a neuron using a linear proportional-integral controller," *J. Neural Eng.*, vol. 7, no. 6, pp. 1-10, 2010.
- [108] P. Gorzelic, S. J. Schiff, and A. Sinha, "Model-based rational feedback controller design for closed-loop deep brain stimulation of Parkinson ' s disease," *J. Neural Eng.*, vol. 10, no. 2, pp. 1-16, 2013.
- [109] K. J. Astrom and T. Hagglund, *PID controllers: theory, design and tuning*, 2nd ed. 1995.
- [110] "National Instruments," *Explicando a Teoria PID*, 2011. [Online]. Available: <http://www.ni.com/white-paper/3782/pt/>. [Accessed: 24-Aug-2018].
- [111] K. J. Astrom and R. M. Murray, *Feedback Systems: an Introduction for Scientists and Engineers*. Princeton University Press, 2008.
- [112] K. H. Ang, G. Chong, and Y. Li, "PID control system analysis, design, and technology," *IEEE Trans. Control Syst. Technol.*, vol. 13, no. 4, pp. 559-576, 2005.
- [113] "Wikipedia," *PID controller*. [Online]. Available: https://en.wikipedia.org/wiki/PID_controller. [Accessed: 25-Aug-2018].
- [114] R. C. Panda, C. Yu, and H. Huang, "PID tuning rules for SOPDT systems: review and some new results," *ISA Trans.*, vol. 43, no. 2, pp. 283-295, 2004.
- [115] M. Shahrokhi and A. Zomorodi, "Comparison of PID Controller Tuning Methods," 2012.
- [116] K. J. Åström and T. Hägglund, "The future of PID control," *Control Eng. Pract.*, vol. 9, no.

- 11, pp. 1163-1175, 2001.
- [117] "Control Soft." [Online]. Available: <https://www.controlsoftinc.com/intune/intunetuningtools.shtml>. [Accessed: 13-Aug-2018].
 - [118] N. Brunel, F. S. Chance, N. Fourcaud, and L. F. Abbott, "Effects of Synaptic Noise and Filtering on the Frequency Response of Spiking Neurons," *Phys. Rev. Lett.*, vol. 86, no. 10, pp. 2186-2189, 2001.
 - [119] MultiChannel Systems, "MEA2100-System: User manual," 2017.
 - [120] M. Systems, "MEA2100-System: Technical Specifications," 2018.
 - [121] MultiChannel Systems, "120-MEA Layout," 2016.
 - [122] MultiChannel Systems, "Microelectrode array (MEA): User manual," 2017.
 - [123] M. Systems, "Multi Channel Experimenter Manual," 2017.
 - [124] "Multichannel Systems," *MEA2100-Systems*. [Online]. Available: <https://www.multichannelsystems.com/products/mea2100-systems#description>. [Accessed: 01-Sep-2018].
 - [125] M. L. Gertz, Z. Baker, S. Jose, and N. Peixoto, "Time-dependent Increase in the Network Response to the Stimulation of Neuronal Cell Cultures on Micro-electrode Arrays," *J. Vis. Exp.*, vol. 123, pp. 1-16, 2017.
 - [126] D. A. Wagenaar, J. Pine, and S. M. Potter, "Effective parameters for stimulation of dissociated cultures using multi-electrode arrays," *J. Neurosci. Methods*, vol. 138, pp. 27-37, 2004.
 - [127] R. Vardi *et al.*, "Neuronal response impedance mechanism implementing cooperative networks with low firing rates and us precision," *Front. Neural Circuits*, vol. 9, pp. 1-16, 2015.
 - [128] J. Wang, M. Trumpis, M. Insanally, R. Froemke, and J. Viventi, "A low-cost, multiplexed electrophysiology system for chronic uECoG recordings in rodents," in *36th Annual International Conference of the IEEE Engineering in Medicine and Biology Society*, 2014, pp. 5256-5259.

Appendix A

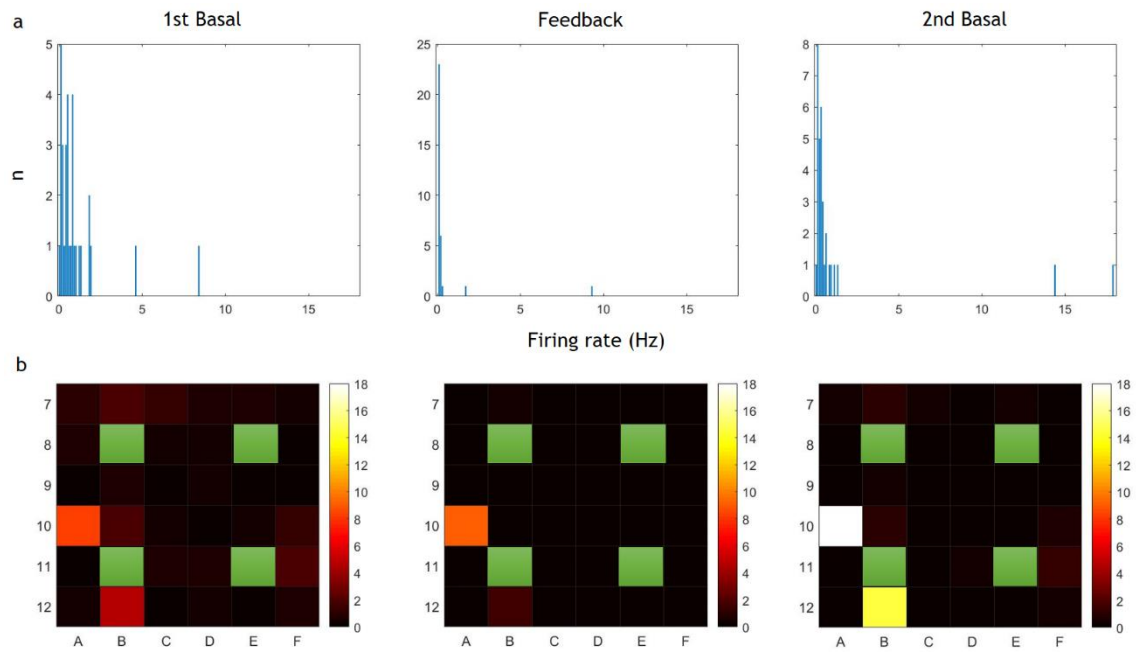


Figure 1 - Complementary results of the experiment 18 (at 19DIV). (a) Histograms (in the form of bar plots) showing the variation in the firing rates of all recording electrodes during the experiment. (b) Color maps showing the spatial distribution of the activity in the recording electrodes over the experiment. The green squares correspond to the stimulation electrodes.

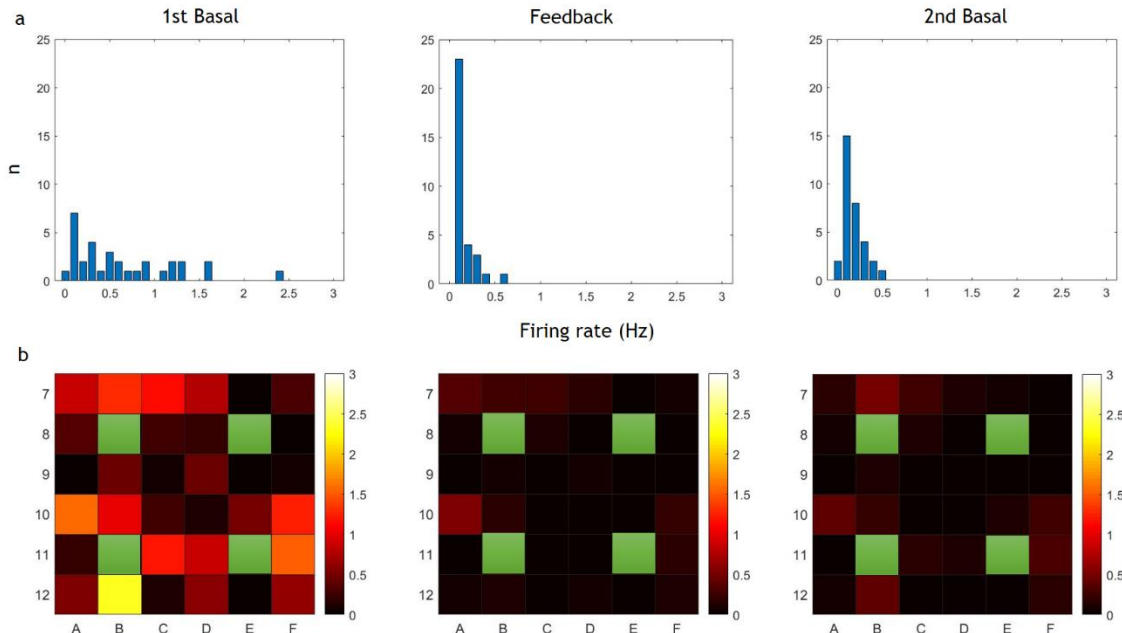


Figure 2 - Complementary results of the experiment 22 (at 22DIV). (a) Histograms (in the form of bar plots) showing the variation in the firing rates of all recording electrodes during the experiment. (b) Color maps showing the spatial distribution of the activity in the recording electrodes over the experiment. The green squares correspond to the stimulation electrodes.

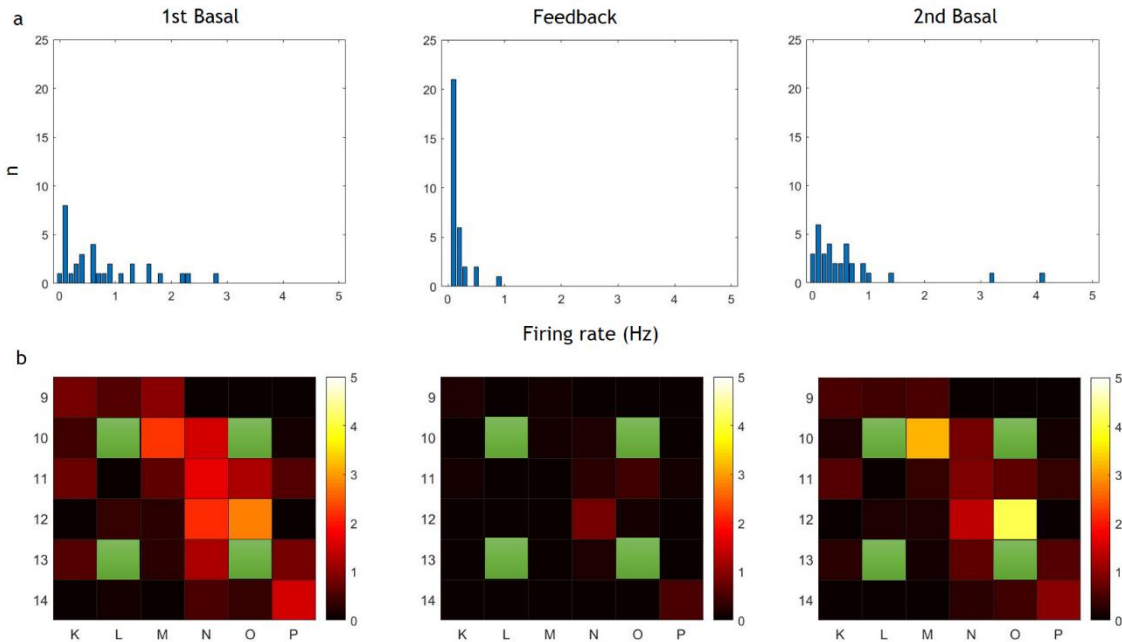


Figure 3 - Complementary results of the experiment 21 (at 21DIV). (a) Histograms (in the form of bar plots) showing the variation in the firing rates of all recording electrodes during the experiment. (b) Color maps showing the spatial distribution of the activity in the recording electrodes over the experiment. The green squares correspond to the stimulation electrodes.

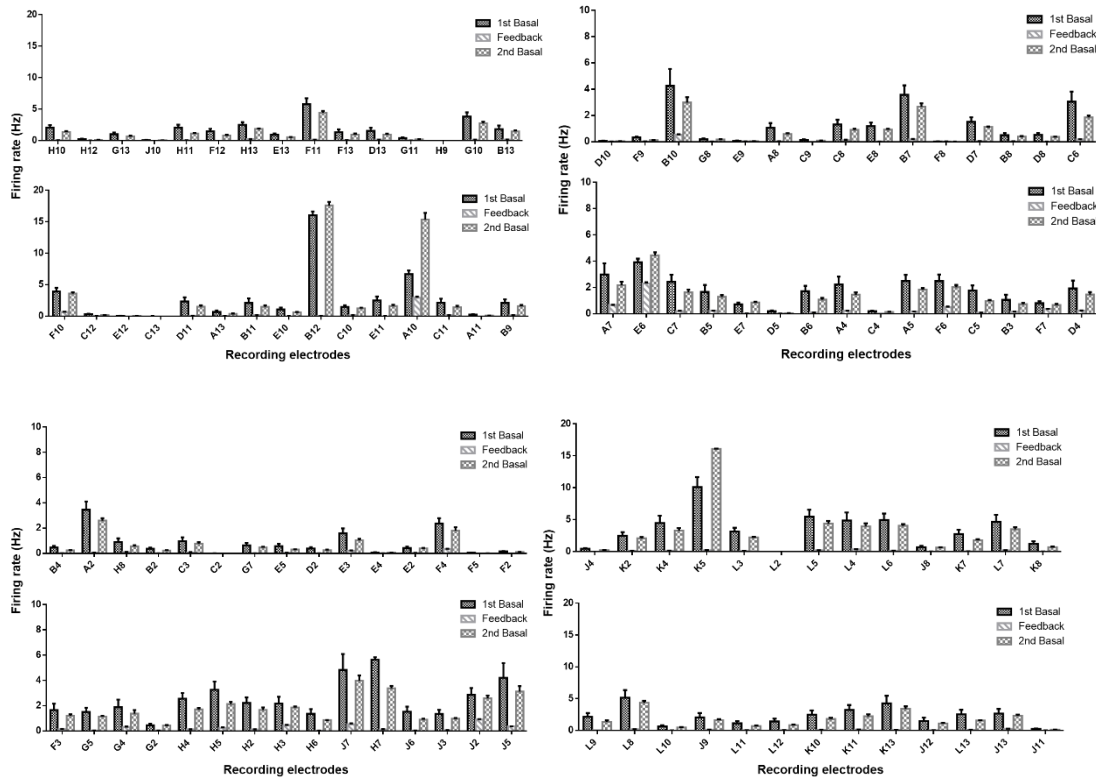


Figure 4 - Bar plot graphs showing the activity mean levels and respective standard deviations of the neuronal network experiment (17). Cell's at 17DIV.

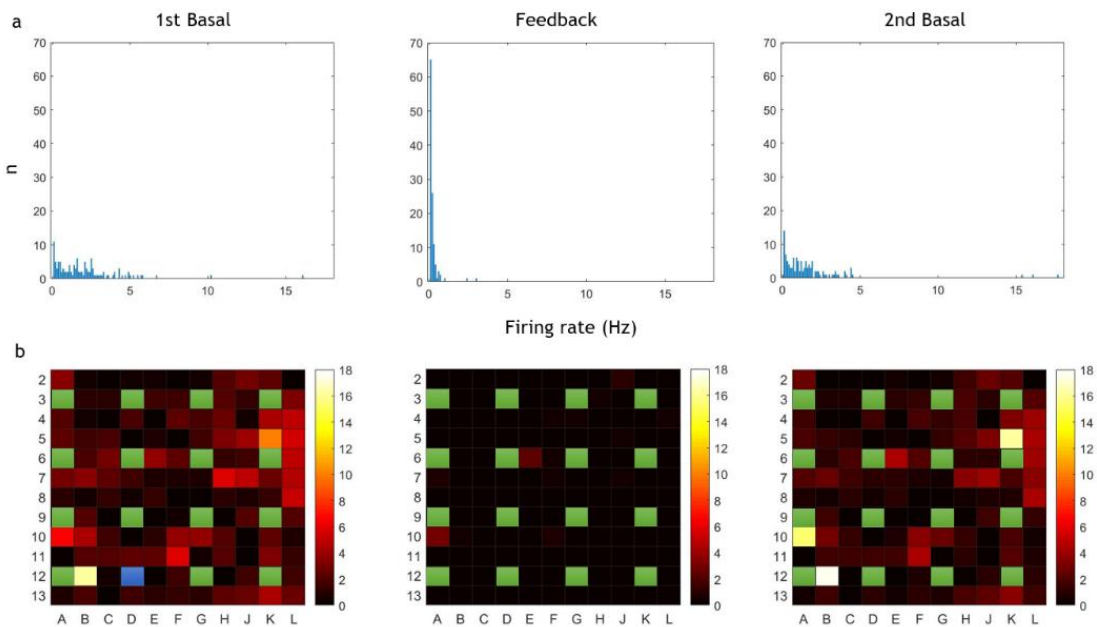


Figure 5 - Complementary results of the experiment 17 (at 17DIV). (a) Histograms (in the form of bar plots) showing the variation in the firing rates of all recording electrodes during the experiment. (b) Color maps showing the spatial distribution of the activity in the recording electrodes over the experiment. The green squares correspond to the stimulation electrodes.

Appendix B

As previously mentioned in the objectives section, a supplementary goal of this dissertation was the design and construction of a low cost and easy-to-build DIY (“Do-It-Yourself”) electrophysiology system. This was motivated by the fact that equipment for electrophysiology with microelectrode arrays is quite expensive, and out of reach for many neuroscience/neuroengineering research labs. The DIY system was composed by two components: a low-cost amplifier and an electronic interface-headstage capable of reading and transmitting electrophysiological signals from a multielectrode array with 60 electrodes (60MEA chip) to a data acquisition system.

The first component is a high-precision amplifier circuit to amplify, filter and detect electrophysiological signals. This circuit was built within the scope of a course of the first year of the Biomedical Engineering masters, which aimed to develop a project related to the dissertation’s area. The circuit used to build the amplifier is in the figure 6. Its schematic was designed using the freely available EAGLE 8.2.0. software, as well as the design of the PCB (*Printed Circuit Board*). The mounted circuit and the PCB are in the figure 7. This circuit can be divided into two stages as shown in the figure below. In respect to the components, since this is a circuit of high precision to measure signals with amplitudes with a very low order of magnitude, were used low-noise components. Taking this into account, were used resistors with tolerances of 1 % to ensure that the values of the resistances vary the minimum as possible. The amplifiers should also have low noise features.

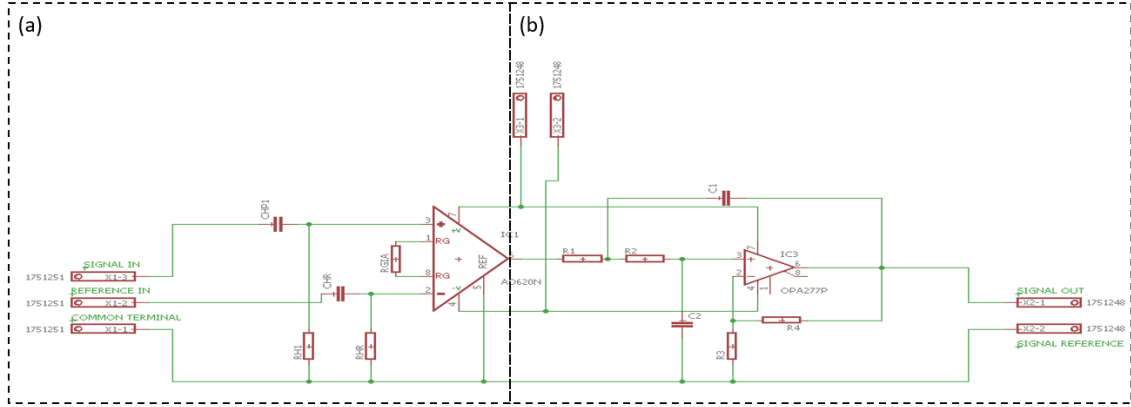


Figure 6 - Circuit diagram of the amplifier designed in the Eagle 8.2.0 software. (a) Pre-amplifier circuit with a passive high-pass filter. (b) Amplifier with second-order active low-pass filter.

The first stage (a) aims to amplify the signal and remove the DC component of the input signals through the application of a high-pass filter in each input. For the amplification of the signal was used an instrumentation amplifier, the AD620. This is a low noise amplifier with a high performance, which common applications are medical instrumentation and data acquisition systems. The amplification gain is defined by an external resistor connected to the terminals 1 and 8 of the amplifier, in this case, is represented in the figure by the resistor RGIA. The value of the gain was set to 500. To obtain this gain, the value of the resistor RGIA was calculated through the next equation, according to the instructions available in the amplifier's datasheet. The calculated value was $99.0\ \Omega$, however, due to unavailability of that value of resistance, it was used a resistor of $100.0\ \Omega \pm 1\%$, which gives a theoretical gain of 495 V/V. This high-pass filter has a cutoff frequency of 0.34 Hz.

$$G_{1st\ stage} = 1 + \frac{49.4K\Omega}{RGIA}$$

The second stage aims to amplify and filter the signal. Here, was used an operational amplifier of high precision, the OPA277, which also has an ultralow offset voltage. This stage contains a second order low-pass filter in a well-known configuration, is a Sallen-Key filter, with a cutoff frequency of 4109 Hz. The amplification gain is defined by the resistors R_3 and R_4 as shown in the following equation and, was defined a theoretical gain of 11 V/V. Thus, the gain of the entire circuit is given by multiplying the individual gains of each stage, which results in a theoretical gain of 5445 V/V.

$$G_{2nd\ stage} = 1 + \frac{R_4}{R_3}$$

The experimental results showed a total experimental gain of approximately 5260 V/V. In addition, the frequency response results confirmed that the cutoff frequency of the low-pass filter was well established.

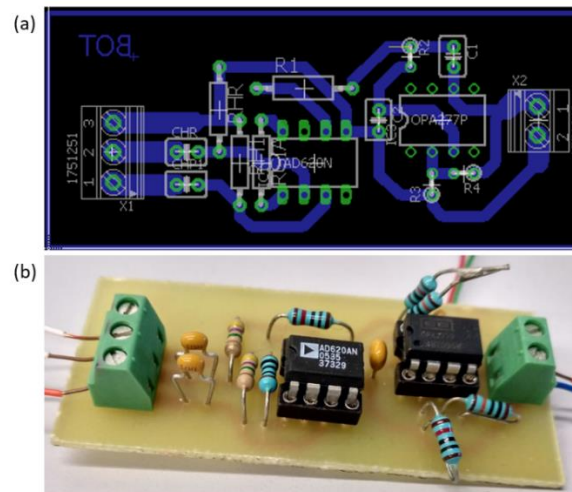


Figure 7 - Electrophysiology amplifier. (a) Design of the PCB (Printed Circuit Board). (b) Assembly of components on the PCB.

This was only a prototype and, the integration of SMD (surface mount devices) components could considerably improve the performance of the amplifier circuit.

The second component of the low cost and easy-to-build DIY electrophysiology system is an electronic interface-headstage for a 60MEA chip. The aim of this interface was to do the “bridge” between the MEA chip with 60 microelectrodes (where the cells are cultured) and the amplifier. Despite the time did not allow the conclusion of this project, a first prototype was built. The headstage has multiplexing capabilities. In the circuit were used two ADG726 (Analog Devices, Inc) multiplexers which are used in applications like medical instrumentation and data acquisition systems. According to Wang et al. in [128], these multiplexers have a noise of only $1.6 \mu V$ RMS. In addition, they are dual 16:1 multiplexers, i.e., each multiplexer has two independent circuits that have 16 inputs and 1 output. Thus, from the 60 microelectrodes of the MEA chip, the multiplexer will be capable to transmit signals from 4 electrodes through four independent output channels. The headstage printed circuit board (PCB) was designed in the open-source software Eagle 8.3.2. However, the free open-source version has space constrains which increased the difficulty of the PCB’s design. The PCB design is in the figure 8. The center square (green) corresponds to the places where the gold pins will be inserted to contact with the sensing pads of the MEA chips. This square was designed by hand according to the dimension specifications of a commercial 60MEA chip.

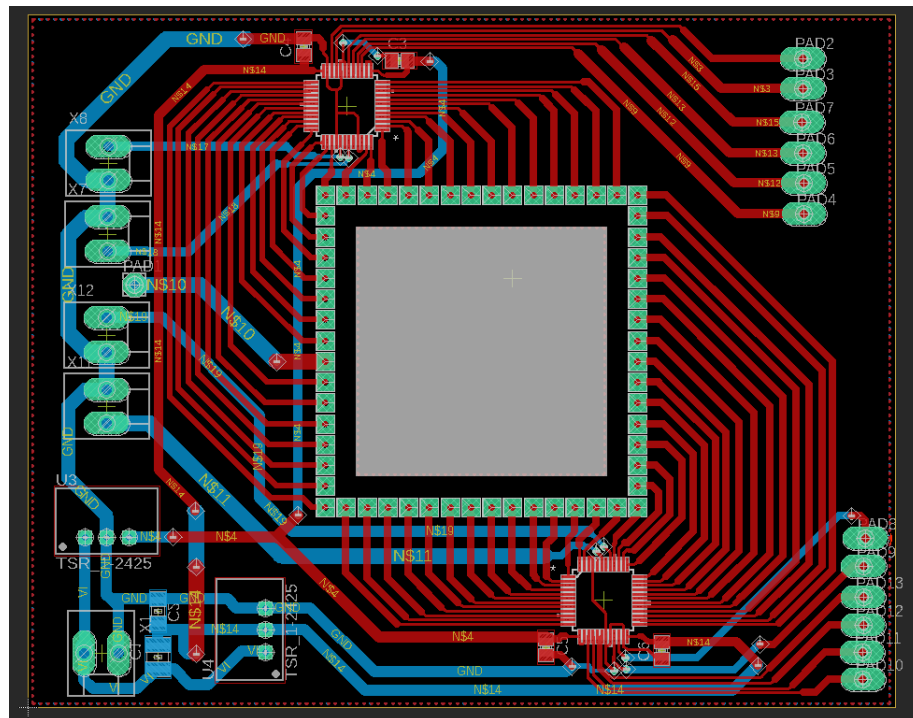


Figure 8 - Headstage's Printed Circuit Board (PCB). The red lines correspond to the vias on the top of the PCB and the blue lines to the vias on the bottom.

One of the steps of this work consisted in learning how to control National Instruments data acquisition boards (NI-DAQs) using MATLAB. The focus was to create a toolbox with specific commands to acquire electrophysiological signals through NI-DAQ devices. Despite its use to acquire data, this board will also be used to control the DIY headstage. The switching control of the multiplexers' channels is done through the digital outputs of the DAQ. To do the switching of 16 channels, each multiplexer uses 4 bits. The only problem of this type of multiplexers is that we cannot control the dual multiplexers integrated in each multiplexer separately. I.e., within each multiplexer exists the circuit A and B (output A and B) that transmit in parallel their correspondent channel according to the sequence of bits introduced in the multiplexer. A friendly graphical user interface (GUI) was developed in MATLAB to give instructions to the headstage through the NI-DAQ device. It enables the selection of the readout channels, record and plot the signal according to a specific acquisition rate and duration settled by the user. The user also has the option to save the data of each independent readout channel or all at once, in a user-chosen directory.

The figure 9 shows the final result of the circuit construction. A case to support the headstage was built using a 3D-printer.

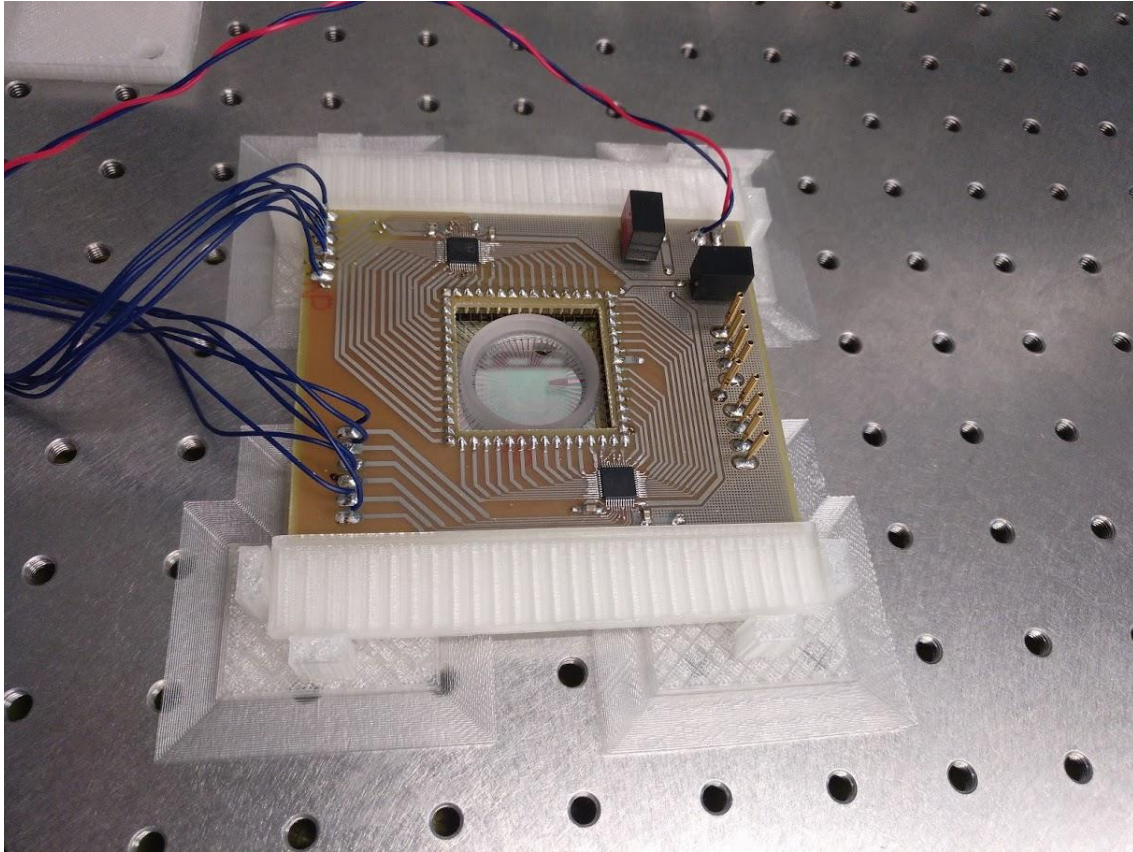


Figure 9- Headstage circuit in a case (white) 3D-printer.

Until now, it is possible to select the desired channels of the multiplexer using the developed GUI. The tests demonstrated that the switching is working exactly as it should. However, the DC/DC converters (TSRN -1 - Traco Power) used to regulate the voltages to supply the multiplexers ($\pm 2.5\text{ V}$) are the main responsible for the noise introduced into the system which did not allow us to see the neuronal activity because, this headstage does not have any type of pre-amplification of the signals until the signal enters in the multiplexers. However, despite design problems, a lot of skills in different areas were improved.